

Disorder-induced quantum phenomena  
in inhomogeneous optical lattices

Masaru Sakaida



# Abstract

Thanks to marked developments of laser techniques and atom cooling techniques, a new research field called cold atomic systems was pioneered in the early 1990s. The cold atomic systems are a new platform to investigate novel quantum phenomena and significant devices, such as Bose-Einstein condensation, an optical clock, a quantum bit, and so on. Moreover, these systems are expected to play a role as a quantum simulator of several model Hamiltonians which have been analyzed in solid state physics.

Especially among cold atomic fields, spatially-disordered optical lattices recently attract our interest. The correlated lattice systems with spatial nonuniformity have been investigated since 1960s in solid state physics, but complete understandings of such systems are not obtained. This is because it is rather difficult to tune the strength of spatial inhomogeneity and interaction between particles in ordinary materials. On the other hand, high controllability, which is a feature of cold atomic systems, enables us to systematically tune the above two effects in spatially-disordered optical lattices. Therefore, we can investigate the effects of disorder and interaction in an extremely wide region which is difficult to experimentally access in solids.

Motivated by these backgrounds, we investigate the correlated systems with spatial inhomogeneity described by an  $N$ -component Anderson-Hubbard model where  $N$  denotes the number of components, and report the obtained results in this thesis. To analyze the two-component systems, we employ the statistical dynamical mean-field theory, which is an extension of a usual dynamical mean-field theory and enables us to successfully treat both effects of spatial nonuniformity and interaction, and Bogoliubov-de Gennes equations are used to address the  $N=3$  and 4 cases.

In the analysis of two-component attractively interacting Fermi systems with diagonal disorder which is described by a uniform distribution function, we confirm that spatial nonuniformity triggers the transition between a superfluid state and a Cooper-pair insulating state, and find that the Cooper-pair insulating state gradually crossovers to an ordinary Anderson localized state. We also address the systems with spatial disorder characterized by a bimodal distribution function, and thus clarify that not band-splitting effects but spatial inhomogeneity due to binary disorder plays a main role in dictating the properties of whole systems in a certain condition.

Furthermore, it is found that the superfluid state-band insulator transition, which is characteristic of the systems with binary disorder, occurs in a different condition. Through these studies, we elucidate that attractive interaction enhances the effects of spatial disorder.

In the study of multicomponent attractively interacting Fermi systems with on-site disorder, we find that in the  $N=3$  case spatial disorder induces the transition between a density-wave state and an  $s$ -wave superfluid state and stabilizes the  $s$ -wave superfluid state as the ground state. The feature of this transition is clarified from the results of the spectral gap at the Fermi level and the histogram of the local particle density. It is also found that the superfluid state-Anderson localized state transition occurs as the strength of spatial disorder further increases. We find that these two transitions are of first-order. We also address the four-component attractive Anderson-Hubbard model with spatial nonuniformity. It is found that the density-wave state directly undergoes a transition to the Anderson localized state, and the transition between the density-wave state and the Anderson localized state is of second-order. It is expected from this result that the density-wave state-Anderson localized state transition directly occurs in the  $N>3$  case.

This thesis is organized as follows. Chap. 1 gives an overview of cold atomic systems, and the aim of this study is clarified in this chapter. We introduce the statistical dynamical mean-field theory and the Bogoliubov-de Gennes method in Chap. 2. The numerical results of  $N$ -component attractively interacting Fermi systems with diagonal disorder are given in Chaps. 3 and 4. Our results are summarized in Chap. 5.

# List of publications

1. Masaru Sakaida, Kazuto Noda, and Norio Kawakami  
*Effects of Disorder on Superfluidity in the Attractive Hubbard Model*  
Journal of the Physical Society of Japan **82**, 074715 (2013).
2. Masaru Sakaida, Kazuto Noda, and Norio Kawakami  
*Superfluid-Insulator Transition Caused by Binary Disorder*  
Japan Physics Society Conference Proceedings **3**, 016002 (2014).
3. Masaru Sakaida and Norio Kawakami  
*Disorder-induced charge-density-wave-superfluid transition in  $SU(N)$  Fermi systems*  
Physical Review A **90**, 013632 (2014).
4. Masaru Sakaida and Norio Kawakami  
*Competition between superfluid order and charge-density-wave order in  $SU(N)$  disordered attractive Fermi systems*  
Journal of Physics: Conference Series **592**, 125405 (2015).

# Contents

<b>1</b>	<b>Introduction</b>	<b>8</b>
1.1	Cold atoms in optical lattice . . . . .	8
1.1.1	Advantage of cold atoms in optical lattice . . . . .	9
1.2	Fermi systems with spatial inhomogeneity . . . . .	12
1.2.1	Effects of spatial disorder . . . . .	12
1.2.2	How do interaction and spatial disorder compete/collaborate with each other? . . . . .	16
1.2.3	Superfluidity in spatially disordered systems . . . . .	19
1.3	Open questions of spatially disordered systems . . . . .	19
<b>2</b>	<b>Numerical calculation method</b>	<b>22</b>
2.1	Statistical dynamical mean-field theory . . . . .	22
2.1.1	Dynamical mean-field theory . . . . .	22
2.1.2	Coherent potential approximation . . . . .	29
2.1.3	How to treat backscattering effects within a DMFT . . . . .	32
2.1.4	Extension of statistical DMFT . . . . .	36
2.1.5	Impurity solver : modified iterative perturbation theory . . . . .	38
2.2	Bogoliubov-de Gennes method . . . . .	40
2.2.1	Two-component Fermi systems with disorder . . . . .	41
2.2.2	Multicomponent Fermi systems with disorder . . . . .	42
<b>3</b>	<b>Two-component systems with spatial nonuniformity</b>	<b>46</b>
3.1	Numerical setup . . . . .	46
3.2	Uniformly disordered systems . . . . .	47
3.2.1	Superfluid-insulator transition . . . . .	51
3.2.2	Phase diagram of uniformly-disordered systems . . . . .	55
3.3	Binary-disordered systems . . . . .	57
3.3.1	$n \neq 2\gamma$ . . . . .	58
3.3.2	$n = 2\gamma$ . . . . .	60
3.4	Summary . . . . .	62

---

<b>4</b>	<b>Multicomponent systems with spatial nonuniformity</b>	<b>63</b>
4.1	Ground state of multicomponent systems with disorder . . . . .	63
4.2	SU(3) Fermi systems with spatial nonuniformity . . . . .	65
4.2.1	Density-density correlation . . . . .	65
4.2.2	Superfluid state in SU(3) systems . . . . .	67
4.2.3	Disorder-induced DW-SF transition . . . . .	69
4.2.4	Effective disorder . . . . .	71
4.2.5	SF-AL transition in SU(3) systems . . . . .	72
4.2.6	Ground state phase diagram of SU(3) Fermi systems . . . . .	74
4.3	SU(4) Fermi systems with spatial disorder . . . . .	75
4.4	Summary . . . . .	78
<b>5</b>	<b>Conclusion</b>	<b>80</b>
	Bibliography	82
	Acknowledgment	88

# Chapter 1

## Introduction

In Chapter 1, we describe in detail the cold atomic systems which are our main subject. In particular, we explain the spatially disordered optical lattices which recently attract our interest, and multicomponent Fermi systems which are successfully realized in cold atoms. Also, important theoretical studies of disordered systems are introduced. At the end of this chapter, we clarify the aim of our study.

### 1.1 Cold atoms in optical lattice

In the latter half of 1980s, remarkable experimental techniques, such as a trapping technique[1, 2, 3] and a cooling technique[4], were established. Optical trapping of dielectric particles and neutral particles by the single beam was demonstrated in 1970[1] and 1986[3], and the observation of the electromagnetically trapped neutral particles was reported in 1985[5]. In addition to the development of the trapping techniques, a laser cooling (Doppler cooling) technique was established around the same time[4]. One can cool atoms down to temperature of the order of microkelvin by the laser cooling technique. Moreover, by using other techniques, such as an evaporative cooling technique[6, 7], after the Doppler cooling method, atoms can be cooled down to further low temperature of the order of nanokelvin. At the temperature of the order of nanokelvin, thermal fluctuation is sufficiently suppressed and quantum effects dominantly characterize the properties of systems. Therefore, the cold atomic systems produced by the optical trapping and cooling techniques are expected as a new ground where one can investigate quantum phenomena, for examples, Bose-Einstein condensation (BEC)[8, 9]. Moreover, the optical lattice[10] constructed from a standing wave is realized by applying the optical trapping. Optical lattice systems provide a platform for investigating the phenomena which are observed in solids, such as Anderson localization[11, 12], a Mott insulator[13], and so on.

## 1.1.1 Advantage of cold atoms in optical lattice

The high controllability is the biggest advantage which cold atomic systems have. Successfully controlling and arranging laser systems, one can tune the dimension and the geometry of optical lattices and thus experimentally realize various lattices; a one-dimensional chain, a square lattice, a cubic lattice[10], a triangular lattice[14, 15], a bipartite lattice[16, 17], a honeycomb lattice[18, 19], a Kagome lattice[20], a Lieb lattice[39], and so on. We show some of them in Fig. 1.1. Among these lattices,

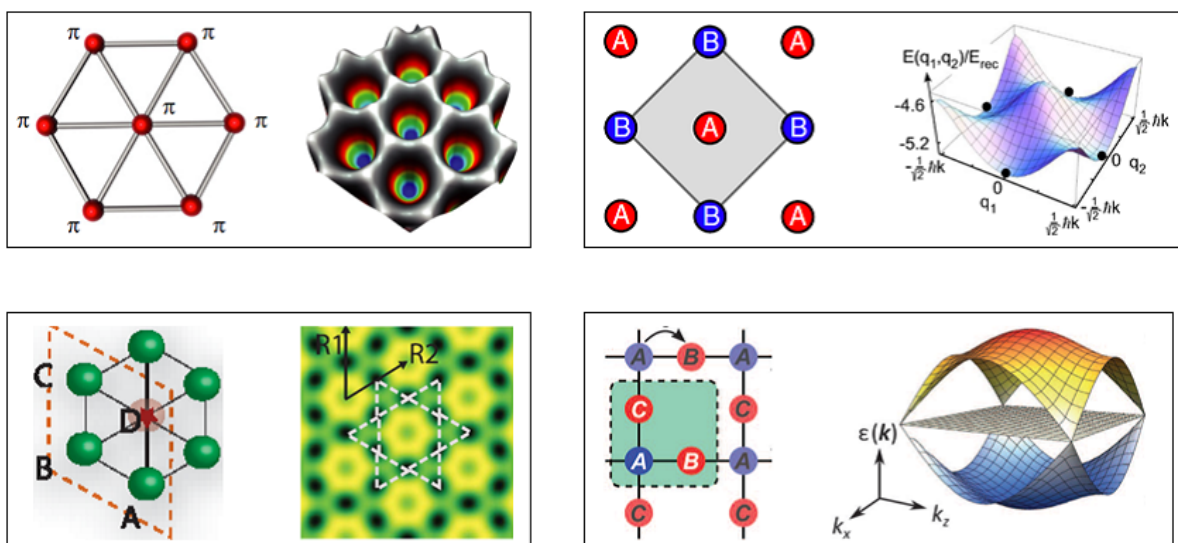


Fig. 1.1 Optical lattices; a triangle lattice (upper left), bipartite lattice (upper right), Kagome lattice (lower left), and Lieb lattice (lower right). These figures are reprinted from Refs. [14, 16, 20, 39].

optical lattices with spatial nonuniformity[11, 12, 22, 23, 24, 25] especially attract our interest. Such lattices are constructed by managing the several lasers with different phases or the laser beam diffracted through a ground-glass plate. Schematic views of the spatially disordered optical lattices are shown in Fig. 1.2. In the disordered optical lattices, one can systematically tune disorder strength by changing the intensity of lasers. In addition to the structure of optical lattices, the strength of the interaction between atoms is also tunable by controlling optical lattice depth or a magnetic field. The tuning technique by a magnetic field applies a Feshbach resonance[26] and enables us to systematically tune the interaction between atoms even from repulsion to attraction. This high controllability allows to investigate the effects of disorder and interaction in an extremely wide region which is rather difficult to experimentally access in solid-state materials.

It is another advantage of cold atoms that we can realize novel systems, such as

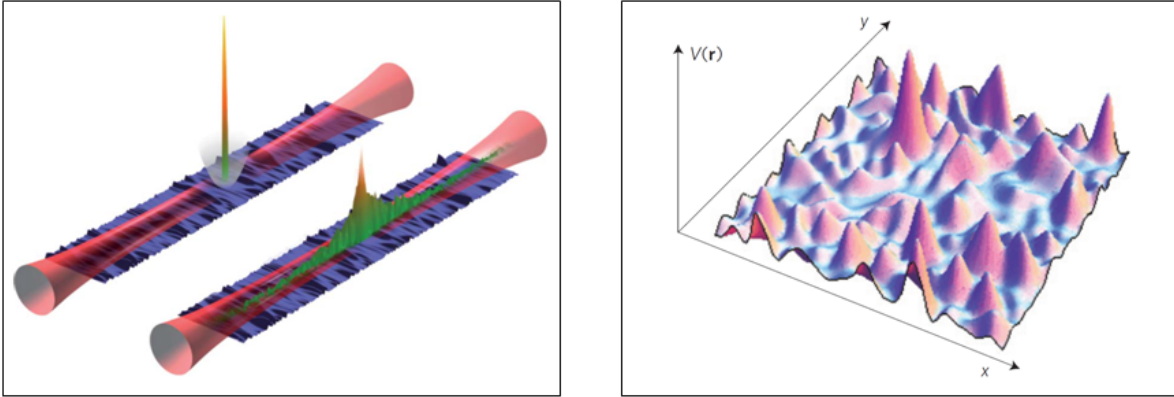


Fig. 1.2 (From [11, 24]) One (left figure) and two (right figure) dimensional optical lattices with spatial disorder.

Bose-Fermi mixed systems[27, 28, 29, 30, 31, 32], multicomponent systems[33], and so on. In such systems, one might observe the nontrivial quantum phenomena which are unlikely to occur in ordinary materials. For examples, a filling induced Mott transition was observed in  $^{173}\text{Yb}$ - $^{174}\text{Yb}$  mixtures[31] (Fig. 1.3) and the coherent energy transfer due to the interaction between bosons and fermions was demonstrated in a mixture of bosonic and fermionic superfluids[32] (Fig. 1.4). Also,  $^{174}\text{Yb}$ - $^6\text{Li}$

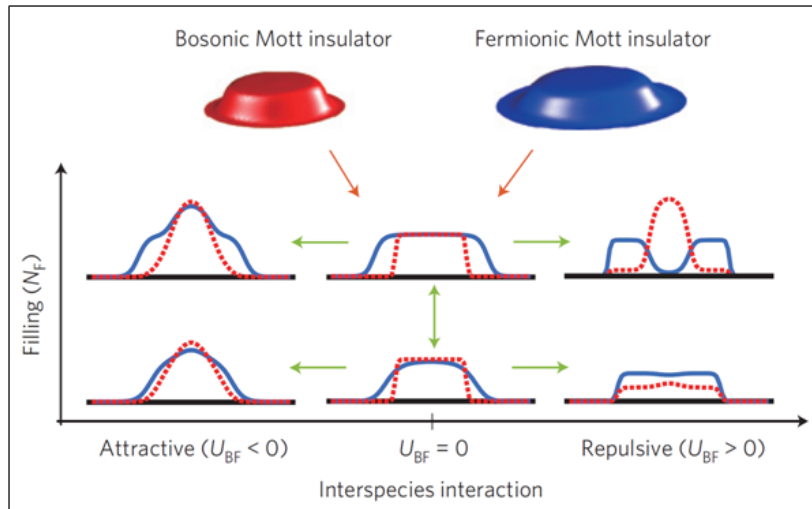


Fig. 1.3 (From [31]) Schematic pictures of the quantum phases in  $^{173}\text{Yb}$ - $^{174}\text{Yb}$  mixtures.

mixtures in cold atoms are expected as a quantum simulator of the binary-disordered systems corresponding to binary-alloys and doped materials[30]. Due to the large mass imbalance of  $^{174}\text{Yb}$  and  $^6\text{Li}$ , a  $^{174}\text{Yb}$  atom plays a role of the impurities and a  $^6\text{Li}$  atom the electrons in such mixtures.

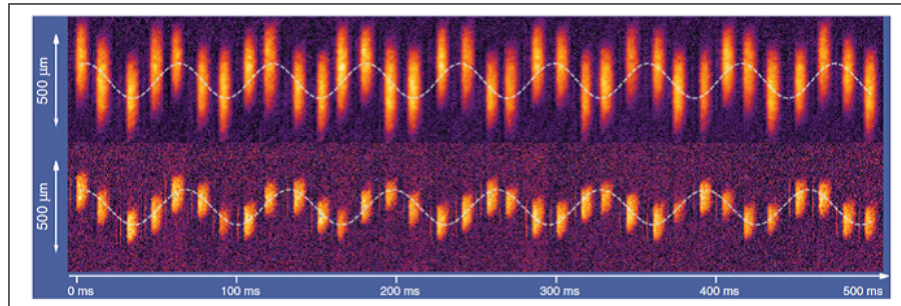


Fig. 1.4 (From [32]) Coherent oscillation of the superfluid mixture.

We would like to introduce the multicomponent Fermi systems in some detail here. After the realization of the quantum degenerate Fermi gases of  $^{40}\text{K}$ [34], quantum degenerate states of many species of atoms ( $^6\text{Li}$ [35],  $^{173}\text{Yb}$ [36],  $^{87}\text{Sr}$ [37], and so on.) have been also observed. The atoms mentioned above have a large nuclear spin  $I$  besides the electron spin  $1/2$ . This large nuclear spin allows these atoms to have  $(2I+1)$ -degenerate low-lying hyperfine states (degeneracy is multiplied by two if the spin degrees of freedom of electrons are relevant). One can appropriately choose some species from these hyperfine states. By loading the chosen species into optical lattices, the multicomponent Fermi systems should be realized in cold atoms (see Fig. 1.5). It is expected that one can observe rich phases and nontrivial properties due

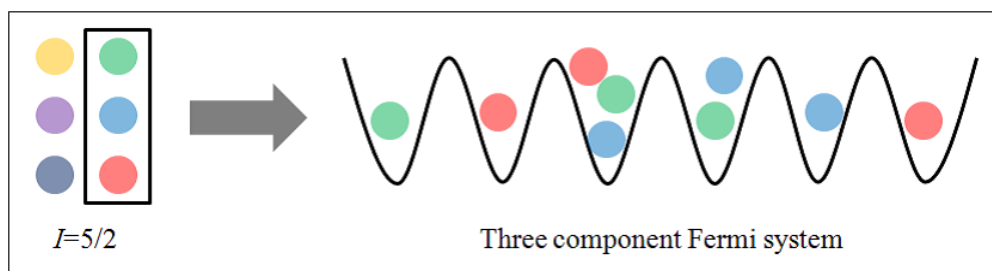


Fig. 1.5 Schematic picture to prepare the multicomponent Fermi systems. This picture shows how to prepare the three-component Fermi systems (right figure) by using six-component atoms of  $^{173}\text{Yb}$  with  $I=5/2$  (left figure).

to many degrees of freedom in the multicomponent Fermi systems, and thereby the multicomponent Fermi systems attract our attention.

The multicomponent Fermi systems in cold atoms are expected as a quantum simulator of  $\text{SU}(N)$  Fermi systems. Note that some kinds of fermions, such as Ca, Sr and Yb, naturally realize  $\text{SU}(N)$  systems where the interaction between atoms is isotropic. This is because the spin-degrees of freedom of electrons of such atoms are quenched and the scattering length between atoms is relevant to the electron

spin but irrelevant to  $I$ [38]. Some other kinds of atoms, such as K and Li, where spin degrees of freedom of electrons still remain, could also realize  $SU(N)$  systems by some specific fine-tuning of the magnetic field. We here introduce the important experiment of multicomponent Fermi systems[39]. Using  $^{173}\text{Yb}$  with  $I=5/2$ , the authors reported the realization of the  $SU(6)$  Mott insulating state. Also, in this study, they revealed the mechanism of the large-spin Pomeranchuk cooling which is analogous to Pomeranchuk cooling in solid  $^3\text{He}$ .

It has been shown in the above discussion that spatially disordered optical lattices are successfully realized and quantum degenerate states of fermions with a large nuclear spin are observed. Loading these fermions into a disordered optical lattice, one can realize the multicomponent Fermi systems with spatial disorder. These systems provide a good platform for investigating how spatial disorder affects the rich phase proposed for multicomponent systems.

## 1.2 Fermi systems with spatial inhomogeneity

Spatial inhomogeneity is caused by the impurities mixed into materials, lattice defects, atomic replacement, or so on. It is almost impossible to perfectly omit these elements from realistic solids. Therefore, since P. W. Anderson pointed at the localization of electrons due to spatial disorder in 1958[40], it has been a central issue how spatial nonuniformity affects the properties of the whole system. In the previous section, we have explained that a disordered optical lattice offers a new ground for experimentally investigating the Fermi systems with spatial inhomogeneity. In this section, we introduce the important previous studies of such systems, and then glance at open questions to solve. Also, we concisely describe the aim of our study.

### 1.2.1 Effects of spatial disorder

Anderson localization[40], which strongly influences physical properties, is one of the most interesting phenomena caused by spatial disorder. We here briefly explain the Anderson localization. If a system is in a metallic phase, the wave function of electrons (infinitely) spreads throughout the system. Spatial disorder lessens the spread of the wave function. When the spread of the wave function becomes smaller than the scale of the system, the transition from a metallic phase to an insulating phase (so-called Anderson transition) occurs. We explain the localization of electrons in the case of a tight-binding model with spatial disorder given as,

$$H = -t \sum_{\langle i,j \rangle, \sigma} (C_{i\sigma}^\dagger C_{j\sigma} + h.c.) + \sum_{i, \sigma} \epsilon_i C_{i\sigma}^\dagger C_{i\sigma}, \quad (1.1)$$

where  $C_{i\sigma}$  ( $C_{i\sigma}^\dagger$ ) annihilates (creates) a fermion with spin  $\sigma$  at site  $i$ , and  $n_{i\sigma} = C_{i\sigma}^\dagger C_{i\sigma}$  denotes the number operator.  $t$  and  $\epsilon_i$  represent a hopping amplitude and the random potential caused by spatial nonuniformity, respectively.

If  $\epsilon_i=0$  at all sites (the system is “clean”), the wave function of electrons overall spreads, and hence the existence probability of electrons is independent of sites. To clarify what phenomena occur in the case  $\epsilon_i \neq 0$ , we consider the system including only two lattice sites (site A and B). The Hamiltonian of this systems is rewritten in the matrix representation as follows.

$$H = \sum_{\sigma} \begin{pmatrix} C_{A\sigma}^\dagger & C_{B\sigma}^\dagger \end{pmatrix} \begin{pmatrix} \epsilon_A & -t \\ -t & \epsilon_B \end{pmatrix} \begin{pmatrix} C_{A\sigma} \\ C_{B\sigma} \end{pmatrix}. \quad (1.2)$$

It is easy to diagonalize the above Hamiltonian, and the eigenvalues  $E_{\pm}$  and the eigenfunctions  $\Psi_{\pm} = c_A \phi_A + c_B \phi_B$  are given as,

$$E_{\pm} = \frac{\epsilon_A + \epsilon_B \pm \sqrt{\epsilon^2 + 4t^2}}{2}, \quad (1.3)$$

$$\begin{pmatrix} c_A \\ c_B \end{pmatrix}_{\pm} = \frac{\epsilon \pm \sqrt{\epsilon^2 + 4t^2}}{2t}, \quad (1.4)$$

where we assume  $\epsilon_A < \epsilon_B$  and use the difference between the lattice potentials at each site  $\epsilon = \epsilon_B - \epsilon_A$ . Two opposite limits ( $t \gg \epsilon$  and  $t \ll \epsilon$ ) are considered to understand the properties of the obtained eigenfunctions. In the limit  $t \gg \epsilon$ ,  $c_A \sim \pm c_B$ . This result means that the electron existence probability at each site is almost same as is the case with a clean system. By contrast, the situation dramatically changes in the opposite limit. In  $t \ll \epsilon$ ,  $c_A \gg c_B$  or  $c_A \ll c_B$ . It is found from this result that electrons are localized in one site, and another site is empty.

Based on the knowledge given from the above discussion, the system with many lattice sites is considered. We focus on the spread of the wave function of electrons at a given site and assume that random lattice potentials  $\epsilon_i$  are chosen independently at each site from a rectangular distribution  $[-D/2, D/2]$ . In this case, if  $t \gg \epsilon$  is satisfied, the probability  $P_1$  of the wave function spreading to the nearest-neighbor sites of a given site is roughly estimated as,

$$P_1 \sim \begin{cases} 1 & (t > D), \\ t/D & (t < D), \end{cases} \quad (1.5)$$

where the coefficient of  $P_1$  is neglected because it is not important. Similarly, the probability  $P_2$  of the wave function spreading to the next-nearest-neighbor sites is given as,

$$P_2 \sim \begin{cases} 1 & (t > D), \\ (t/D)^2 & (t < D). \end{cases} \quad (1.6)$$

From the formulas of  $P_1$  and  $P_2$ , we can easily analogize the expressions of  $P_N$  ( $N=1, 2, \dots$ ) in the case  $t < D$  as,

$$P_N \sim \left(\frac{t}{D}\right)^N = \exp\left\{-N \log\left(\frac{D}{t}\right)\right\}. \quad (1.7)$$

This expression means that  $P_N$  exponentially decreases as  $N$  increases, namely the wave function of electrons exponentially decays in the systems with spatial nonuniformity. This exponential decay of the wave functions is characteristic of Anderson localization. Although the above discussion is rough, we can capture the characteristic feature of Anderson localization. This characteristic property is directly observed in the experiments of cold atoms[11, 12, 25], as shown in Fig. 1.6. Note that it is very difficult to observe the exponential decay in solid materials.

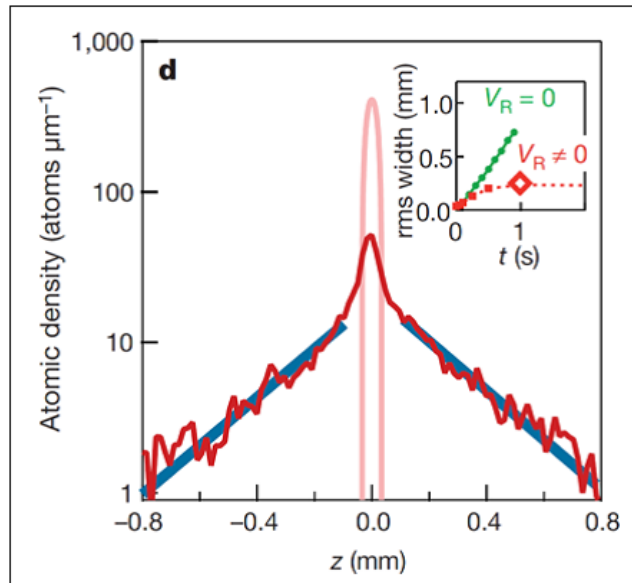


Fig. 1.6 (From [11]) Direct observation of the exponential decay of matter waves due to Anderson localization.

It is not addressed in the above discussion how the dimension  $d$  of systems influences the Anderson localization. This is because this information should be included in the coefficient of  $P_N$ . E. Abrahams *et. al.*[41] analyzed the Anderson localization in details, and thus their scaling theory revealed that infinitesimal spatial disorder induces the localization of electrons in  $d(\leq 2)$ -dimensional systems whereas the metal-Anderson insulator transition occurs at finite critical disorder in the  $d > 2$  case (Fig. 1.7). In the previous study[41], it was clarified that the Anderson transition is of second order. This result was confirmed in experiments of P-doped Si[42] (Fig. 1.8). Also, they indicated the effect of weak localization which is appreciated as the precu-

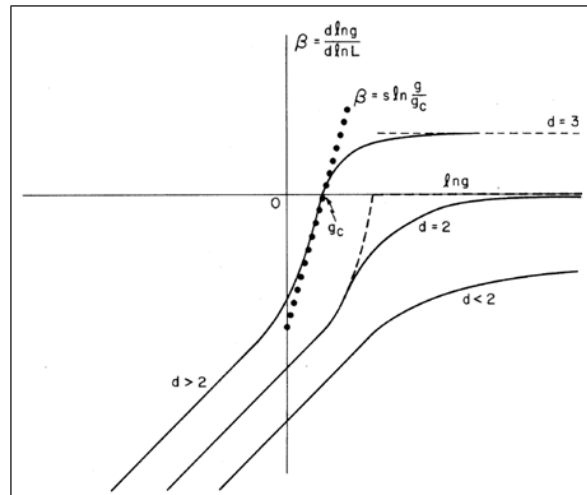


Fig. 1.7 (From [41]) Results given by scaling theory.  $\beta = \ln g(L) / \ln L$ , where  $g(L)$  represents a conductance and  $L$  a one-dimensional size of a  $d$ -dimensional hypercube.

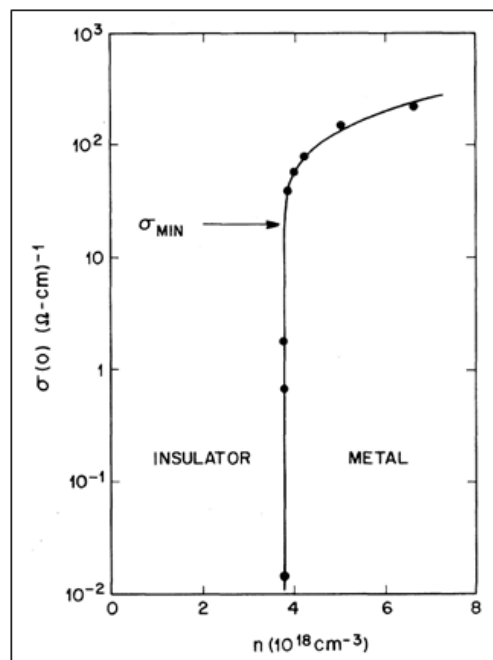


Fig. 1.8 (From [42]) Conductance  $\sigma(0)$  as a function of a donor density  $n$  at extremely low temperature.  $\sigma_{\text{MIN}}$  denotes the finite minimum conductance predicted by N. F. Mott[43]. It is seen that  $\sigma(0)$  takes the smaller value than  $\sigma_{\text{MIN}}$ , and this result ensures that the Anderson transition is of second order.

sor phenomenon of Anderson localization. The weak localization is the phenomenon that in a two-dimensional finite system, the conductance decreases with increase of a one-dimensional size of the system with spatial disorder although the system is in a metallic phase. The effect of weak localization can be experimentally observed by measuring the response of the conductance for the change of magnetic field. This is because the magnetic field breaks the time-reversal symmetry which the system has, and thus the backscattering effect due to spatial nonuniformity is weakened[44]. Indeed, this phenomenon was experimentally observed by Kawaguchi *et. al.*[45] (Fig. 1.9).

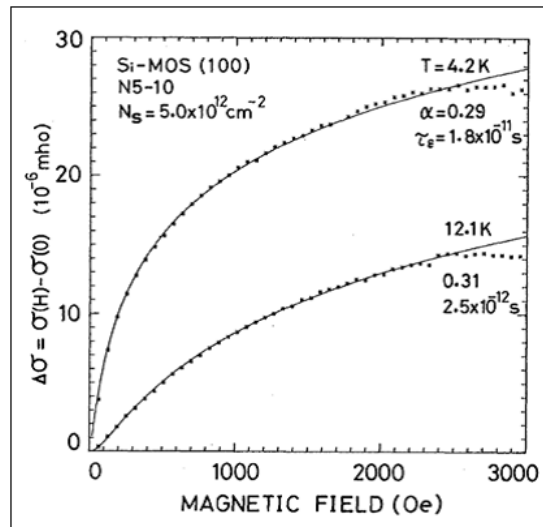


Fig. 1.9 (From [45]) Response of the conductance  $\sigma(H)$  for the change of magnetic field  $H$ . We find that the conductance increases as  $H$  increases.

## 1.2.2 How do interaction and spatial disorder compete/collaborate with each other?

The interaction between electrons always influences the properties of realistic materials as is the case with spatial disorder. Therefore, in order to clarify the properties of realistic solids more properly, we should consider how interaction and spatial disorder compete/collaborate with each other and how the competition/collaboration affects the properties of systems. Although it is very difficult to exactly treat both of spatial disorder and interaction on equal footing, marked approximate methods help us to address on these important issues. Note that we do not describe the detailed explanation of the approximate methods here, and they are written in Chap. 2. In this section, we represent only the results demonstrated in the important previous studies.

The Mott transition is one of the most interesting phenomena realized in strongly-correlated electron systems. The authors investigated how spatial inhomogeneity influences the formation of a Mott insulator in Ref. [46]. Thereby, the ground state phase diagram of the Anderson-Hubbard model at zero temperature and at half-filling was determined, as plotted in Fig. 1.10. We can find from this phase diagram that

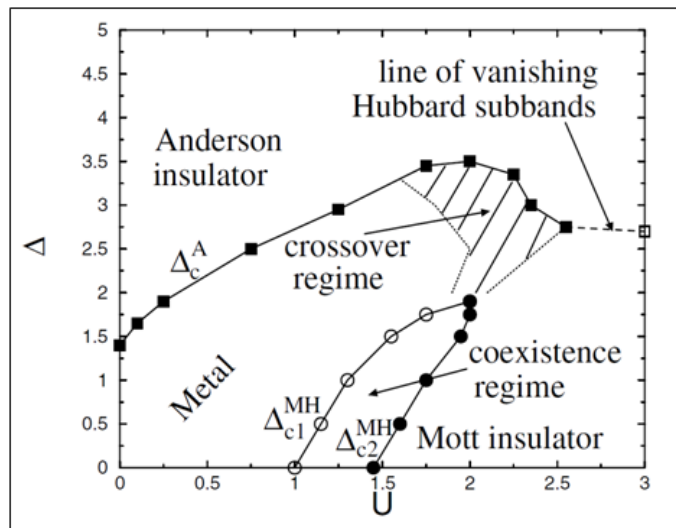


Fig. 1.10 (From [46]) ground state phase diagram of an Anderson-Hubbard model at zero temperature and at half-filling. The vertical (horizontal) axis shows the disorder (repulsive interaction) strength. This result is given by a typical medium theory.

the metal-Mott transition points increase with increasing the disorder strength. Also, the metal-Anderson insulator transition points increase as a repulsive interaction increases in weakly-interacting regions. These results mean that spatial inhomogeneity competes against correlation effects, and both effects mutually suppress each other.

Ordered states in correlated systems with spatial nonuniformity have been also analyzed. An antiferromagnetic state in spatially disordered systems was studied by using a typical medium theory[47] and it was indicated in the previous study that spatial disorder breaks an antiferromagnetic order and triggers a transition from an antiferromagnetic insulator to a paramagnetic metal (Fig. 1.11). Moreover, the authors suggested that the antiferromagnetic metal realizes in narrow regions. In other previous study[48], the authors investigated the attractively interacting Fermi systems with spatial disorder by using the determinant quantum Monte Carlo method. They calculated the charge structure factor associated with the checkerboard-type charge-density-wave state, and the pair structure factor associated with the  $s$ -wave superfluid state in two dimensional square lattices. Their results indicate that the charge-density-wave state is strongly influenced by spatial disorder whereas disorder

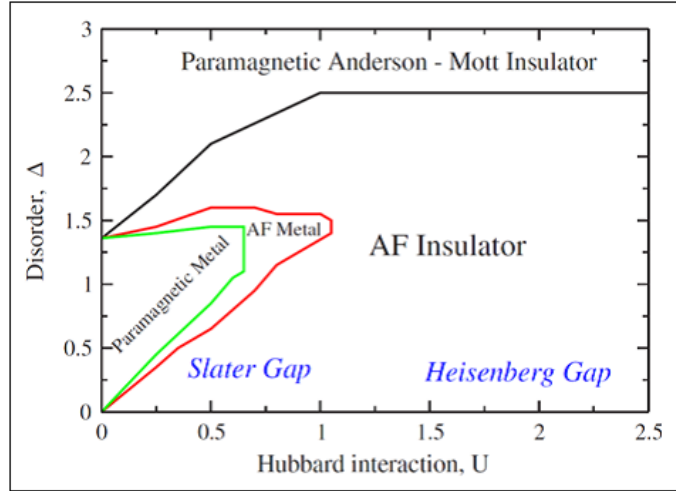


Fig. 1.11 (From [47]) Magnetic phase diagram of the model with on-site interaction and diagonal disorder. The vertical and horizontal axes represent the disorder and the interaction strength, respectively.

does not affect a pair correlation very much (see Fig. 1.12). The result means that

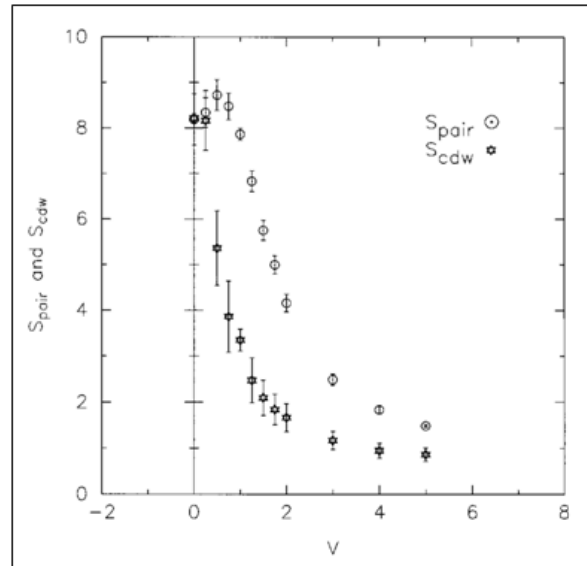


Fig. 1.12 (From [48]) Charge structure factor  $S_{cdw}$  and pair structure factor  $S_{pair}$  as a function of the disorder strength  $V$ .

although the charge-density-wave state and the  $s$ -wave superfluid state are degenerate in two dimensional square lattices without spatial disorder, only the  $s$ -wave superfluid state is stabilized as the ground state of the Anderson-Hubbard model if the systems are subject to spatial disorder.

### 1.2.3 Superfluidity in spatially disordered systems

We would like to explain in more detail the quantum phenomena observed in attractively interacting systems with diagonal disorder, which is well-described by an Anderson-Hubbard model. In the previous subsection, it has been shown that the superfluid state might realize as the ground state of the Anderson-Hubbard model. The superfluidity in disordered systems has been studied since 1959, when P. W. Anderson suggested that nonmagnetic impurities hardly affect the characters of  $s$ -wave superfluidity whereas  $s$ -wave superfluidity is strongly influenced by magnetic impurities (for examples, the transition temperature to the superfluid state decreases with increasing the concentration of magnetic impurities.)[49]. It is known that this statement is true if the spatial nonuniformity caused by nonmagnetic impurities is weak. On the other hand, it is experimentally observed in disordered thin films[50, 51, 52, 53, 54, 55, 56] that the strong disorder by nonmagnetic impurities breaks down the superfluidity, and stabilizes the states with a pseudogap at the Fermi level. This superfluid-insulator transition is well captured by a Bogoliubov-de Gennes (BdG) method[57]. Here, we would like to introduce several important papers[58, 59, 60, 61, 62, 63]. Using the BdG method in these papers, the authors investigated the low-dimensional systems with attractive interaction and non-magnetic disorder. Thereby, it was reported that the long-range order in the superconducting state, which is stabilized as the ground state, is gradually weakened with increase of the disorder strength. It was also clarified that when the correlation length of the superconducting order becomes shorter than the lattice size at a critical disorder strength (see Fig.1.13), the superconducting states undergo a transition to the insulating states where the regions with and without the pair correlation coexist. The properties of the insulating state uncovered by the BdG method agree rather well with the results of the experiments of disordered thin films.

## 1.3 Open questions of spatially disordered systems

We approach two important issues and report the results of them in this thesis. One is how quantum fluctuations influence the properties of the two-component Fermi systems with on-site attractive interaction and diagonal disorder, and the other is what quantum phenomena should be observed in multicomponent attractively-interacting Fermi systems with diagonal disorder. Note that the aims of our study are described in detail in Chaps. 3 and 4, and we concisely explain them here.

First, we explain the issue about the two-component Fermi systems. As mentioned above, attractive Fermi systems with spatial disorder have been investigated

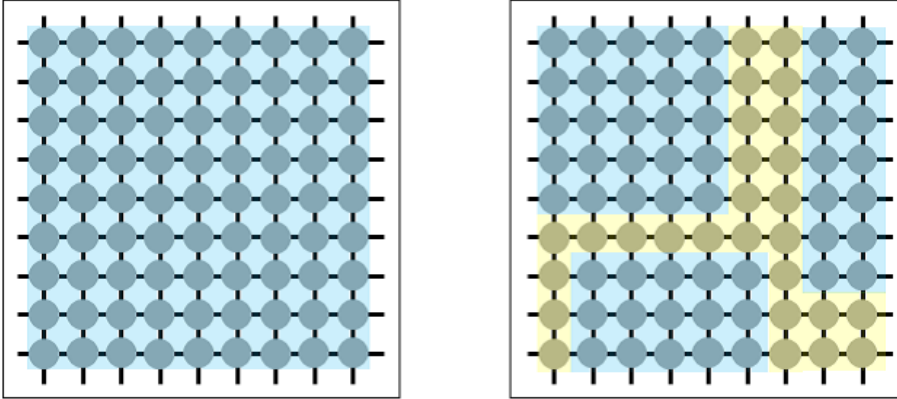


Fig. 1.13 Superconducting states in clean or weakly disordered systems (left panel) and insulating states in strongly disordered systems (right panel). The graphic filled with dilute aqua (yellow) represents the regions where the pair correlation develops (does not exist).

by using numerical methods, such as a BdG method. Thereby the disorder-induced superfluid-insulator transition was uncovered. The BdG method is the simpler numerical method, but still gives us a fruitful insight. However, this method cannot capture the change of the properties of the systems caused by quantum fluctuations because it treats the interaction within the static mean-field level. The attractively interacting systems have been investigated by using the dynamical mean-field theory[64], which can successfully treat local quantum fluctuations[65, 66]. In these studies[65, 66], the importance to treat the local quantum fluctuations in attractive Fermi systems was discussed. Therefore, using the numerical method which can treat the effects of quantum fluctuations in addition to spatial nonuniformity, we investigate the attractive Fermi systems with spatial disorder to obtain complete understandings of such systems. This is one of the main purposes of our studies.

Based on the knowledge which is obtained in the study of the two-component Fermi systems, we investigate the multicomponent Fermi systems with spatial disorder. There are many theoretical studies of the multicomponent systems[67, 68, 69, 70, 71, 72, 73, 74, 75, 76, 77, 78, 79, 80, 81]. Using a mean-field method and an one-loop renormalization group, C. Honerkamp and W. Hofstetter demonstrated that the rich phases, such as a flavor-density wave state, an anomalous superfluid state, and a staggered flux state (see Fig. 1.14), could be realized as the ground state at zero temperature in  $SU(N)$  systems[69, 70]. Also, they indicated that if  $N > 2$ , only the density-wave state is stabilized as the ground state at zero temperature and at half-filling (one atom per site in average) in two-dimensional square lattices whereas the superfluid state and the density-wave state are degenerate on these conditions in  $SU(2)$  attractive Fermi systems. From this result and the result that only the

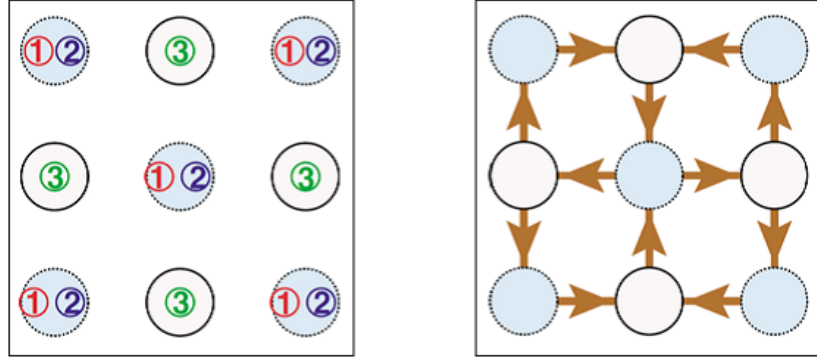


Fig. 1.14 Flavor-density wave state in  $SU(3)$  Fermi systems (left panel) and staggered flux state in  $SU(N>6)$  Fermi systems (right panel). Numbers denote the spins and arrows the particle currents. These figures are reprinted from Ref. [69]

$s$ -wave superfluid state is stabilized as the ground state of the  $SU(2)$  Anderson-Hubbard model corresponding to the  $SU(2)$  Fermi systems with diagonal disorder, an important issue, what kind of state is realized as the ground state in the  $SU(N>2)$  systems with disorder, arises. We investigate the  $SU(N>2)$  Fermi systems with spatial disorder to clarify this issue.

## Chapter 2

# Numerical calculation method

In this chapter, we describe the details of the numerical methods and introduce some previous studies which demonstrate the novel results by using these methods. To successfully treat both of spatial inhomogeneity and interaction between particles, a statistical dynamical mean-field theory (statistical DMFT)[82, 83, 84] and a Bogoliubov-de Gennes (BdG) method[57] are employed in these studies. First, the formalism of the statistical DMFT is presented, and that of the BdG method follows.

### 2.1 Statistical dynamical mean-field theory

In this section, we explain the two important methods named a dynamical mean-field theory (DMFT)[64] and a coherent potential approximation (CPA)[85, 86] before the explanation of a statistical dynamical mean-field theory (statistical DMFT). The statistical DMFT is an extension of these two methods, and thus the explanation of these methods might be helpful for understanding the statistical DMFT. The way to treat backscattering effects within the scheme of the DMFT is discussed after the explanations of the DMFT and the CPA, and we describe the details of the statistical DMFT. At the end of this section, the self-consistent loop of the extended statistical DMFT which is extended to analyze attractively interacting systems with spatial inhomogeneity is dilated and the explanation of the modified iterative perturbation theory[87, 88] which is used as an impurity solver in this study follows.

#### 2.1.1 Dynamical mean-field theory

The interaction between electrons often plays a main role for the physical phenomena occurring in solids. However, the case in which we can exactly treat the effects of an interaction is very limited, and hence how we should treat the effects of an interaction has been a central issue in solid state physics. The dynamical mean-field theory (DMFT)[64] is one of the methods which had been developed to deal with the

correlation between electrons. Using the DMFT, we can successfully treat the effect of local correlation. The basic idea of the DMFT is to map a target lattice model into an effective single-impurity model for which many methods have been developed (see Fig. 2.1). The microscopic derivation of DMFT in the case of the Hubbard model is as follows.

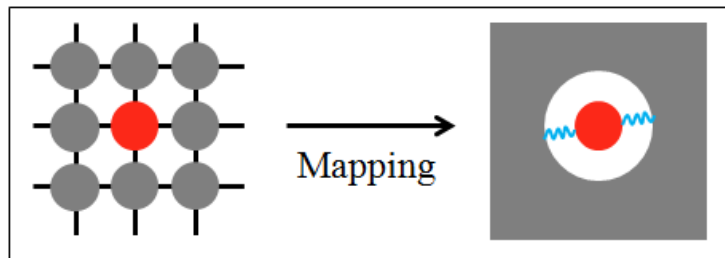


Fig. 2.1 Schematic picture of mapping a target lattice model into an effective single-impurity model in the scheme of the DMFT. The red circle represents the site “0” and the ash circles the other sites in the left figure. In the right figure, the red circle represents a single impurity which is coupled with the electron bath described by the graphic filled with ash.

The Hubbard model is expressed as,

$$H = - \sum_{i,j,\sigma} t_{ij} (C_{i\sigma}^\dagger C_{j\sigma} + h.c.) - \mu \sum_{i,\sigma} n_{i\sigma} + U \sum_i n_{i\uparrow} n_{i\downarrow}. \quad (2.1)$$

$\mu$  and  $U$  represent a chemical potential and an on-site interaction between particles, respectively. The partition function  $Z$  and the action  $S$  for this model are given as,

$$Z = \int \prod_{i,\sigma} \mathcal{D}C_{i\sigma}^\dagger \mathcal{D}C_{i\sigma} e^{-S}, \quad (2.2)$$

$$S = \int_0^\beta d\tau \left\{ \sum_{i,j,\sigma} C_{i\sigma}^\dagger(\tau) \left[ \left( \frac{\partial}{\partial \tau} - \mu \right) \delta_{ij} + t_{ij} \right] C_{j\sigma}(\tau) + U \sum_i n_{i\uparrow}(\tau) n_{i\downarrow}(\tau) \right\}. \quad (2.3)$$

Here, we focus on a given site (we call this site to the site “0”.) and decompose the action  $S$  to a part of the action which is relevant to the site “0”  $S_0$ , that of the action which is relevant to the hopping between the site “0” and the other sites  $\Delta S$ , and

that of the action which is relevant to the other sites except for the site “0”  $S^{(0)}$ .

$$S = S_0 + \Delta S + S^{(0)}, \quad (2.4)$$

$$S_0 = \int_0^\beta d\tau \left\{ \sum_\sigma C_{0\sigma}^\dagger(\tau) \left( \frac{\partial}{\partial \tau} - \mu \right) C_{0\sigma}(\tau) + U n_{0\uparrow}(\tau) n_{0\downarrow}(\tau) \right\}, \quad (2.5)$$

$$\Delta S = \int_0^\beta d\tau \left\{ \sum_{i,\sigma} \left[ t_{i0} C_{i\sigma}^\dagger(\tau) C_{0\sigma}(\tau) + t_{0i} C_{0\sigma}^\dagger C_{i\sigma}(\tau) \right] \right\}, \quad (2.6)$$

$$S^{(0)} = \int_0^\beta d\tau \left\{ \sum_{i,j \neq 0, \sigma} C_{i\sigma}^\dagger(\tau) \left[ \left( \frac{\partial}{\partial \tau} - \mu \right) \delta_{ij} + t_{ij} \right] C_{j\sigma}(\tau) + U \sum_{i \neq 0} n_{i\uparrow}(\tau) n_{i\downarrow}(\tau) \right\}. \quad (2.7)$$

By substituting the above decomposed actions into Eq.(2.2), we rewrite the formula of  $Z$  as,

$$\begin{aligned} Z &= \int \prod_{i,\sigma} \mathcal{D}C_{i\sigma}^\dagger \mathcal{D}C_{i\sigma} e^{-S_0 - \Delta S - S^{(0)}} \\ &= \int \mathcal{D}C_{0\sigma}^\dagger \mathcal{D}C_{0\sigma} e^{-S_0} \int \prod_{i \neq 0, \sigma} \mathcal{D}C_{i\sigma}^\dagger \mathcal{D}C_{i\sigma} e^{-\Delta S - S^{(0)}}. \end{aligned} \quad (2.8)$$

Here, we define a statistical average of  $e^{-\Delta S}$  as,

$$\langle e^{-\Delta S} \rangle^{(0)} = \frac{1}{Z^{(0)}} \int \prod_{i \neq 0, \sigma} \mathcal{D}C_{i\sigma}^\dagger \mathcal{D}C_{i\sigma} e^{-\Delta S} e^{-S^{(0)}}, \quad (2.9)$$

$$Z^{(0)} = \int \prod_{i \neq 0, \sigma} \mathcal{D}C_{i\sigma}^\dagger \mathcal{D}C_{i\sigma} e^{-S^{(0)}}. \quad (2.10)$$

$Z$  is rewritten by using the above formula of  $\langle e^{-\Delta S} \rangle^{(0)}$  as,

$$Z = Z^{(0)} \int \mathcal{D}C_{0\sigma}^\dagger \mathcal{D}C_{0\sigma} e^{-S_0} \langle e^{-\Delta S} \rangle^{(0)}. \quad (2.11)$$

In order to map a lattice model into an effective single impurity model, we have to integrate the degrees of freedom at the other sites, i.e. to calculate the integration of  $C_{i\sigma}$  and  $C_{i\sigma}^\dagger$  in Eq.(2.9). For this purpose,  $\langle e^{-\Delta S} \rangle^{(0)}$  is decomposed by using the Taylor series expansion as,

$$\langle e^{-\Delta S} \rangle^{(0)} = 1 - \langle \Delta S \rangle^{(0)} + \frac{1}{2} \langle (\Delta S)^2 \rangle^{(0)} - \frac{1}{6} \langle (\Delta S)^3 \rangle^{(0)} + \dots \quad (2.12)$$

The first-order term,  $\langle \Delta S \rangle^{(0)}$ , reads

$$\begin{aligned}
\langle \Delta S \rangle^{(0)} &= \frac{1}{Z^{(0)}} \int \prod_{i \neq 0, \sigma} \mathcal{D}C_{i\sigma}^\dagger \mathcal{D}C_{i\sigma} (\Delta S) e^{-S^{(0)}} \\
&= \frac{1}{Z^{(0)}} \int \prod_{i \neq 0, \sigma} \mathcal{D}C_{i\sigma}^\dagger \mathcal{D}C_{i\sigma} \int_0^\beta d\tau \sum_{i, \sigma} \left[ t_{i0} C_{i\sigma}^\dagger(\tau) C_{0\sigma}(\tau) + t_{0i} C_{0\sigma}^\dagger(\tau) C_{i\sigma}(\tau) \right] e^{-S^{(0)}} \\
&= \int_0^\beta d\tau \sum_{i, \sigma} \left[ t_{i0} \langle C_{i\sigma}^\dagger(\tau) \rangle^{(0)} C_{0\sigma}(\tau) + t_{0i} C_{0\sigma}^\dagger(\tau) \langle C_{i\sigma}(\tau) \rangle^{(0)} \right]. \tag{2.13}
\end{aligned}$$

The statistical averages  $\langle C_{i\sigma}^\dagger(\tau) \rangle^{(0)}$  and  $\langle C_{i\sigma}(\tau) \rangle^{(0)}$  in the above formula vanish from the particle conservation-law. Therefore, the contribution of the first-order term becomes zero. Similarly, all the contributions which arise from the odd-order terms are also equal to zero.

The second-order term  $\langle (\Delta S)^2 \rangle^{(0)}/2$  is discussed. Calculating  $\langle (\Delta S)^2 \rangle^{(0)}/2$  with due considerations to the particle conservation-law, we obtain the following formula given by the two point Green function  $\langle T_\tau C_{i\sigma}(\tau_1) C_{j\sigma}^\dagger(\tau_2) \rangle^{(0)}$ .

$$\begin{aligned}
\frac{1}{2} \langle (\Delta S)^2 \rangle^{(0)} &= \frac{1}{2Z^{(0)}} \int \prod_{i \neq 0, \sigma} \mathcal{D}C_{i\sigma}^\dagger \mathcal{D}C_{i\sigma} (\Delta S)^2 e^{-S^{(0)}} \\
&= \int_0^\beta d\tau_1 \tau_2 \sum_{i, j, \sigma} \left\{ t_{0i} t_{j0} C_{0\sigma}^\dagger(\tau_1) \langle T_\tau C_{i\sigma}(\tau_1) C_{j\sigma}^\dagger(\tau_2) \rangle^{(0)} C_{0\sigma}(\tau_2) \right\}. \tag{2.14}
\end{aligned}$$

It may be impossible to explicitly evaluate the contributions arise from high-order terms. Therefore, we adopt the approximation which becomes exact if a spatial dimension  $d$  is infinite, and the contributions under this approximation are discussed here. To avoid the divergence of a band width in  $d \rightarrow \infty$ , a hopping amplitude  $t_{ij}$  is rescaled as  $t_{ij} \rightarrow t_{ij}/\sqrt{d}$ . Here, we consider the contribution of the second-order term under this scaling  $t_{ij} \rightarrow t_{ij}/\sqrt{d}$ . The order of each part in the second-order term is estimated as follows.  $t_{i0} t_{0j} \rightarrow 1/d$ ,  $\sum_{i, j} \rightarrow d^2$ , and  $\langle T_\tau C_{i\sigma}(\tau_1) C_{j\sigma}^\dagger(\tau_2) \rangle^{(0)} \rightarrow 1/d$ . The product of these terms is of order 1, and hence the contribution arising from the second-order term cannot be truncated even when  $d \rightarrow \infty$ . Through a similar argument, the contribution of the  $n$ -th ( $n$  is even and larger than 2.) order term is estimated. We would like to note again here that the contribution of the odd-order term becomes equal to zero due to a particle conservation law. The  $n$ -th order term may be composed of the product of  $t_{0i}^{n/2}$  and  $t_{i0}^{n/2}$ , summations  $\sum_{i_1, i_2, \dots, i_n}$ , and  $n$ -point Green functions. Here, the  $n$ -point Green function is decomposed into the term of the product of only two-point Green functions, i.e. the term including no vertices and the terms including some vertices. The product of  $t$ , summations, the term

including no vertices, and the term including some vertices are of order  $d^{-n/2}$ ,  $d^n$ ,  $d^{-n/2}$ , and  $d^{1-n}$ , respectively. Therefore, the term which is relevant to the product of only two-point Green functions is of order 1. By contrast, that of the term which is relevant to the part including some vertices becomes  $d^{1-n/2}$ . From these arguments, it is found that the contribution of the higher-order terms arises only from the terms of the product of two-point Green functions under  $d \rightarrow \infty$ .

It is found from the above discussion that when  $d \rightarrow \infty$ ,  $\langle e^{-\Delta S} \rangle^{(0)}$  should be described as,

$$\begin{aligned} \langle e^{-\Delta S} \rangle^{(0)} &= 1 - \int_0^\beta d\tau_1 \tau_2 \sum_{i,j,\sigma} \left\{ t_{0i} t_{j0} C_{0\sigma}^\dagger(\tau_1) G_{ij\sigma}^{(0)}(\tau_1 - \tau_2) C_{0\sigma}(\tau_2) \right\} + \dots \\ &= \exp \left[ - \int_0^\beta d\tau_1 \tau_2 \sum_{i,j,\sigma} \left\{ t_{0i} t_{j0} C_{0\sigma}^\dagger(\tau_1) G_{ij\sigma}^{(0)}(\tau_1 - \tau_2) C_{0\sigma}(\tau_2) \right\} \right], \end{aligned} \quad (2.15)$$

where  $G_{ij\sigma}^{(0)}(\tau_1 - \tau_2) (= \langle T_\tau C_{i\sigma}(\tau_1) C_{j\sigma}^\dagger(\tau_2) \rangle^{(0)})$  is a two-point Green function. By substituting Eq.(2.11) with Eq.(2.15), the formula of the partition function  $Z$  is obtained as,

$$\begin{aligned} Z &= Z^{(0)} \int \mathcal{D}C_{0\sigma}^\dagger \mathcal{D}C_{0\sigma} e^{-S_0} \exp \left\{ - \int_0^\beta d\tau_1 d\tau_2 \sum_\sigma C_{0\sigma}^\dagger(\tau_1) \left[ \sum_{i,j} t_{i0} t_{0j} G_{ij\sigma}^{(0)}(\tau_1 - \tau_2) \right] C_{0\sigma}(\tau_2) \right\} \\ &= Z^{(0)} Z_0. \end{aligned} \quad (2.16)$$

As seen above, we can decompose the partition function  $Z$  to the term which is relevant to the site “0” ( $Z_0$ ) and the term which is relevant to the other sites except for the site “0” ( $Z^{(0)}$ ). Here,  $Z_0$  is defined as  $Z_0 = \int \mathcal{D}C_{0\sigma}^\dagger \mathcal{D}C_{0\sigma} e^{-S_{\text{eff}}}$ . Thereby, the effective action  $S_{\text{eff}}$  is described as,

$$\begin{aligned} S_{\text{eff}} &= S_0 + \int_0^\beta d\tau_1 d\tau_2 \sum_\sigma C_{0\sigma}^\dagger(\tau_1) \left[ \sum_{i,j} t_{i0} t_{0j} G_{ij\sigma}^{(0)}(\tau_1 - \tau_2) \right] C_{0\sigma}(\tau_2) \\ &= \int_0^\beta d\tau \left\{ \sum_\sigma C_{0\sigma}^\dagger(\tau) \left( \frac{\partial}{\partial \tau} - \mu \right) C_{0\sigma}(\tau) + U n_{0\uparrow}(\tau) n_{0\downarrow}(\tau) \right\} \\ &\quad + \int_0^\beta d\tau_1 d\tau_2 \sum_\sigma C_{0\sigma}^\dagger(\tau_1) \left[ \sum_{i,j} t_{i0} t_{0j} G_{ij\sigma}^{(0)}(\tau_1 - \tau_2) \right] C_{0\sigma}(\tau_2) \\ &= - \int_0^\beta d\tau_1 d\tau_2 \sum_\sigma C_{0\sigma}^\dagger(\tau_1) \mathcal{G}_\sigma^{-1}(\tau_1 - \tau_2) C_{0\sigma}(\tau_2) + U \int_0^\beta d\tau n_{0\uparrow}(\tau) n_{0\downarrow}(\tau), \end{aligned} \quad (2.17)$$

where  $\mathcal{G}_\sigma^{-1}(\tau_1 - \tau_2)$  expresses a dynamically fluctuating field and is calculated from

the statistical average of the degrees of freedom except for the site “0” as,

$$\mathcal{G}_\sigma^{-1}(\omega) = \omega + \mu - \sum_{i,j} t_{i0} t_{0j} G_{ij\sigma}^{(0)}(\omega). \quad (2.18)$$

Thus,  $S_{\text{eff}}$  should be regarded as the effective action of the systems where the single impurity is subject to a local interaction couples to a particle bath.

The procedure to map a target lattice model to a single-impurity model, i.e. the basic strategy of a DMFT, has been explained up to this point. Here, we introduce the self-consistent equations for the effective action  $\mathcal{G}_\sigma^{-1}(\omega)$ . As already described,  $\mathcal{G}_\sigma^{-1}(\omega)$  is defined by  $G_{ij\sigma}^{(0)}(\omega)$ . This  $G_{ij\sigma}^{(0)}(\omega)$  is related to the “normal” Green function  $G_{ij\sigma}(\omega)$  (here, “normal” means including the site “0”) as,

$$G_{ij\sigma}(\omega) = G_{ij\sigma}^{(0)}(\omega) + G_{i0\sigma}(\omega) G_{00\sigma}^{-1}(\omega) G_{0j\sigma}(\omega), \quad (2.19)$$

where  $G_{00\sigma}(\omega)$  is a local Green function. Eq.(2.19) is derived from the following consideration.  $G_{ij\sigma}(\omega)$  denotes the propagation of the particle from a site  $i$  to a site  $j$ . The routes on which particles are propagated by  $G_{ij\sigma}(\omega)$  include the routes on which particles pass through the site “0” and the routes on which particles do not pass through the site “0”.  $G_{ij\sigma}^{(0)}(\omega)$  shows only the routes on which particles do not pass the site “0” in all routes. From the above discussion, it is easily understood that the relation between  $G_{ij\sigma}(\omega)$  and  $G_{ij\sigma}^{(0)}(\omega)$  is given by Eq.(2.19). Also, there are innumerable routes from a site “ $i$ ” to a site “ $j$ ”, but the contribution from the propagation on the routes, where particles go a long way round, is equal to zero when  $d \rightarrow \infty$  due to the extra hopping. From this statement,

$$\begin{aligned} \sum_{ij} t_{i0} t_{0j} G_{ij\sigma}^{(0)}(\omega) &= \sum_{ij} t_{i0} t_{0j} \{G_{ij\sigma}(\omega) - G_{i0\sigma}(\omega) G_{00\sigma}^{-1}(\omega) G_{0j\sigma}(\omega)\} \\ &= \sum_{ij} t_{i0} t_{0j} G_{ij\sigma}(\omega) - \left\{ \sum_i t_{i0} G_{i0\sigma}(\omega) \right\} G_{00\sigma}^{-1}(\omega) \left\{ \sum_j t_{0j} G_{0j\sigma}(\omega) \right\} \end{aligned} \quad (2.20)$$

is derived.

By substituting Eq.(2.20) by Eq.(2.18), the relation between the Green function of an effective field and a lattice Green function is obtained, but Eq.(2.20) is not practical. To derive a practical formula, the right side of Eq.(2.20) is rewritten by Fourier transformation.

$$\begin{aligned} &\sum_{ij} t_{i0} t_{0j} G_{ij\sigma}(\omega) - \left\{ \sum_i t_{i0} G_{i0\sigma}(\omega) \right\} G_{00\sigma}^{-1}(\omega) \left\{ \sum_j t_{0j} G_{0j\sigma}(\omega) \right\} \\ &= \frac{1}{M} \sum_k \epsilon_k^2 G_{k\sigma}(\omega) - \left\{ \frac{1}{M} \sum_k \epsilon_k G_{k\sigma}(\omega) \right\} G_{00\sigma}^{-1}(\omega) \left\{ \frac{1}{M} \sum_k \epsilon_k G_{k\sigma}(\omega) \right\}, \end{aligned} \quad (2.21)$$

where  $\epsilon_k = \sum_{ij} t_{ij} e^{ik(R_i - R_j)}$  ( $R_i$  represents the coordinate of sites) and  $M$  denotes the number of lattice sites. From the Dyson equation for  $G_{k\sigma}(\omega)$ , the relation between  $G_{k\sigma}(\omega)$  and  $\epsilon_k$  is derived as,

$$\begin{aligned} G_{k\sigma}^{-1}(\omega) &= \tilde{G}_{k\sigma}^{-1}(\omega) - \Sigma_{k\sigma}(\omega) \\ G_{k\sigma}(\omega) &= \frac{1}{\omega + \mu - \epsilon_k - \Sigma_{k\sigma}(\omega)} \\ &= \frac{1}{\omega + \mu - \epsilon_k - \Sigma_{\sigma}(\omega)}. \end{aligned} \quad (2.22)$$

Here,  $\tilde{G}_{k\sigma}(\omega)$  denotes a non-perturbative Green function and  $\Sigma_{k\sigma}(\omega)$  a self-energy. The last equation in Eq.(2.22) is given from the fact that the self-energy is independent of a wave number when  $d \rightarrow \infty$ . We find from Eq.(2.22) that the dependence on  $k$  of  $G_{k\sigma}(\omega)$  is determined only from the dispersion relation  $\epsilon_k$ . By solving Eq.(2.22) for  $\epsilon_k$ , the following formula is obtained.

$$\epsilon_k = \omega + \mu - \Sigma_{\sigma}(\omega) - G_{k\sigma}^{-1}(\omega). \quad (2.23)$$

$\frac{1}{M} \sum_k \epsilon_k^2 G_{k\sigma}(\omega)$  and  $\frac{1}{M} \sum_k \epsilon_k G_{k\sigma}(\omega)$  in Eq.(2.21) are calculated by using Eq.(2.23) as,

$$\frac{1}{M} \sum_k \epsilon_k^2 G_{k\sigma}(\omega) = -(\omega + \mu - \Sigma_{\sigma}(\omega)) + (\omega + \mu - \Sigma_{\sigma}(\omega))^2 G_{00\sigma}(\omega), \quad (2.24)$$

$$\frac{1}{M} \sum_k \epsilon_k G_{k\sigma}(\omega) = -1 + (\omega + \mu - \Sigma_{\sigma}(\omega)) G_{00\sigma}(\omega), \quad (2.25)$$

where  $\frac{1}{M} \sum_k \epsilon_k = t_{00} = 0$  and  $\frac{1}{M} \sum_k G_{k\sigma}(\omega) = G_{00\sigma}(\omega)$  are used. By substituting the equations derived here into Eqs.(2.20) and (2.21),

$$\sum_{ij} t_{i0} t_{0j} G_{ij\sigma}^{(0)}(\omega) = \omega + \mu - \Sigma_{\sigma}(\omega) - G_{00\sigma}^{-1}(\omega) \quad (2.26)$$

is obtained. Thus, the self-consistent equation of  $\mathcal{G}_{\sigma}^{-1}(\omega)$  is given as,

$$\mathcal{G}_{\sigma}^{-1}(\omega) = G_{00\sigma}^{-1}(\omega) + \Sigma_{\sigma}(\omega). \quad (2.27)$$

This self-consistent equation is the same as the Dyson equation for an effective single-impurity model.

The self-consistent loop of a DMFT is as follows:

- (i) Choose proper  $\Sigma_{\sigma}(\omega)$  as an initial state. (In most cases, there are no problems if the Hartree-Fock self-energy is chosen.)

- (ii) Calculate the local Green function  $G_{00\sigma}(\omega)$  from Eq.(2.22) and

$$G_{00\sigma}(\omega) = \frac{1}{M} \sum_k G_{k\sigma}(\omega). \quad (2.28)$$

- (iii) Calculate the cavity Green function  $\mathcal{G}_\sigma^{-1}(\omega)$  from Eq.(2.27).  
 (iv) Using an impurity solver, update the self-energy  $\Sigma_\sigma(\omega)$ .

Steps (i)—(iv) are iterated until self-consistency is achieved.

### 2.1.2 Coherent potential approximation

In the previous subsection, we have addressed the derivation and the basic procedure of DMFT. The basic idea of the DMFT is that we integrate the many degrees of freedom except for that about a single site and map the target systems into the systems with a few degrees of freedom. This spirit is the same as that of a coherent potential approximation (CPA)[85, 86, 89, 90, 91]. As described in the previous subsection, the DMFT has been developed to treat local correlation. On the other hand, the CPA has been developed to investigate the lattice systems without a periodic structure as exemplified by alloys, doped semiconductors, amorphous solids, or the systems in which a lattice potential is spatially disordered due to impurities. The systems without periodic structure might be described by the Hamiltonian with site-diagonal disorder,

$$H = - \sum_{i,j,\sigma} t_{ij} (C_{i\sigma}^\dagger C_{j\sigma} + h.c.) - \sum_{i,\sigma} (\mu - \epsilon_i) n_{i\sigma} + U \sum_i n_{i\uparrow} n_{i\downarrow}. \quad (2.29)$$

The systems described by this Hamiltonian is more difficult to analyze than the systems with periodic structure because we cannot use many remarkable techniques which have been developed for analyzing the systems with periodic structure. Thus, in the CPA, we approximate the systems without periodic structure by the systems with periodic structure by introducing an effective lattice-potential (see Fig. 2.2).

Thanks to the analogy between the scheme of the CPA and the DMFT, it is easy to combine these methods. Thus, the correlated systems with disorder have been extensively analyzed by using a CPA+DMFT method[92, 93, 94, 95, 96, 97, 98, 99, 100]. In this thesis, a microscopic deviation of a CPA+DMFT method in the case of the model written in Eq.(2.29) is not described because it is almost same as that of a standard DMFT. We just show the steps of the self-consistent loop of a CPA+DMFT below.

- (i) Start calculations from the suitable  $\Sigma_\sigma(\omega)$  and the hybridization function  $\eta_\sigma(\omega)$ .

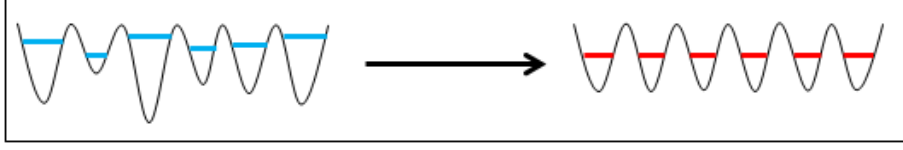


Fig. 2.2 Schematic picture of the basic procedure of a CPA. The black lines represent the potential caused by atoms, impurities, and so on. The left figure shows the systems without periodic structure and the right figure those with periodic structure.  $(\mu - \epsilon_i)$  in Eq.(2.29) is represented by the blue lines in the left figure. The red lines in right figure denote the effective potential explained in the text.

- (ii) Calculate the local Green functions  $G_{ii\sigma}(\omega)$  with respect to each site with random potential  $\epsilon_i$ .

$$G_{ii\sigma}(\omega) = \frac{1}{\omega - \mu + \epsilon_i - \Sigma_\sigma(\omega) - \eta_\sigma(\omega)}. \quad (2.30)$$

- (iii) From  $G_{ii\sigma}(\omega)$ , calculate the local densities of states  $\rho_{i\sigma}(\omega)$ .

$$\rho_{i\sigma}(\omega) = -\frac{1}{\pi} \text{Im} G_{ii\sigma}(\omega). \quad (2.31)$$

- (iv) Perform an arithmetic average of  $\rho_{i\sigma}(\omega)$ .

$$\rho_\sigma^{\text{arith}}(\omega) = \int d\epsilon_i P(\epsilon_i) \rho_{i\sigma}(\omega), \quad (2.32)$$

where  $\rho_\sigma^{\text{arith}}(\omega)$  represents the disorder-averaged density of states and  $P(\epsilon_i)$  the probability distribution function for a random variable  $\epsilon_i$ .

- (v) Calculate the disorder-averaged Green function  $G_\sigma(\omega)$  as,

$$G_\sigma(\omega) = \int d\omega' \frac{\rho_\sigma^{\text{arith}}(\omega')}{\omega - \omega' - \Sigma_\sigma(\omega)}. \quad (2.33)$$

- (vi) Update  $\eta_\sigma(\omega)$  and calculate the cavity Green function  $\mathcal{G}_\sigma(\omega)$ .

$$\eta_\sigma(\omega) = \omega + \mu - \Sigma_\sigma(\omega) - G_\sigma^{-1}(\omega), \quad (2.34)$$

$$\mathcal{G}_\sigma(\omega) = \frac{1}{\omega + \mu - \eta_\sigma(\omega)}. \quad (2.35)$$

- (vii) Update the self-energy  $\Sigma_\sigma(\omega)$  by using an impurity solver.

The difference between the self consistent loop of a CPA+DMFT method and that of a standard DMFT is found in the steps (ii)-(vi). These steps are relevant to the framework of a CPA, and in these steps the effective hybridization function  $\eta_\sigma(\omega)$  is

calculated from the disorder-averaged Green function  $G_\sigma(\omega)$ . We supplement here a brief explanation of the calculations performed in these steps.

The hybridization function  $\eta_{i\sigma}(\omega)$  is defined from Eq.(2.18) as,

$$\eta_{i\sigma}(\omega) = t^2 \sum_{\langle x,y \rangle} G_{xy\sigma}^{(i)}(\omega), \quad (2.36)$$

where  $x$  and  $y$  are the site indices, and it is imposed that only the hopping to the nearest neighbor sites takes a nonzero value. Also, the site dependence of a hopping amplitude is omitted ( $t_{xi}=t_{iy}=t$ ). It is found from Eq.(2.36) that the hybridization function must originally depend on the site index. Here, the approximation, which becomes exact if a spatial dimension  $d$  is infinite in the same manner as the case of DMFT, is adopted. It is also assumed that the lattice coordination number  $z$  increases with increasing the spatial dimension, such as  $z \rightarrow \infty$  if  $d \rightarrow \infty$ . If  $z \rightarrow \infty$ , the sites related to all sorts of  $\epsilon_i$  should neighbor the focusing site. This fact suggests that we can substitute the Green function, which is used to determine the hybridization function and depends on sites, for the disorder-averaged Green function. By this substitution, only the one hybridization which is independent of sites should be calculated. Hence, the cavity Green function and the self-energy also do not depend on the lattice sites, and after having calculated the hybridization function, we can follow the framework of a standard DMFT and calculate the self-energy without taking an additional numerical cost.

The CPA+DMFT method becomes exact if  $d \rightarrow \infty$  and reduces to a CPA (DMFT) for the interaction  $U=0$  (for the random potential  $\epsilon_i=0$  at all sites). This method is notably suitable to analyze the binary-alloy systems[92, 94, 96, 97, 100], described by the model with the site-diagonal random potential which is characterized by the bimodal probability distribution function  $P_{\text{bi}}(\epsilon_i)$ ,

$$P_{\text{bi}}(\epsilon_i) = \gamma \delta\left(\epsilon_i + \frac{D}{2}\right) + (1 - \gamma) \delta\left(\epsilon_i - \frac{D}{2}\right), \quad (2.37)$$

where  $\gamma$  denotes the mix ratio of the random variables and  $D$  represents the strength of the random potential. This is because the CPA+DMFT method enables us to successfully capture the influence caused by the band-splitting effects which should be observed in binary-alloy systems. Also, in some previous studies[98, 99] the CPA+DMFT method has been used to analyze the model with  $\epsilon_i$  which is randomly selected from the uniform distribution function  $P_{\text{uni}}(\epsilon_i)$ ,

$$P_{\text{uni}}(\epsilon_i) = \frac{1}{D} \Theta\left(\frac{D}{2} - |\epsilon_i|\right). \quad (2.38)$$

In these previous studies, it is clarified how weak disorder competes with the interaction between particles and affects the properties of the systems near the Mott transition.

### 2.1.3 How to treat backscattering effects within a DMFT

It is noted in the previous subsection that the CPA+DMFT method is useful to analyze the interacting systems with spatially random potential because the influence of the spatial nonuniformity seems to be suitably captured in addition to correlation effects. However, the CPA+DMFT method does not deal with the backscattering effects which is caused by spatial nonuniformity and might affect the properties of strongly-disordered systems, and thus the Anderson localization is not described within the framework of the CPA+DMFT. To overcome this weakness and clarify the competition or the cooperation between the effects of strong disorder and correlation effects, the CPA+DMFT method is extended, and hence the statistical DMFT[82, 83] have been developed.

The arithmetically-averaged Green function is used to estimate the influence of spatial nonuniformity as Eq.(2.34). This is the reason why the CPA+DMFT cannot capture backscattering effects which causes Anderson localization. The local density of states (LDOS) includes the information whether these states are extended states or localized states in disordered systems. However, as first pointed out in 1958[40], the arithmetic average of the LDOS just gives the energy region where the states exist, and does not show whether the states contribute to the conductivity or not. The statement is easily understand by considering the probability distribution function of the LDOS at the Fermi energy ( $P(\rho_i(\omega=\epsilon_F))$ , where  $\epsilon_F$  is the Fermi energy.).  $P(\rho_i(\omega=\epsilon_F))$  in weakly disordered systems and strongly disordered systems are shown in Fig. 2.3. In disordered systems, the LDOS takes a different value with respect to each site due to the influence of the spatial nonuniformity, and hence the dispersion of  $P(\rho_i(\omega=\epsilon_F))$  becomes larger with increase of the disorder strength. The increase of the dispersion of  $P(\rho_i(\omega=\epsilon_F))$  is observed even in weakly disordered systems. However, the dispersion of  $P(\rho_i(\omega=\epsilon_F))$  is still small and the arithmetic average of the LDOS is almost the same as the mode value of the LDOS (see the left figure in Fig. 2.3). The mode value might represent the properties of the whole systems, and thus it can be concluded that the arithmetic average is useful to describe the properties of weakly disordered systems. On the other hand, the situation is completely changed in strongly disordered systems. Strong nonuniformity makes the states localized, and the LDOS at most sites becomes zero at the Fermi energy. However, there are also a few sites where the LDOS remains to take a nonzero value. Therefore,  $P(\rho_i(\omega=\epsilon_F))$  should have a peak near  $\rho_i(\omega=\epsilon_F)=0$  and the long tail which extends to the very large value of  $\rho_i(\omega=\epsilon_F)$  as shown in the right figure of Fig. 2.3. The arithmetic average is absolutely different from the mode value in this distribution function, and hence the arithmetic average of the LDOS in strongly disordered systems does not play a role

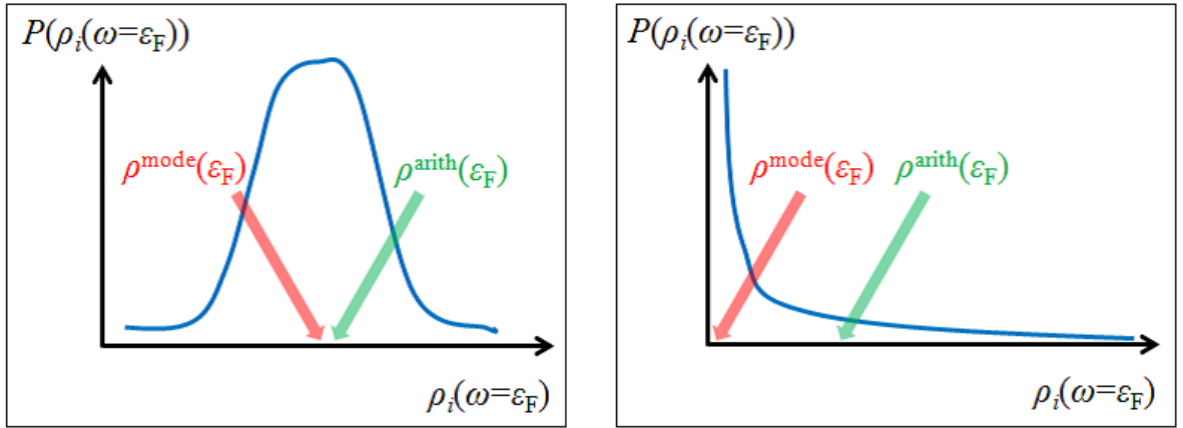


Fig. 2.3 Schematic pictures of the probability distribution functions of the LDOS at the Fermi energy. The left figure shows it in weakly disordered systems and the right figure it in strongly disordered systems.  $\rho^{\text{arith}}(\epsilon_F)$  and  $\rho^{\text{mode}}(\epsilon_F)$  in the figures represent the arithmetic average and the mode value of the LDOS, respectively.

of the order parameter which reflects the properties of the whole systems.

It can be found from the above discussion that we should discuss the properties of the systems with strong nonuniformity by using the probability distribution function or the mode value of the physical quantities. According to this idea, the ensemble of the hybridization function is calculated instead of the disorder-averaged hybridization within the framework of a statistical DMFT from Eq.(2.36). The way to calculate the ensemble of  $\eta_{i\sigma}(\omega)$  in the case of Bethe lattices (Fig. 2.4) is as follows. In the

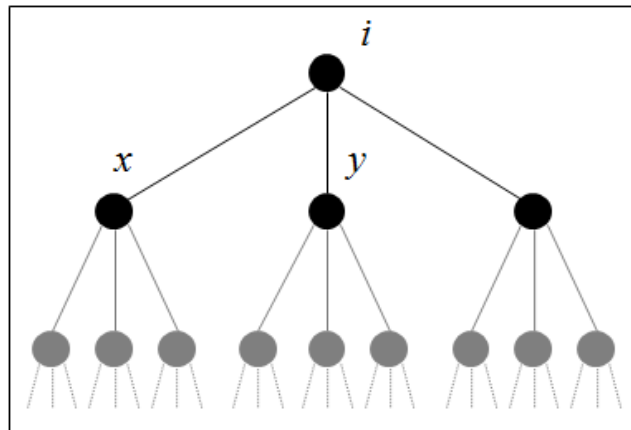


Fig. 2.4 Bethe lattice in the case that a lattice coordination number  $z$  is four and a connectivity  $K$  is three.

Bethe lattice,  $t^2 \sum_{\langle x,y \rangle} G_{xy\sigma}^{(i)}(\omega)$  in Eq.(2.36) can be reduced to the simple formula.

The branches on the Bethe lattice are characterized by the connectivity  $K$  and do not mutually cross even if the lattice becomes large. Hence, there are no loop structures in this lattice. From this argument, the relation  $G_{xy\sigma}^{(i)}(\omega) = G_{xx\sigma}^{(i)}(\omega)\delta_{xy}$  is given. Also, as seen from Fig. 2.4, the lattice structure which originates the site  $x$  does not change even when the site  $i$  is omitted, and thus  $G_{xx\sigma}^{(i)}(\omega) = G_{xx\sigma}(\omega)$  is obtained. Therefore, the formula about the hybridization function is simply expressed as,

$$\eta_{i\sigma}(\omega) = t^2 \sum_x^K G_{xx\sigma}(\omega), \quad (2.39)$$

where the sum  $x$  runs over the  $K$  nearest neighbors of the site  $i$ . Using Eq.(2.39), we can calculate the ensemble of the hybridization function. Here, it should be commented that the difference between  $z$  and  $K$  is neglected in the derivation of Eq.(2.39).  $z$  and  $K$  of the Bethe lattice are related by the equation  $z = K + 1$ , and thus the accuracy of this approximation becomes higher with an increase of  $K$ . Bethe lattices are here assumed to simplify the derivation, but the ensemble of  $\eta_{i\sigma}(\omega)$  in the case of arbitrary lattices, where there are some loop structures, is also calculated in the same manner by adopting the approximation that  $G_{xx\sigma}^{(i)}(\omega) = G_{xx\sigma}(\omega)$ .

We summarize the self-consistent loop of a statistical DMFT below (see also Fig. 2.5).

- (i) Select the appropriate ensembles of  $\Sigma_{i\sigma}(\omega)$  and  $\eta_{i\sigma}(\omega)$  as an initial state.
- (ii) Construct the ensemble of the local Green function  $G_{ii\sigma}(\omega)$  from the ensembles of  $\Sigma_{i\sigma}(\omega)$  and  $\eta_{i\sigma}(\omega)$  from

$$G_{ii\sigma}(\omega) = \frac{1}{\omega - \mu + \epsilon_i - \Sigma_{i\sigma}(\omega) - \eta_{i\sigma}(\omega)}. \quad (2.40)$$

- (iii) Randomly select the several local Green functions from the ensemble of  $G_{ii\sigma}(\omega)$ . From Eq.(2.39) and selected Green functions, calculate  $\eta_{i\sigma}(\omega)$  and construct the ensemble of that. (The number of  $G_{ii\sigma}(\omega)$  is selected here is equal to the number of  $K$ .)
- (iv) Update the self-energy  $\Sigma_{i\sigma}(\omega)$  at each site by using an impurity solver.

By comparing the self-consistent loop of the statistical DMFT with that of the CPA+DMFT, it is found that the disorder average of physical quantities is not taken within the framework of the statistical DMFT. Therefore, using this method, we can accurately construct the full probability distribution functions of physical quantities and successfully treat the effects caused by strong disorder such as backscattering effects which trigger Anderson localization.

It is a notable advantage of a statistical DMFT method to describe Anderson localization. The strongly-correlated systems with strong disorder have been investigated

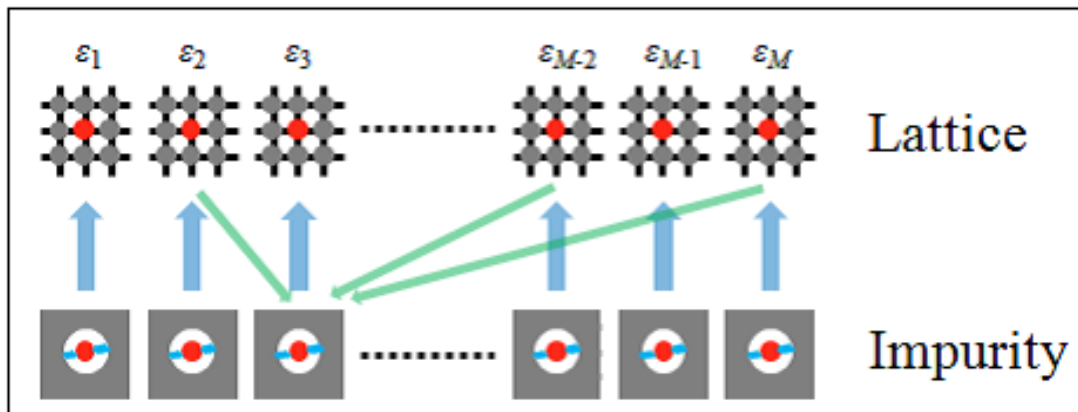


Fig. 2.5 The conceptual figure of the self-consistent loop of the statistical DMFT. From the local Green functions with  $\epsilon_i$  which the green arrowed lines originate at, the cavity Green function which the green arrowed lines gain is calculated. This figure shows the case that the connectivity  $K$  is three.

by using this method, and it has been clarified how the correlation effects and spatial nonuniformity compete with each other in the systems with binary disorder[101], speckle disorder[102], or uniform disorder[103].

To address the shortcomings of a statistical DMFT may be helpful to deeply understand this method. One of the weak points of this method is that the cost to perform numerical calculations is much larger than that of case where the CPA+DMFT is used. This is because the process, where the self-energy is calculated, takes the largest time in the self-consistent loop of a DMFT, and the self-energy has to be calculated at each site in the framework of the statistical DMFT. Naively thinking, the numerical cost of the statistical DMFT is  $M$  times as large as that of the CPA+DMFT (Here,  $M$  denotes the number of sites.). Owing to this numerical cost, it is difficult to use the method which is numerically reliable but needs to pay a large cost as an impurity solver.

At the end of this subsection, we would like to introduce the typical medium theory (TMT)[104] which is also an extension of the CPA+DMFT method and developed to successfully deal with the effects caused by strong disorder. As is the case in the statistical DMFT, the way to calculate the hybridization function from Eq.(2.34) in the case of the TMT is different from that in the case of a CPA+DMFT. Within the TMT, the hybridization function is calculated from the geometrical average of local Green functions calculated as

$$\rho_{\sigma}^{\text{geom}}(\omega) = \exp \left[ \int d\epsilon_i P(\epsilon_i) \ln \rho_{i\sigma}(\omega) \right], \quad (2.41)$$

$$G_{\sigma}^{\text{geom}}(\omega) = \int d\omega' \frac{\rho_{\sigma}^{\text{geom}}(\omega')}{\omega - \omega' - \Sigma_{\sigma}(\omega)}. \quad (2.42)$$

Here,  $\rho_{\sigma}^{\text{geom}}(\omega)$  ( $G_{\sigma}^{\text{geom}}(\omega)$ ) represents the geometrical average of the local density of states (the local Green functions). From Fig. 2.3, we can naively understand the reasons why a geometrical average instead of an arithmetic average is adopted and we can capture the effects of strong nonuniformity by using the TMT. As mentioned above, the arithmetic average is extremely different from the mode value in strongly-disordered systems, and thus the arithmetic average does not reflect the properties of such systems. On the other hand, the geometrical average seems almost same as the mode value even in strongly disordered systems. (For reference, we note here that the relation  $\rho_{\sigma}^{\text{geom}}(\omega) = \rho_{\sigma}^{\text{mode}}(\omega)$  exactly holds if the probability distribution is a log-normal distribution.) This fact means that the geometrical average plays a role of an order parameter in the disordered systems. For examples, the geometrical average of the local density of states vanishes at Anderson transition points in non-interacting systems with disorder[40, 82, 104] and also seems to be a good criterion for the Anderson localization in interacting systems[46, 47]. (We provide a more detailed description of  $\rho_{\sigma}^{\text{geom}}(\omega)$  in Sec. 3.2.)

The advantage of the TMT method is that we can deal with the effects of strong nonuniformity in addition to that of weak nonuniformity by this method, but have not to pay a more numerical cost. The numerical cost to use the TMT method is almost equal to that to use a CPA+DMFT method. Thanks to this advantage, we can relatively easily approach strongly-disordered and strongly-correlated systems, and hence there are many previous studies in which the TMT is used as a numerical method[46, 47, 105, 106, 107, 108, 109].

We would like to note here that the TMT is an efficient numerical method, but the effects due to strong nonuniformity on the properties of systems should be more accurately captured by a statistical DMFT method than by the TMT method. This is because the full probability distribution function of physical quantities is constructed within the statistical DMFT, whereas only the geometrical average, which is a mere approximation to a mode value, is obtained within the TMT. For reference, we comment on the probability distribution function in strongly disordered and correlated systems. It is reported in the previous study[103] that as correlation effects increases in such systems the probability distribution function deviates far from a log-normal distribution function, and thus the geometrical average becomes to be unsuitable. For this reason, we employ the statistical DMFT method to investigate strongly disordered and correlated systems in this study.

#### 2.1.4 Extension of statistical DMFT

In this study, we extend the statistical DMFT method to investigate attractively interacting systems with spatial nonuniformity described by the following Anderson-

Hubbard model Hamiltonian.

$$H = -t \sum_{\langle i,j \rangle, \sigma} (C_{i\sigma}^\dagger C_{j\sigma} + h.c.) - \sum_{i,\sigma} (\mu - \epsilon_i) n_{i\sigma} - U \sum_i n_{i\uparrow} n_{i\downarrow}. \quad (2.43)$$

It is well-known that the superfluid state is stabilized as the ground state at zero temperature in attractively interacting systems without disorder. Therefore, the Nambu formalism is used to take the superfluid order with singlet pairing into account. In this case, the cavity Green function matrix  $\hat{\mathcal{G}}_i(\omega)$  and the self-energy matrix  $\hat{\Sigma}_i(\omega)$  at site  $i$  are given as,

$$\hat{\mathcal{G}}_i(\omega) = \begin{pmatrix} \mathcal{G}_i(\omega) & \mathcal{F}_i(\omega) \\ \mathcal{F}_i^\dagger(-\omega) & -\mathcal{G}_i^\dagger(-\omega) \end{pmatrix}, \quad (2.44)$$

$$\hat{\Sigma}_i(\omega) = \begin{pmatrix} \Sigma_i(\omega) & S_i(\omega) \\ S_i^*(-\omega) & -\Sigma_i^*(-\omega) \end{pmatrix}, \quad (2.45)$$

where  $\mathcal{G}$  and  $\mathcal{F}$  ( $\Sigma$  and  $S$ ) denote the diagonal and off-diagonal part of the cavity Green function matrix (the self-energy matrix). The matrix elements of  $\hat{\mathcal{G}}$  are expressed as,

$$\mathcal{G}_i(\omega) = \frac{\beta_i}{\gamma_i \beta_i - \eta_i^{\text{off}}(\omega)(\eta_i^{\text{off}}(-\omega))^*}, \quad (2.46)$$

$$\mathcal{F}_i(\omega) = \frac{-\eta_i^{\text{off}}(\omega)}{\gamma_i \beta_i - \eta_i^{\text{off}}(\omega)(\eta_i^{\text{off}}(-\omega))^*}. \quad (2.47)$$

Here,  $\gamma_i$  and  $\beta_i$  are

$$\gamma_i = \omega + \mu - \epsilon_i - \eta_i(\omega) + i\delta, \quad (2.48)$$

$$\beta_i = \omega - \mu + \epsilon_i - (\eta_i(-\omega))^* + i\delta, \quad (2.49)$$

where  $\eta_i(\omega)$  and  $\eta_i^{\text{off}}(\omega)$  represent the diagonal matrix element and the off-diagonal matrix element of the hybridization function matrix  $\hat{\eta}_i(\omega)$  given as,

$$\hat{\eta}_i(\omega) = \begin{pmatrix} \eta_i(\omega) & -\eta_i^{\text{off}}(\omega) \\ -(\eta_i^{\text{off}}(-\omega))^* & -(\eta_i(-\omega))^* \end{pmatrix}. \quad (2.50)$$

In Eqs.(2.48) and (2.49), we explicitly express the broadening weight  $\delta$  which denotes the lifetime of quasiparticles.  $\delta$  ( $>0$ ) is here assumed to be infinitesimally small, but we take a small finite value for it in our numerical calculations. The matrix of the hybridization function  $\hat{\eta}_i(\omega)$  is related to the matrix of the local Green function  $\hat{G}_{ii}(\omega)$  by

$$\hat{\eta}_i(\omega) = \sum_{j=1}^K t^2 \hat{G}_{jj}(\omega) \quad (2.51)$$

in the case of Bethe lattices. The matrix of the local Green function is calculated from  $\hat{\mathcal{G}}_i(\omega)$  and  $\hat{\Sigma}_i(\omega)$  via the Dyson equation

$$\hat{G}_{ii}^{-1}(\omega) = \hat{\mathcal{G}}_i^{-1}(\omega) - \hat{\Sigma}_i(\omega). \quad (2.52)$$

The flow of the self-consistent loop of the extended statistical DMFT is almost same as the flow of a usual statistical DMFT which has been described in the previous subsection.

### 2.1.5 Impurity solver : modified iterative perturbation theory

The framework of a DMFT and the extensions of it have been already described. In this subsection, we discuss the impurity solver which is used to calculate the self-energy of a single impurity model. There are many numerical methods which are useful as an impurity solver of the DMFT. Non-crossing approximation (NCA)[110], exact diagonalization approach (ED)[111], quantum Monte Carlo method (QMC)[112], numerical renormalization group (NRG)[113], continuous-time quantum Monte Carlo method (ct-QMC)[114], and iterative perturbation theory (IPT)[115, 116] are given as the representative examples. In these methods, it is known that the NRG and the ct-QMC enable us to successfully treat the local correlation effects in particular although the numerical cost to use these two methods is huge. Thanks to this high reliability, these two methods have been used as the impurity solver of a CPA+DMFT[100], or a TMT method[46, 47, 108]. By contrast, owing to the huge numerical cost, it is more difficult to incorporate these two methods in the framework of a statistical DMFT. Hence, an IPT has been used in the several previous studies[101, 102, 103]. The IPT is a simpler approximation, but gives qualitatively reliable results. It is also one of the advantages of the IPT that we do not need to pay a huge numerical cost. Considering the total numerical cost and the reliability of results, we choose the IPT as an impurity solver of a statistical DMFT.

Before presenting the detail of this method, it should be commented that the IPT should not be applied to the analyses of the systems without particle-hole symmetry such as the systems with spatial nonuniformity. This is because the IPT is formulated so as to give the self-energy which is correct in an atomic limit, a high frequency limit, and a low frequency limit when particle-hole symmetry is preserved. In particular, if particle-hole symmetry is broken, the IPT should not obtain the correct self-energy in the atomic limit. To overcome this shortcoming, a modified-IPT (mIPT) has been developed[87, 88]. This mIPT is an expansion of the usual IPT and gives the correct self-energy in the three limits mentioned above even in the systems without particle-hole symmetry. In this study, the mIPT is used to investigate the spatially disordered and correlated systems. The detail of mIPT is as follows.

In the IPT, the self-energy is calculated using perturbation theory up to the second order in interaction  $U$ . The interpolating self-energy based on IPT is defined in mIPT as,

$$\hat{\Sigma}_i(\omega) = \hat{\Sigma}_i^{\text{HFB}} + \hat{X}_i \hat{\Sigma}_i^{(2)}(\omega). \quad (2.53)$$

Here,  $\hat{\Sigma}_i^{(2)}(\omega)$  is the second-order self-energy and  $\hat{\Sigma}_i^{\text{HFB}}$  the Hartree-Fock-Bogoliubov (HFB) self-energy matrix

$$\begin{aligned} \hat{\Sigma}_i^{\text{HFB}} &= -\frac{1}{2}U n_i \hat{\tau}_z - U \Phi_i \hat{\tau}_x \\ &= U \begin{pmatrix} -\frac{1}{2}n_i & -\Phi_i \\ -\Phi_i & \frac{1}{2}n_i \end{pmatrix}, \end{aligned} \quad (2.54)$$

where  $\hat{\tau}_x$  and  $\hat{\tau}_z$  are Pauli matrices in Nambu space. The local filling factor  $n_i$  and the local superfluid order parameter  $\Phi_i$  are given as,

$$n_i = -\frac{2}{\pi} \int_{-\infty}^0 d\omega \text{Im} G_{ii}(\omega), \quad (2.55)$$

$$\Phi_i = -\frac{1}{\pi} \int_{-\infty}^0 d\omega \text{Im} F_{ii}(\omega), \quad (2.56)$$

where  $G_{ii}(\omega)$  ( $F_{ii}(\omega)$ ) is the diagonal (off-diagonal) element of the local Green function matrix.  $\hat{X}_i$  in Eq.(2.53) is the matrix which is introduced to give the correct self-energy in the three limits (atomic limit, high frequency limit, and low frequency limit), and is expressed as[65],

$$\hat{X}_i = \left[ \frac{n_i}{2} \left( 1 - \frac{n_i}{2} \right) - \Phi_i^2 \right] \times \left[ \frac{n'_i}{2} \left( 1 - \frac{n'_i}{2} \right) - \Phi_i'^2 \right]^{-1} \hat{\tau}_0, \quad (2.57)$$

where  $\hat{\tau}_0$  is an identity matrix in Nambu space.  $n'_i$  and  $\Phi'_i$  are a fictive local particle density and a fictive local superfluid order parameter which are introduced to consider the influence caused by density fluctuation. These physical quantities are obtained from the diagonal part  $\mathcal{G}'_i(\omega)$  and the off diagonal part  $\mathcal{F}'_i(\omega)$  of a fictive cavity Green function matrix  $\hat{\mathcal{G}}'_i(\omega)$  as,

$$n'_i = -\frac{2}{\pi} \int_{-\infty}^0 d\omega \text{Im} \mathcal{G}'_i(\omega), \quad (2.58)$$

$$\Phi'_i = -\frac{1}{\pi} \int_{-\infty}^0 d\omega \text{Im} \mathcal{F}'_i(\omega). \quad (2.59)$$

The fictive cavity Green function matrix is related to the cavity Green function matrix by

$$\begin{pmatrix} \mathcal{G}'_i(\omega) & \mathcal{F}'_i(\omega) \\ \mathcal{F}'_i^\dagger(-\omega) & -\mathcal{G}'_i^\dagger(-\omega) \end{pmatrix}^{-1} = \begin{pmatrix} \mathcal{G}_i(\omega) & \mathcal{F}_i(\omega) \\ \mathcal{F}_i^\dagger(-\omega) & -\mathcal{G}_i^\dagger(-\omega) \end{pmatrix}^{-1} - \hat{\Sigma}_i^{\text{HFB}}. \quad (2.60)$$

At the end of this subsection, the detail formula of the second-order self-energy matrix is described. The influence by density fluctuation should be considered in calculating the second-order self-energy matrix  $\hat{\Sigma}_i^{(2)}(\omega)$ . Hence,  $\hat{\Sigma}_i^{(2)}(\omega)$  is calculated from a fictive cavity Green function as,

$$\begin{aligned} \Sigma_i^{(2)}(\omega) = -iU^2 \int_0^\infty dt e^{i\omega t - \delta t} \times \{ & A_i(t)A_i(t)B_i(-t) + B_i(t)B_i(t)A_i(-t) \\ & + A_i(t)C_i(t)D_i(-t) + B_i(t)D_i(t)C_i(-t) \}, \end{aligned} \quad (2.61)$$

$$\begin{aligned} S_i^{(2)}(\omega) = -iU^2 \int_0^\infty dt e^{i\omega t - \delta t} \times \{ & C_i(t)D_i(-t)D_i(-t) + D_i(t)C_i(-t)C_i(-t) \\ & + A_i(t)D_i(-t)B_i(-t) + B_i(t)C_i(-t)A_i(-t) \}, \end{aligned} \quad (2.62)$$

where  $\Sigma_i^{(2)}(\omega)$  and  $S_i^{(2)}(\omega)$  are the diagonal and off-diagonal parts of  $\hat{\Sigma}_i^{(2)}(\omega)$ .  $A_i(t)$ ,  $B_i(t)$ ,  $C_i(t)$ , and  $D_i(t)$  are expressed as,

$$A_i(t) = -\frac{1}{\pi} \int_{-\infty}^\infty d\omega e^{-i\omega t} f(\omega) \text{Im}\mathcal{G}'_i(\omega), \quad (2.63)$$

$$B_i(t) = -\frac{1}{\pi} \int_{-\infty}^\infty d\omega e^{-i\omega t} f(-\omega) \text{Im}\mathcal{G}'_i(\omega), \quad (2.64)$$

$$C_i(t) = -\frac{1}{\pi} \int_{-\infty}^\infty d\omega e^{-i\omega t} f(\omega) \text{Im}\mathcal{F}'_i(\omega), \quad (2.65)$$

$$D_i(t) = -\frac{1}{\pi} \int_{-\infty}^\infty d\omega e^{-i\omega t} f(-\omega) \text{Im}\mathcal{F}'_i(\omega), \quad (2.66)$$

where the Fermi distribution function is represented by  $f(\omega)$ . This completes our formulation for treating a disordered attractive Hubbard model in terms of statistical DMFT combined with mIPT.

## 2.2 Bogoliubov-de Gennes method

A Bogoliubov-de Gennes (BdG) method[57] may be the most well-known one in the analytical approaches which has been developed to investigate the interacting systems with spatial nonuniformity. By using the BdG method, the influence by spatial nonuniformity is fully captured whereas the effects of an interaction is treated only at the static mean-field level. The BdG method is extended to investigate the multicomponent Fermi systems with disorder and employed in this study. After the explanation of a usual BdG method is presented, we describe the detail of the extended BdG equations.

### 2.2.1 Two-component Fermi systems with disorder

Two-component Fermi systems with disorder are often usual electron systems with impurities in solids and are successfully described by the Anderson-Hubbard model defined in Eq.(2.43). By introducing the expectation value of a local  $s$ -wave singlet pairing amplitude  $\Phi_i = \langle C_{i\downarrow} C_{i\uparrow} \rangle$  and a local particle density  $n_{i\sigma} = \langle C_{i\sigma}^\dagger C_{i\sigma} \rangle$ , the interaction term of the Anderson-Hubbard Hamiltonian  $H_{\text{int}}$  is decomposed as,

$$\begin{aligned} H_{\text{int}} &= -U \sum_i C_{i\uparrow}^\dagger C_{i\uparrow} C_{i\downarrow}^\dagger C_{i\downarrow} \\ &\rightarrow -U \sum_{i,\sigma} \langle n_{i\sigma} \rangle C_{i\sigma}^\dagger C_{i\sigma} - U \sum_i (\Phi_i C_{i\uparrow}^\dagger C_{i\downarrow}^\dagger + \Phi_i^* C_{i\downarrow} C_{i\uparrow}) + U \sum_i (\langle n_{i\uparrow} \rangle \langle n_{i\downarrow} \rangle + |\Phi_i|^2). \end{aligned} \quad (2.67)$$

By substituting Eq.(2.67) with Eq.(2.43), the mean-field Hamiltonian is given as,

$$\begin{aligned} H_{\text{mf}} &= -t \sum_{\langle i,j \rangle, \sigma} (C_{i\sigma}^\dagger C_{j\sigma} + h.c.) - \sum_{i,\sigma} \tilde{\mu}_{i\sigma} C_{i\sigma}^\dagger C_{i\sigma} \\ &\quad - U \sum_i (\Phi_i C_{i\uparrow}^\dagger C_{i\downarrow}^\dagger + \Phi_i^* C_{i\downarrow} C_{i\uparrow}), \end{aligned} \quad (2.68)$$

where  $\tilde{\mu}_{i\sigma} = \mu - \epsilon_i + U \langle n_{i\sigma} \rangle$  and the term  $U \sum_i (\langle n_{i\uparrow} \rangle \langle n_{i\downarrow} \rangle + |\Phi_i|^2)$  is omitted because this term only contributes the total energy of whole systems and is unconcerned in the formalism of the BdG equations. Here, it is assumed that a spin symmetry is conserved. Thus,  $\langle n_{i\uparrow} \rangle = \langle n_{i\downarrow} \rangle$ , and the spin dependence of  $\tilde{\mu}_{i\sigma}$  is neglected ( $\tilde{\mu}_{i\sigma} \rightarrow \tilde{\mu}_i$ ).  $H_{\text{mf}}$  is transferred to the matrix representation as follows.

$$H_{\text{mf}} = \begin{pmatrix} \hat{C}_{i\uparrow}^\dagger & \hat{C}_{i\downarrow} \end{pmatrix} \hat{H}_{\text{BdG}} \begin{pmatrix} \hat{C}_{i\uparrow} \\ \hat{C}_{i\downarrow}^\dagger \end{pmatrix} \quad (2.69)$$

$$= \begin{pmatrix} \hat{C}_{i\uparrow}^\dagger & \hat{C}_{i\downarrow} \end{pmatrix} \begin{pmatrix} \hat{K} & \hat{\Phi} \\ \hat{\Phi}^* & -\hat{K} \end{pmatrix} \begin{pmatrix} \hat{C}_{i\uparrow} \\ \hat{C}_{i\downarrow}^\dagger \end{pmatrix}, \quad (2.70)$$

where the basis  $(\hat{C}_{i\uparrow}^\dagger \hat{C}_{i\downarrow}) = (C_{1\uparrow}^\dagger C_{2\uparrow}^\dagger \cdots C_{M\uparrow}^\dagger C_{1\downarrow} C_{2\downarrow} \cdots C_{M\downarrow})$  ( $M$  represents the number of sites.) is adopted and  $\hat{K}$  ( $\hat{\Phi}$ ) is the  $M \times M$  real symmetric matrix (the  $M \times M$  diagonal matrix) which composes  $t$  and  $\tilde{\mu}_i$  ( $\Phi_i$ ).  $\hat{H}_{\text{BdG}}$  is the Hermite matrix, and hence can be diagonalized by introducing some unitary matrices  $\hat{P}$ .

$$H_{\text{mf}} = \begin{pmatrix} \hat{C}_{i\uparrow}^\dagger & \hat{C}_{i\downarrow} \end{pmatrix} \hat{P} \hat{P}^{-1} \begin{pmatrix} \hat{K} & \hat{\Phi} \\ \hat{\Phi}^* & -\hat{K} \end{pmatrix} \hat{P} \hat{P}^{-1} \begin{pmatrix} \hat{C}_{i\uparrow} \\ \hat{C}_{i\downarrow}^\dagger \end{pmatrix} \quad (2.71)$$

$$= \begin{pmatrix} \hat{\gamma}_{i\uparrow}^\dagger & \hat{\gamma}_{i\downarrow} \end{pmatrix} \hat{E} \begin{pmatrix} \hat{\gamma}_{i\uparrow} \\ \hat{\gamma}_{i\downarrow}^\dagger \end{pmatrix}, \quad (2.72)$$

where  $\hat{E}(=\hat{P}^{-1}\hat{H}_{\text{BdG}}\hat{P})$  is the diagonal matrix and its diagonal elements correspond to eigenvalues  $E_n \geq 0$ .  $(\hat{\gamma}_{i\uparrow}^\dagger \hat{\gamma}_{i\downarrow})=(\hat{C}_{i\uparrow}^\dagger \hat{C}_{i\downarrow})\hat{P}$  is the transformed basis which satisfies the commutation relations of fermions, and  $(\hat{\gamma}_{i\uparrow}^\dagger \hat{\gamma}_{i\downarrow})=(\gamma_{1\uparrow}^\dagger \gamma_{2\uparrow}^\dagger \cdots \gamma_{M\uparrow}^\dagger \gamma_{1\downarrow} \gamma_{2\downarrow} \cdots \gamma_{M\downarrow})$ . It is assumed here that  $\hat{P}$  is expressed as

$$\hat{P} = \begin{pmatrix} \hat{u} & -\hat{v}^* \\ \hat{v} & \hat{u}^* \end{pmatrix}, \quad (2.73)$$

where  $\{\hat{u}\}_{ij}=u_j(r_i)$  and  $\{\hat{v}\}_{ij}=v_j(r_i)$  ( $i, j=1 \cdots M$ ), and satisfy  $\sum_n \{|u_n(r_i)|^2 + |v_n(r_i)|^2\}=1$  for each  $r_i$ . By using  $u_j(r_i)$ ,  $v_j(r_i)$ , and  $\gamma_{i\sigma}$ , the inverse transforms for  $C_{i\sigma}$  and  $C_{i\sigma}^\dagger$  are given as,

$$C_{i\uparrow} = \sum_n \{u_n(r_i)\gamma_{n\uparrow} - v_n^*(r_i)\gamma_{n\downarrow}^\dagger\}, \quad (2.74)$$

$$C_{i\downarrow} = \sum_n \{u_n(r_i)\gamma_{n\downarrow} + v_n^*(r_i)\gamma_{n\downarrow}^\dagger\}. \quad (2.75)$$

Also, from these transformations, the following self-consistent equations of  $\langle n_i \rangle (= \sum_\sigma \langle n_{i\sigma} \rangle)$  and  $\Phi_i$  in the case of the temperature  $T=0$  are obtained.

$$\begin{aligned} \langle n_i \rangle &= \sum_\sigma \langle n_{i\sigma} \rangle \\ &= \langle C_{i\uparrow}^\dagger C_{i\uparrow} + C_{i\downarrow}^\dagger C_{i\downarrow} \rangle \\ &= 2 \sum_n |v_n(r_i)|^2, \end{aligned} \quad (2.76)$$

$$\begin{aligned} \Phi_i &= \langle C_{i\downarrow} C_{i\uparrow} \rangle \\ &= - \sum_n u_n(r_i) v_n^*(r_i). \end{aligned} \quad (2.77)$$

In the case that the systems with spatial nonuniformity are analyzed, the calculations should be performed on the finite-size lattice. The lattice size may be determined by the numerical cost to diagonalize  $\hat{H}_{\text{BdG}}$ . However, it is found from the above formulation of the BdG method that any approximations or limitations are not imposed to estimate the effects of  $\epsilon_i$  in the Anderson-Hubbard model. Hence, the BdG method can successfully describe the physical phenomena caused by the spatial nonuniformity.

## 2.2.2 Multicomponent Fermi systems with disorder

The BdG method can be employed to investigate the multicomponent systems with spatial nonuniformity described by the following Hamiltonian in the almost same

manner as the case of two-component systems.

$$H = -t \sum_{i,j,\sigma} (C_{i\sigma}^\dagger C_{j\sigma} + h.c.) - \sum_{i,\sigma} (\mu - \epsilon_i) n_{i\sigma} + \frac{1}{2} \sum_{i,\sigma,\sigma'} U_{\sigma\sigma'} n_{i\sigma} n_{i\sigma'}. \quad (2.78)$$

In this study, the  $SU(N)$ -symmetric systems ( $N$  represents the number of components.) are investigated. The  $SU(N)$  systems are the multicomponent systems where all parameters included in the Hamiltonian are independent of the spin. Thus, it is here explained how we apply the BdG method to  $SU(N)$  systems ( $U_{\sigma\sigma'} \rightarrow U$ ). Note that the notations  $\sigma=a, b, c, \dots$  and  $i=1, 2, 3, \dots$  are used hereafter.

The mean-fields of a local  $s$ -wave singlet pairing amplitude  $\Phi_i^{\sigma\sigma'} = \langle C_{i\sigma} C_{i\sigma'} \rangle$  and a local particle density  $n_{i\sigma} = \langle C_{i\sigma}^\dagger C_{i\sigma} \rangle$  are introduced, and the Hamiltonian in Eq.(2.78) is transformed into the mean-field Hamiltonian  $H_{\text{mf}}(N)$ ,

$$H_{\text{mf}}(N) = -t \sum_{\langle i,j \rangle, \sigma} (C_{i\sigma}^\dagger C_{j\sigma} + h.c.) - \sum_{i,\sigma} \left( \mu + \frac{N-1}{N} U n_i - \epsilon_i \right) C_{i\sigma}^\dagger C_{i\sigma} - \frac{U}{2} \sum_{i,\sigma \neq \sigma'} \left( \Phi_i^{\sigma\sigma'} C_{i\sigma'}^\dagger C_{i\sigma}^\dagger + \{ \Phi_i^{\sigma\sigma'} \}^* C_{i\sigma} C_{i\sigma'} \right), \quad (2.79)$$

where it is assumed that the local particle density does not depend on  $\sigma$ , and thus the total local particle density  $n_i = \sum_{\sigma} n_{i\sigma}$  is used instead of the local particle density. In the  $N=2$  case, we can give the matrix representation of the mean-field Hamiltonian in the Nambu basis. However, the basis  $(\hat{C}_{i\sigma}^\dagger \hat{C}_{i\sigma}) = (\hat{C}_{ia}^\dagger \hat{C}_{ib}^\dagger \dots \hat{C}_{iN}^\dagger \hat{C}_{ia} \hat{C}_{ib} \dots \hat{C}_{iN})$  ( $\hat{C}_{i\sigma} = (C_{1\sigma}, C_{2\sigma}, \dots, C_{M\sigma})$ ) must be chosen to transfer the mean-field Hamiltonian into the matrix representation in  $N>2$  because the three kinds of a singlet pairing amplitude are included in the mean-field Hamiltonian. Hence, the mean-field Hamiltonian is expressed by  $(2NM) \times (2NM)$  matrix as follows.

$$H_{\text{mf}}(N) = \begin{pmatrix} \hat{C}_{i\sigma}^\dagger & \hat{C}_{i\sigma} \end{pmatrix} \hat{H}_{\text{BdG}}(N) \begin{pmatrix} \hat{C}_{i\sigma} \\ \hat{C}_{i\sigma}^\dagger \end{pmatrix} \quad (2.80)$$

$$= \begin{pmatrix} \hat{C}_{i\sigma}^\dagger & \hat{C}_{i\sigma} \end{pmatrix} \begin{pmatrix} \hat{K}(N) & \hat{\Phi}(N) \\ \hat{\Phi}^*(N) & -\hat{K}(N) \end{pmatrix} \begin{pmatrix} \hat{C}_{i\sigma} \\ \hat{C}_{i\sigma}^\dagger \end{pmatrix}, \quad (2.81)$$

where  $\hat{K}(N)$  are the  $(NM) \times (NM)$  matrix composing of  $-t/2$  and  $-(\mu + \frac{N-1}{N} U n_i - \epsilon_i)/2$ , and  $\hat{\Phi}(N)$  that composing of  $U \Phi_i^{\sigma\sigma'}/2$ . Using the components of the normalized eigenvector  $u_n(r_i)$  and  $v_n(r_i)$ , we can diagonalize  $\hat{H}_{\text{BdG}}(N)$  via the transformation

$$\begin{aligned} \hat{c}_{ia} &= \sum_n \{ u_n(r_i) \hat{\gamma}_n + v_n^*(r_i) \hat{\gamma}_n^\dagger \}, \\ \hat{c}_{ib} &= \sum_n \{ u_n(r_{i+M}) \hat{\gamma}_n + v_n^*(r_{i+M}) \hat{\gamma}_n^\dagger \}, \\ &\vdots \end{aligned} \quad (2.82)$$

It is noticed that this transformation is slightly different from that of the  $N=2$  case. The self-consistent equations of the mean-fields are given by the above transformation in the same manner as  $N=2$ . We would like to comment here that the self-consistent equations can be derived in the similar manner even in the systems without  $SU(N)$  symmetry.

There is an important point to be noticed when we investigate the superfluid states in  $SU(N>2)$  Fermi systems by using the BdG method. This point is that the  $SU(N)$  symmetry is spontaneously broken when the superfluid order with even-parity pairs is realized even if the systems have  $SU(N>2)$  symmetry, and reduced to the  $SU(N/2)$  symmetry (the  $SU((N+1)/2)$  symmetry) if  $N$  is even (odd). This fact was particularly suggested in previous studies[69, 70]. Also, the authors showed that a constraint ( $\sum |\Phi^{\sigma\sigma'}|^2 = |\Phi_0|^2$ , where  $\Phi^{\sigma\sigma'}$  represents the order parameter of the singlet pairing of particles with the spin  $\sigma$  and  $\sigma'$ , and  $\Phi_0$  is a constant superfluid order parameter.) is imposed on the superfluid order parameters, and all the gap functions with this condition are energetically degenerate.

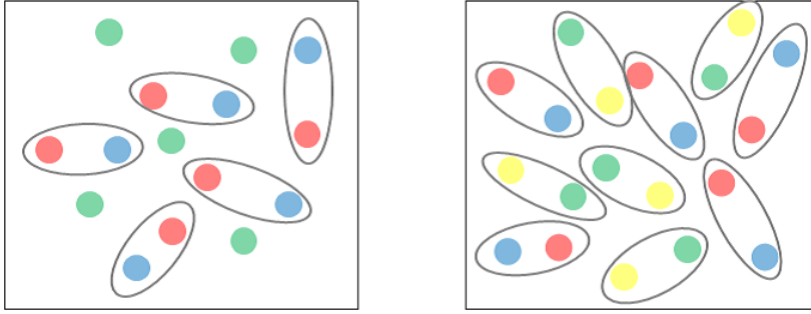


Fig. 2.6 Superfluid states in  $SU(3)$  (left panel) and  $SU(4)$  (right panel) systems. The difference of color represents that of the spin. (Left panel) Red and blue particles denote the paired particles and the green particles the unpaired particles. (Right panel) All particles are paired although red (green) particles are only paired with blue (yellow) particles and there are not the other pairs, such as the pair of red and green particles.

Taking the  $SU(3)$  case for instance, we concretely explain the results mentioned above. In the  $SU(3)$  systems, the three pairs, namely  $\Phi^{ba}$ ,  $\Phi^{cb}$ , and  $\Phi^{ac}$ , might be considered, and they are equivalent under  $SU(3)$  symmetry. When a singlet superfluid order is realized and the  $SU(3)$  symmetry is broken, these three pairs are not equivalent any more. Therefore, for examples, these three order parameters ( $\Phi^{ba}$ ,  $\Phi^{cb}$ ,  $\Phi^{ac}$ ) might be given by  $(\Phi_1, \Phi_2, \Phi_2)$  ( $\Phi_1$  and  $\Phi_2$  are constant order parameters.). Any of  $(\Phi_1, \Phi_2, \Phi_2)$  can be mapped into  $(\Phi_0, 0, 0)$  by a global gauge transformation. This pair of the order parameters  $(\Phi_0, 0, 0)$  means that the particles with  $a$  and those with  $b$  are only paired and contribute to the superfluid order whereas the particles with

spin  $c$  are unpaired and in the normal state (Fig. 2.6). From the discussion mentioned here, we find that the case of  $(\Phi_0, 0, 0)$  seems to be specific but equivalent to all the cases which are possible under the constraint  $\sum |\Phi^{\sigma\sigma'}|^2 = |\Phi_0|^2$ . Thus, we can choose the simplest state  $(\Phi_0, 0, 0)$  as an initial state of the self-consistent loop of the BdG method to investigate the superfluid states in SU(3) systems without additional approximations. For SU(4), a further limitation, such as  $|\Phi^{ba}|=|\Phi^{dc}|$ ,  $|\Phi^{cb}|=|\Phi^{da}|$ , and  $|\Phi^{ca}|=|\Phi^{db}|$ , is imposed on six superfluid order parameters  $(\Phi^{ba}, \Phi^{cb}, \Phi^{dc}, \Phi^{ad}, \Phi^{ca}, \Phi^{db})$ . The pair of  $(\Phi^{ba}, \Phi^{cb}, \Phi^{dc}, \Phi^{ad}, \Phi^{ca}, \Phi^{db})$  cannot be mapped into the  $(\Phi_0, 0, 0, 0, 0, 0)$  and thus all the particles are paired and contribute to the superfluid order (Fig. 2.6). The simplest case in the SU(4) systems is  $(\Phi_0, 0, \Phi_0, 0, 0, 0)$  and this case is chosen as an initial state in this study.

## Chapter 3

# Two-component systems with spatial nonuniformity

We present the results of two-component attractively interacting Fermi systems with spatial nonuniformity. These systems are well-described by the attractive Anderson-Hubbard Hamiltonian written in Eq.(2.43) and thus this Hamiltonian is analyzed by using the statistical DMFT method combined with mIPT in this chapter. We consider two typical probability distribution functions, such as a uniform distribution function  $P_{\text{uni}}(\epsilon_i)$  in Eq. (2.38) and a bimodal distribution function  $P_{\text{bi}}(\epsilon_i)$  in Eq.(2.37), as the probability distribution function which characterizes the random potential  $\epsilon_i$  in the Hamiltonian. The Hamiltonian with each probability distribution function is investigated. Comparing the case of  $P_{\text{bi}}(\epsilon_i)$  with that of  $P_{\text{uni}}(\epsilon_i)$ , we clarify the universal effects which are caused by spatial inhomogeneity and do not depend on the nature of the probability distribution functions, and the specific properties which depends on the probability distribution function.

In this chapter, after the detail of a numerical setup is described, the results in the case of  $P_{\text{uni}}(\epsilon_i)$  are explained and the elucidation of results in the systems with  $P_{\text{bi}}(\epsilon_i)$  follows. The comparison between the results of each probability distribution function is also discussed.

### 3.1 Numerical setup

Here, we would like to concretely describe the setup of the practical numerical calculations. The attractive Anderson-Hubbard Hamiltonian  $H_{\text{AH}}$

$$H_{\text{AH}} = -t \sum_{\langle i,j \rangle, \sigma} (C_{i\sigma}^\dagger C_{j\sigma} + h.c.) - \sum_{i, \sigma} (\mu - \epsilon_i) n_{i\sigma} - U \sum_i n_{i\uparrow} n_{i\downarrow} \quad (3.1)$$

is rewritten here. To analyze this Hamiltonian, we employ the statistical DMFT method. Calculations are performed at zero temperature on the Bethe lattice with

the connectivity  $K$  which is the input parameter used to determine the ensemble of the hybridization functions. This lattice has the semi-elliptical density of states characterized by a half-band width  $W$  if an interaction  $U=0$  and  $\epsilon_i=0$  at each site. We set the energy unit as  $W=1$  in noninteracting and nondisordered cases. The number of the ensembles of physical quantities is 1000. It is confirmed that this number is large enough to omit a dependence on the distribution of  $\epsilon_i$ . The free energy might have the many local minimum points in the systems with spatial nonuniformity, and thus it is not ensured that the results obtained by the mean-field approach always give true solutions in such systems. Therefore, we check that some different initial states lead to the same solution.

## 3.2 Uniformly disordered systems

In this section, we show the results in the disordered systems where  $\epsilon_i$  is characterized by a uniform probability distribution function  $P_{\text{uni}}(\epsilon_i)$ .  $P_{\text{uni}}(\epsilon_i)$

$$P_{\text{uni}}(\epsilon_i) = \frac{1}{D} \Theta\left(\frac{D}{2} - |\epsilon_i|\right) \quad (3.2)$$

is rewritten here and pictured in Fig. 3.1. In the study of the uniformly disordered systems, we set  $K=3$  and  $n=1$  ( $n$  denotes the particle density of the whole system and  $n=1$  at half-filling.).

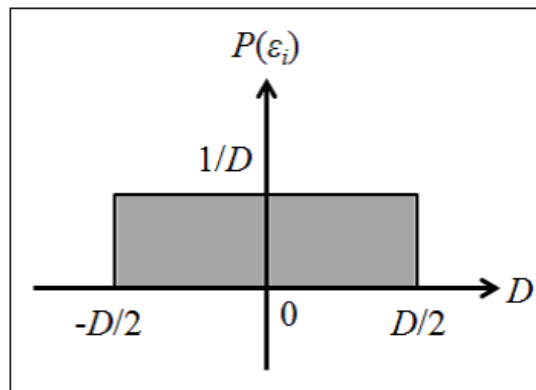


Fig. 3.1 Uniform probability distribution function of  $\epsilon_i$ .

### Anderson localization

As discussed in Sec. 1.2, in uniformly disordered systems without interaction, it is known that spatial inhomogeneity makes the particles localized and hence triggers a metal-Anderson localized state transition, the so-called Anderson transition. The

typical  $\rho_{i\sigma}(\omega)$  in the Anderson localized states is presented in the right panel of Fig. 3.2. It is naively understood from this panel that as mentioned in Sec. 2.1, the

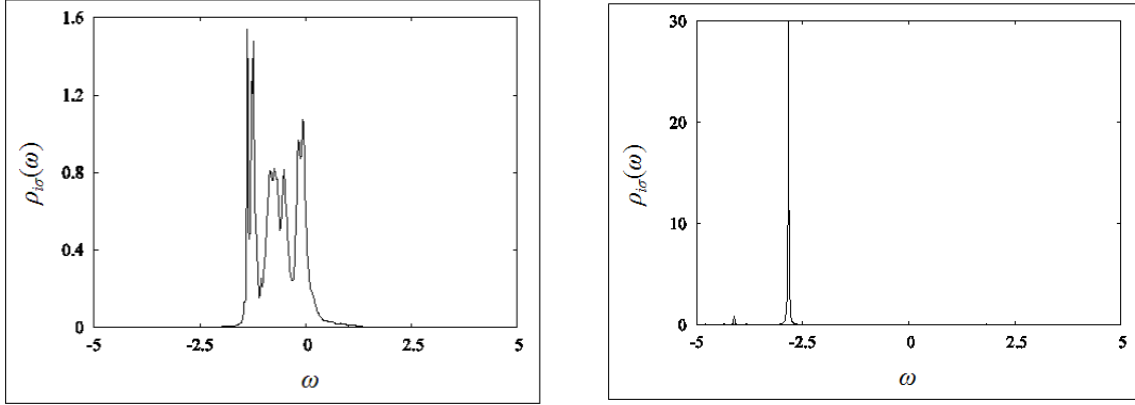


Fig. 3.2 Local density of states  $\rho_{i\sigma}(\omega)$  at some site in noninteracting systems. The left figure shows the case of  $D=2$  where systems are in metallic states, and the right figure the case of  $D=10$  where systems are in Anderson localized states.

geometrical average of the local density of states  $\rho_{\sigma}^{\text{geom}}(\omega)$  provides a good criterion for the Anderson transition because  $\rho_{\sigma}^{\text{geom}}(\omega)$  vanishes in the Anderson localized states. For reference, we show the arithmetic average and the geometrical average of the local density of states for  $D=0, 3, 6,$  and  $9$  in Fig. 3.3. In the previous

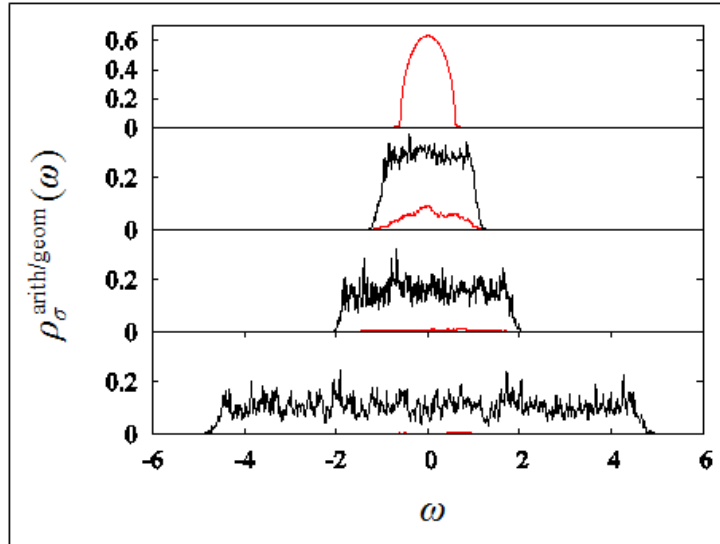


Fig. 3.3 Arithmetic average  $\rho_{\sigma}^{\text{arith}}(\omega)$  (black lines) and geometrical average  $\rho_{\sigma}^{\text{geom}}(\omega)$  (red lines) of the local density of states in the cases of the disorder strength  $D=0, 3, 6,$  and  $9$  from top to bottom.  $U=0$  is chosen.

study[103], it is reported that the Anderson transition occurs at the strength of uniform disorder  $D=8$  within the statistical DMFT in  $U=0$  and  $K=3$ , and also the

geometrical average given in our study (Fig. 3.3) almost vanishes in the Anderson localized states whereas the geometrical average takes a finite value at the energy region including the Fermi energy below  $D=6$ . It might be confirmed also from the above discussion that  $\rho_{\sigma}^{\text{geom}}(\omega)$  is suitable as the order parameter of Anderson localization.

Numerically determining the Anderson transition points by  $\rho_{\sigma}^{\text{geom}}(\omega)$ , we must pay attention to the dependence of  $\rho_{\sigma}^{\text{geom}}(\omega)$  on a broadening weight  $\delta$ .  $\delta$  transforms the delta-function density of states into the Lorentzian density of states which we can numerically deal with. For this purpose,  $\delta$  must be introduced in numerical calculations. It is easily understood from this property of the broadening weight that  $\delta$  strongly affects  $\rho_{\sigma}^{\text{geom}}(\omega)$ . Therefore, the increase of the geometrical average by the broadening weight should be taken into account to investigate the Anderson localization by using numerical methods.

We describe how to estimate the increase of the geometrical average and determine the Anderson transition points as follows.

- (i) Determine the Anderson transition point in noninteracting systems from the results reported in the previous study[103].
- (ii) Define the value of integral of  $\rho_{\sigma}^{\text{geom}}(\omega)$  with respect to energy as,

$$\rho_{\sigma}^{\text{extend}} = \int_{-\infty}^0 d\omega \rho_{\sigma}^{\text{geom}}(\omega), \quad (3.3)$$

and estimate  $\rho_{\sigma}^{\text{extend}}$  at the Anderson transition point determined in step (i).

- (iii) Regard the value evaluated in step (ii) as the minimum value of  $\rho_{\sigma}^{\text{extend}}$  in metallic states, and the points where  $\rho_{\sigma}^{\text{extend}}$  becomes equal to this minimum value in  $U \neq 0$  as the Anderson transition points in interacting systems.

In this study, we determine the critical disorder strength  $D_c=8$  in noninteracting systems. To evaluate the minimum value of  $\rho_{\sigma}^{\text{extend}}$ , we systematically calculate  $\rho_{\sigma}^{\text{extend}}$  for several values of  $\delta$ . The results are presented in Fig. 3.4. The supplemental explanation of  $\rho_{\sigma}^{\text{extend}}$  should be noted here.  $\rho_{\sigma}^{\text{extend}}$  denotes how many extended states remain below the Fermi energy. Because spatial nonuniformity makes the states localized from those at the lowest energy,  $\rho_{\sigma}^{\text{extend}}$  might be also a good criterion for the Anderson transition. We determine the minimum value of  $\rho_{\sigma}^{\text{extend}}$  from Fig. 3.4 as follows;  $\{\rho_{\sigma}^{\text{extend}}\}_{\min}=0.011$  if  $\delta=0.01$ ,  $\{\rho_{\sigma}^{\text{extend}}\}_{\min}=0.0057$  if  $\delta=0.005$ , and  $\{\rho_{\sigma}^{\text{extend}}\}_{\min}=0.0017$  if  $\delta=0.001$ . These  $\{\rho_{\sigma}^{\text{extend}}\}_{\min}$  are nearly equal to the values of the broadening weight and becomes small as the broadening weight lessens. These results of  $\{\rho_{\sigma}^{\text{extend}}\}_{\min}$  are expected, and thus our results seem to be reliable.

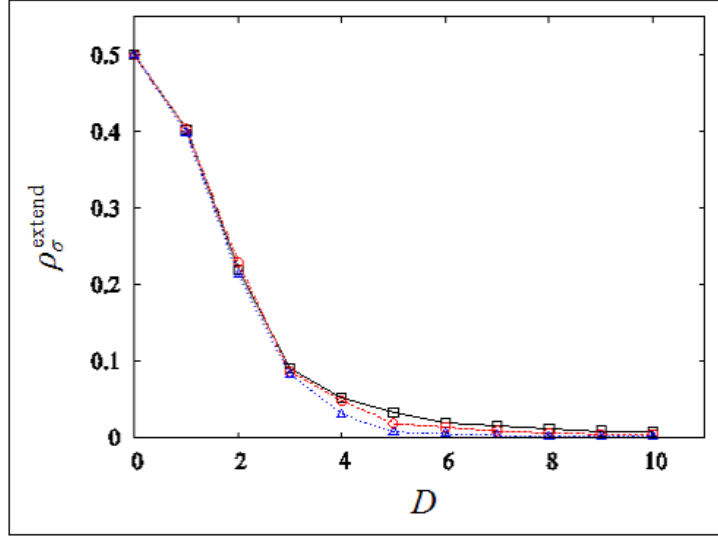


Fig. 3.4  $\rho_\sigma^{\text{extend}}$  as a function of the disorder strength  $D$  for three different values of broadening weight,  $\delta=0.01$  (black solid line with open squares),  $\delta=0.005$  (red dotted line with open circles), and  $\delta=0.001$  (blue dashed line with open triangles) in noninteracting systems at zero temperature. This figure indicates that  $\delta$  becomes to strongly affect  $\rho_\sigma^{\text{geom}}(\omega)$  with increase of the disorder strength whereas the influence of  $\delta$  is negligible in weakly disordered regions ( $D < 3$ ).

### Superfluid order parameter in inhomogeneous systems

The above idea was generalized to deal with the antiferromagnetic order in strongly disordered systems[47]. In this paper, the authors calculated the antiferromagnetic order parameter  $m_{\text{AF}}^{\text{geom}}$  from the geometrical average of the local density of states as,

$$m_{\text{AF}}^{\text{geom}} = |n_{\uparrow A}^{\text{geom}} - n_{\uparrow B}^{\text{geom}}|, \quad (3.4)$$

$$n_{\sigma s}^{\text{geom}} = \int_{-\infty}^0 d\omega \rho_{\sigma s}^{\text{geom}}(\omega), \quad (3.5)$$

where  $s=A, B$  denotes sublattice. By using this staggered magnetization  $m_{\text{AF}}^{\text{geom}}$ , they discussed how spatial nonuniformity affects the antiferromagnetic order.

We extend this idea to treat the superfluidity in attractively interacting systems with spatial inhomogeneity, and propose  $\Phi^{\text{geom}}$

$$\Phi^{\text{geom}} = \int_{-\infty}^0 d\omega \{\rho_{i\sigma}^{\text{off}}(\omega)\}^{\text{geom}} \quad (3.6)$$

as a criterion for the disappearance of superfluidity in disordered systems. Here,

$\rho_{i\sigma}^{\text{off}}(\omega)$  is the local off-diagonal order parameter at each site  $i$  and

$$\rho_{i\sigma}^{\text{off}}(\omega) = -\frac{1}{\pi} \text{Im} \mathcal{F}_i(\omega). \quad (3.7)$$

Note here that  $\Phi^{\text{geom}}$  reduces to the usual superfluid order parameter if  $D=0$ . The formula for  $\Phi^{\text{geom}}$  means that only the extended part of Cooper pairs affects the superfluid long-range order.

### Classification of the possible phases of attractive Anderson-Hubbard model with spatial disorder

To characterize the ground state quantum phase,  $\rho_{\sigma}^{\text{extend}}$ ,  $\Phi^{\text{geom}}$ , and several physical quantities are calculated. Before presenting our results, it is instructive to briefly summarize the classification of the possible phases of the attractive Anderson-Hubbard model with uniform disorder. Those phases are the SF phase, the Anderson localized phase, the metallic phase, the Cooper-pair insulating phase, and can be classified as follows. The system is in a

- SF phase if  $\rho_{\sigma}^{\text{extend}} \neq 0$  and  $\Phi^{\text{geom}} \neq 0$ ;
- Anderson localized phase if  $\rho_{\sigma}^{\text{extend}} = 0$ ;
- metallic phase if  $\rho_{\sigma}^{\text{extend}} \neq 0$  and  $\Phi_i = 0$  at all sites;
- Cooper-pair insulating phase if  $\rho_{\sigma}^{\text{extend}} \neq 0$ ,  $\Phi^{\text{geom}} = 0$ , and  $\Phi_i \neq 0$  at some sites.

Here, we recall that in the Cooper-pair insulating phase, the local superfluid order parameter takes a finite value at some sites although the global superfluid order does not exist (see also Fig. 1.13). The characteristic properties and more detailed explanations of those phases are given in the following sections.

#### 3.2.1 Superfluid-insulator transition

In attractively interacting systems without disorder, the superfluid state is stabilized as the ground state. We first discuss how spatial disorder affects the  $s$ -wave superfluidity.  $\Phi^{\text{geom}}$  for different values of interaction strength is plotted as a function of disorder strength in Fig. 3.5. It is seen from Fig. 3.5 that  $\Phi^{\text{geom}}$  gradually decreases as the disorder strength increases and becomes zero at some critical disorder strength. It is confirmed that  $\Phi^{\text{geom}}$  is always zero in the systems with stronger disorder than critical disorder. This result means that the global superfluid order is destroyed by disorder at some critical points. It is also found that the critical disorder strength lessens with increase of  $U$ . This result indicates that the attractive interaction enhances the effects of disorder, and it is consistent with the result that the non-magnetic disorder hardly affects the formation of Cooper-pairs, but strongly

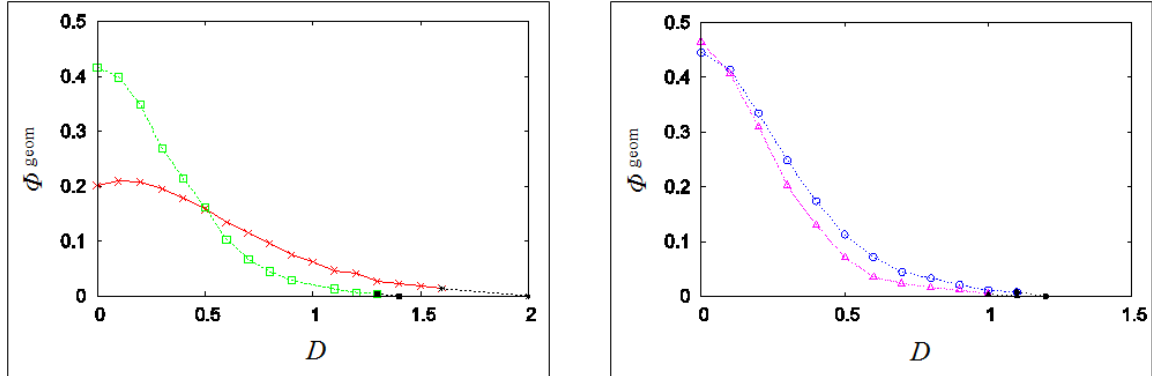


Fig. 3.5  $\Phi^{\text{geom}}$  for four different values of interaction strength  $U=1$  (solid red line with cross marks),  $U=2$  (dotted green line with open squares),  $U=2.5$  (dashed blue line with open circles), and  $U=3$  (chained magenta line with open triangles). Black symbols and dotted lines are not data points (see text).

influences the coherence in the phases of the Cooper-pairs[49]. Note that this tendency is in contrast to that in the repulsive case, i.e. the antiferromagnetic Mott phase[46, 47], where the repulsive interaction suppresses the effects of disorder. We would like to comment that the critical disorder strength is estimated by an extrapolation scheme because converged solutions are not obtained in the vicinity of the critical disorder (see also Fig. 3.5).

For reference, we plot the arithmetic average of the local density of states for two typical disorder strengths  $D=0.2$  and  $2$  in Fig. 3.6.  $D=0.2$  ( $2$ ) is lower (larger) than the critical disorder strength obtained in our study. Both of the coherence

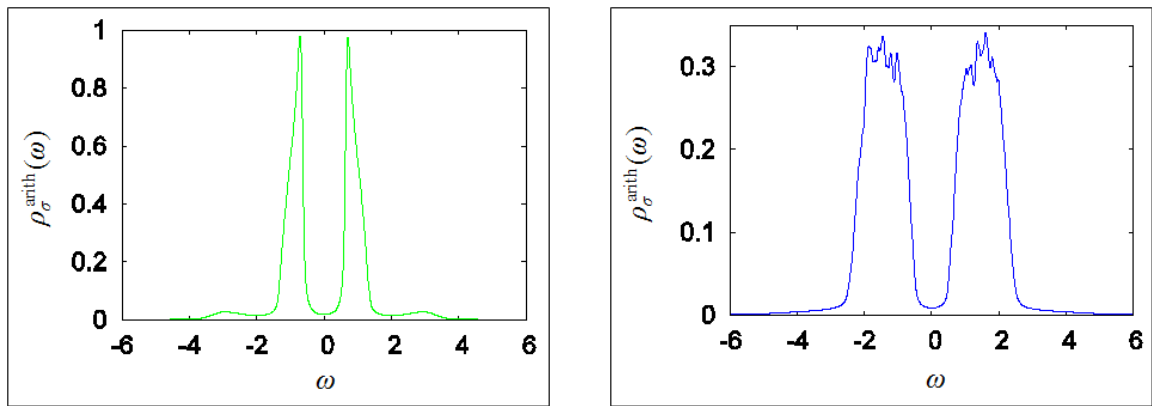


Fig. 3.6 Arithmetic average of the local density of states  $\rho_{\sigma}^{\text{arith}}(\omega)$  for  $D=0.2$  where  $\Phi^{\text{geom}} \neq 0$  (left panel) and  $D=2$  where  $\Phi^{\text{geom}} = 0$  (right panel). We choose  $U=2$ .

peak and the one-particle excitation gap are clearly observed in the left panel of Fig. 3.6. By contrast, we cannot find the coherence peak in the  $D=2$  case although the

one-particle excitation gap remains. The coherence peak signals the coherence in the phase of Cooper-pairs, and the one-particle excitation gap indicates the bond strength of Cooper-pairs. Therefore, these results shown in Fig. 3.6 are also consistent with the results in early studies and might support the above conclusion that the attractive interaction enhances the breaking of the global superfluidity by spatial disorder.

In the distribution function of the local superfluid order parameter  $\Phi_i$ , more interesting information is included. The distribution function  $P(\Phi_i)$  is shown in Fig. 3.7. In the weakly disordered systems ( $D=0.2$ ),  $P(\Phi_i)$  has a sharp peak around  $\Phi_i \sim 0.4$ ,

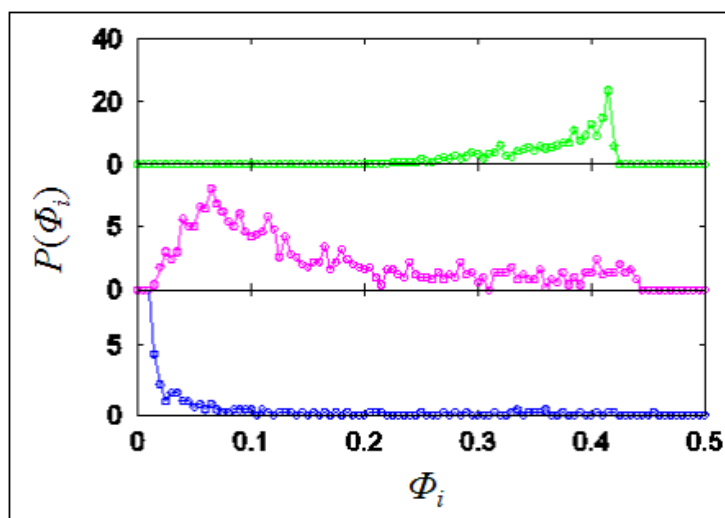


Fig. 3.7 Distribution function  $P(\Phi_i)$  of the local superfluid order parameter at each site for three different disorder strength,  $D=0.2$ ,  $0.6$ , and  $2$  from top to bottom. The upper two panels show the case that  $\Phi^{\text{geom}} \neq 0$ , and the bottom panel the case that  $\Phi^{\text{geom}} = 0$ .  $U=2$  is chosen.

and  $\Phi_i$  ranges from  $\Phi_i \sim 0.42$  to  $\Phi_i \sim 0.25$ . As disorder becomes strong, the peak is shifted to a smaller- $\Phi_i$  region and the corresponding distribution becomes broader ( $D=0.6$ ). This result indicates that with increasing disorder, the superfluid order parameter of the whole system becomes nonuniform. We would like to note here that the probability of  $\Phi_i \sim 0$  is nearly zero in both cases ( $D=0.2$  and  $D=0.6$ ), in accordance with the existence of superfluidity.

We can observe the dramatic change at  $D=2$  where  $P(\Phi_i)$  has a sharp peak at  $\Phi_i \sim 0$ . The distribution of  $\Phi_i \sim 0$  corresponds to the vanishment of the geometrical average  $\Phi^{\text{geom}}$ , and thus signals the disappearance of the global superfluidity. Although the global superfluid order does not exist, a few sites that have large values of  $\Phi_i$  are still found. Such sites are also observed in strongly disordered region ( $D > 2$ ). This characteristic property is more clearly seen in the sample-dependent profile of  $\Phi_i$  shown in Fig. 3.8. In the  $D=2$  and  $U=2$ , both of  $\Phi^{\text{geom}}$  and  $P(\Phi_i)$  indicate that

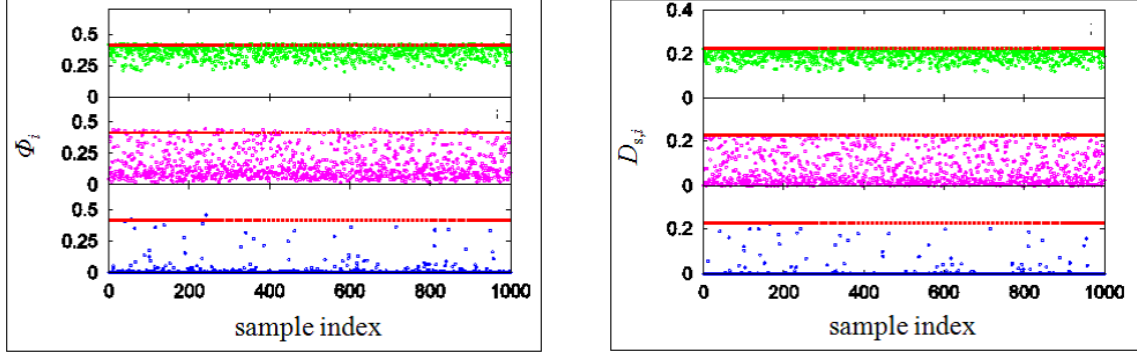


Fig. 3.8 Sample-dependent profiles of  $\Phi_i$  (left panel) and  $D_{s,i}$  (right panel) for three different disorder strength  $D=0.2, 0.6,$  and  $2$  from top to bottom. Red horizontal lines show  $\Phi_i$  and  $D_{s,i}$  at  $D=0$ .  $U=2$  is chosen.

the global superfluidity does not exist, but we can see from Fig. 3.8 that there are many sites having a nonzero local superfluid order parameter. Each sample should correspond to each site in realistic systems, and thus these results imply that the superfluid order may locally survive even after the global superfluidity vanishes.

We have seen that disorder breaks down the global superfluid order and induces the transition. From the properties of systems for  $D > D_{\text{SF}}$  ( $D_{\text{SF}}$  is the critical disorder strength), it is naturally expected that the system is in the Cooper-pair insulating phase discussed in Sec. 2.2. To ensure this expectation, the local superfluid stiffness  $D_{s,i}$  and its geometrical average  $D_s^{\text{geom}}$  are calculated as,

$$D_{s,i} = -\frac{8}{\pi} \int d\epsilon_k \rho_0(\epsilon_k) V(\epsilon_k) \int_{-\infty}^0 d\omega \text{Im} F_i(\omega) \text{Re} F_i(\omega), \quad (3.8)$$

where  $V(\epsilon_k) = (W^2 - \epsilon_k^2)/3$  for the Bethe lattice and  $\rho_0$  is the density of states in  $U=0$  and  $D=0$ . We indeed find that  $D_s^{\text{geom}} = 0$  in the region of  $D > D_{\text{SF}}$ . Our system always has a spectral gap in the entire  $D$  region, and thus it can be concluded that the Drude weight is also zero for  $D > D_{\text{SF}}$ [117]. This result suggests that the insulating state is realized. For reference, we show a sample-profile of the local superfluid stiffness  $D_{s,i}$  in Fig. 3.8. The profile of  $D_{s,i}$  seems to be similar to that of  $\Phi_i$ , but there is one qualitative difference. Comparing the left panel with the right panel of Fig. 3.8, we can see that with increase of the disorder strength, the maximum  $D_{s,i}$  little changes whereas the maximum  $\Phi_i$  increases. This result is consistent with the fact that the disorder effectively enhances the attractive interaction locally; namely, the order parameter  $\Phi_i$  (stiffness  $D_{s,i}$ ) reflects the amplitude (coherence) of a superfluid, which has a tendency to be enhanced (suppressed) as the attractive interaction increases. We also confirm through the systematic analysis that the spectral gap does not close for entire  $D$ . From this result and the above discussions, we conclude that spatial

nonuniformity triggers the transition from the superfluid phase to the Cooper-pair insulating phase.

### 3.2.2 Phase diagram of uniformly-disordered systems

From the systematic calculations of the above quantities, we determine the ground state phase diagram of a two-component Fermi system with spatial disorder at zero temperature and at half-filling, which is plotted in Fig. 3.9. As discussed above, the superfluid-insulator transition points decrease with increasing the disorder strength; namely, the superfluid state becomes less robust against disorder when the strength of the attractive interaction increases, which can be confirmed in Fig. 3.9. Here, some

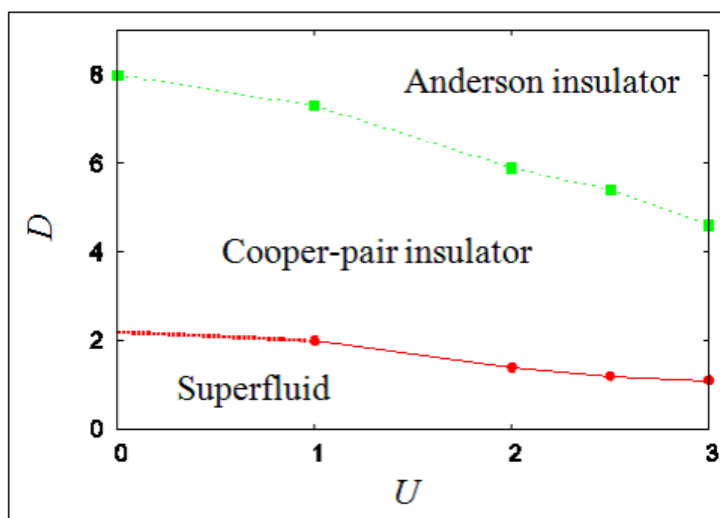


Fig. 3.9 Ground state phase diagram of two-component Fermi systems with uniform disorder at zero temperature and at half-filling. The line with red circles denotes  $D_{SF}$  and the line with green squares  $D_{AL}$ . We draw the red dotted line via the arguments given in the text.

comments on  $U \rightarrow 0$  are in order. Because of the numerical difficulties, the region  $U < 1$  could not be approached. However, we deduce the critical disorder strength  $D_{SF}$  for this region as shown in Fig. 3.9, and the deduction is on the basis of the following two discussions.

- (I) The coherent length exponentially increases as the attractive interaction decreases, and also the superfluid-Cooper-pair insulator transition points are relevant to the strength of the coherence of the superfluidity as discussed above. Therefore, we find it unlikely that  $D_{SF}$  vanishes for  $U \rightarrow 0$ .
- (II) The distribution function of the local superfluid order parameters  $P(\Phi_i)$  becomes broader as the disorder strength increases. It might be improbable that

the superfluidity can continue to exist against very strong disorder.

It should be naturally deduced from these arguments that for  $U \rightarrow 0$  the superfluid-Cooper-pair insulator transition points monotonically increase but converge to a finite value.

It has been argued in the previous subsection that the Cooper-pair insulating state is formed by the localized Cooper-pairs. Thus, it is expected that this insulating state gradually crossovers to the ordinary Anderson localized state as the disorder strength further increases. We calculate  $\rho_\sigma^{\text{extend}}$  (Fig. 3.10) to clarify the character of this crossover, and obtain the line in Fig. 3.9. This line may describe a crossover within the disorder-driven insulating phase; we refer to the two regions as the localized Cooper-pair region (smaller  $D$ ) and the Anderson insulating region (larger  $D$ ). It is found from Fig. 3.10 that the disorder strength, where  $\rho_\sigma^{\text{extend}}$  vanishes,

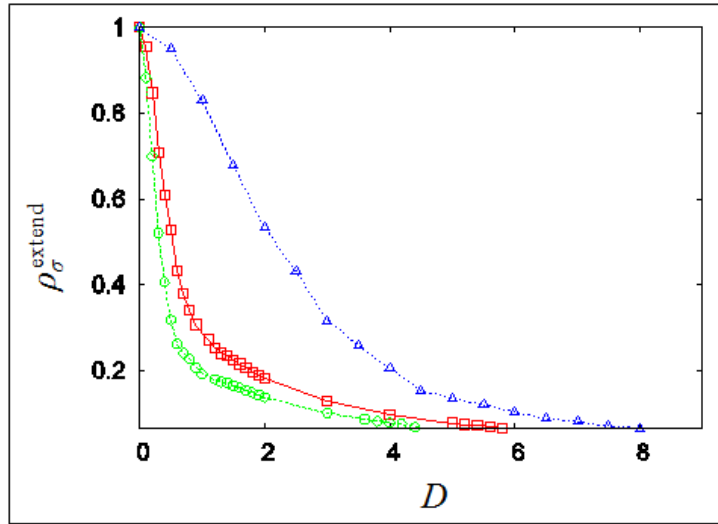


Fig. 3.10  $\rho_\sigma^{\text{extend}}$  for three different attractive interaction strength  $U=0$  (blue dotted line with open triangles),  $U=2$  (red solid line with open squares), and  $U=3$  (green dashed line with open circles). We set the minimum value of this figure to  $\{\rho_\sigma^{\text{extend}}\}_{\min}$  mentioned above.

decreases with the attractive interaction increases, as shown in Fig. 3.9. It has been reported in the previous studies[46, 103] that repulsive interaction and spatial nonuniformity compete with each other, and hence the Anderson transition points, where the metal-Anderson insulator transition occurs, increases with increasing the repulsive interaction. The tendency declared in our study seems to be consistent with that found in the previous studies.

### 3.3 Binary-disordered systems

We here demonstrate the results in the systems with  $\epsilon_i$  is characterized by a binary probability distribution function  $P_{\text{bi}}(\epsilon_i)$  given as,

$$P_{\text{bi}}(\epsilon_i) = \gamma\delta\left(\epsilon_i + \frac{D}{2}\right) + (1 - \gamma)\delta\left(\epsilon_i - \frac{D}{2}\right). \quad (3.9)$$

$P_{\text{bi}}(\epsilon_i)$  is pictured in Fig. 3.11. Comparing Eq. 3.2 with Eq. 3.9, we can find that the

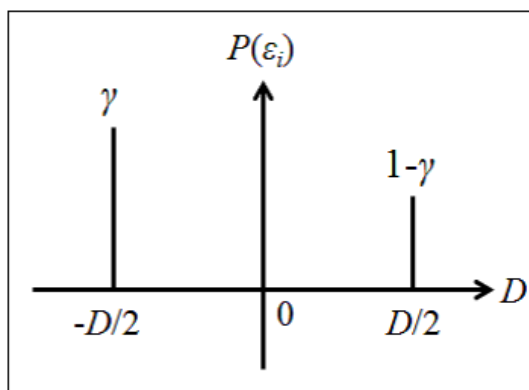


Fig. 3.11 Binary probability distribution function of  $\epsilon_i$ .

additional parameter  $\gamma$  appears only in  $P_{\text{bi}}(\epsilon_i)$ . This  $\gamma$  represents the mixing ratio of atoms in binary alloys, or the ratio of the number of lattice sites to the number of localized atoms in heterogeneous systems which should be realized in cold atomic systems.

It has been reported in previous papers[96, 97, 118] that there is a gap in the one-particle spectrum for sufficiently large  $D$ , and hence the density of states splits into two parts corresponding to the lower and the upper subband. The lower (upper) subband is relevant to  $\epsilon_i = -D/2$  ( $D/2$ ), and the ratio of the number of states in each subband is characterized by  $\gamma$ . From this property, it is known that two metal-insulator transitions occur in non-interacting systems with binary disorder; the band insulator transition occurs for  $n=2\gamma$ , where  $n$  denotes the particle density of the whole system, while the Anderson transition occurs otherwise. It may be easily seen that binary disorder triggers the metal-Anderson transition because the spatial non-uniformity caused by binary disorder is qualitatively similar to that by uniform disorder. The metal-band insulator transition induced by disorder should be observed only in binary-disordered systems when, after the band-splitting occurs, the lower subband is fully occupied and the upper subband is empty, namely the condition  $n=2\gamma$  is satisfied. The spectral gap is characterized by  $D$  in the band insulating

systems. In order to analyze how the effects of the band splitting and the spatial nonuniformity due to binary disorder influence an  $s$ -wave superfluid in attractively interacting systems, we consider two different conditions;  $n \neq 2\gamma$  and  $n = 2\gamma$ .

Here, we would like to comment on the different characteristic condition  $n = \gamma$ , where the lower band is just-half occupied after band-splitting occurs. In this condition, Mott insulating states[97] and antiferromagnetic states might be realized in repulsively interacting systems, and we would observe charge-density-wave states in attractively interacting systems. In this study, we focus on the superfluidity in the attractively interacting systems with spatial non-uniformity, and it is expected that there are no characteristic properties of the superfluidity which are observed just in  $n = \gamma$  because the superfluid order does not qualitatively depend on the filling of the whole systems. For this reason, we consider only the two conditions  $n \neq 2\gamma$  and  $n = 2\gamma$  mentioned above.

As done in the analysis on the uniformly disordered systems, we systematically calculate  $\rho_\sigma^{\text{geom}}(\omega)$ ,  $\rho_\sigma^{\text{extend}}$ ,  $\Phi_i$ ,  $\Phi^{\text{geom}}$ , and so on to characterize the quantum phases stabilized as the ground state in the binary-disordered systems. The possible phases are a band insulating phase and the four different phases which are also realized in uniformly disordered systems; SF phase, Anderson localized phase, metallic phase, and Cooper-pair insulating phase. The phase is classified into a band insulating phase if  $\rho_\sigma^{\text{geom}}(\omega)$  has a gap at the Fermi level,  $\Phi^{\text{geom}} = 0$ , and  $\Phi_i = 0$  at all sites. The classification of the other phases is noted in Sec. 3.2.

### 3.3.1 $n \neq 2\gamma$

First, we present the results of  $n \neq 2\gamma$ . In this condition,  $n = 0.2$  and  $\gamma = 0.2$  are selected, and the Bethe lattice with the connectivity  $K = 6$  is considered.  $\Phi^{\text{geom}}$  and  $\rho_\sigma^{\text{extend}}$  are calculated in the same manner as the case of uniform disorder, and shown in Fig. 3.12. We can see from Fig. 3.12 that these quantities monotonically decrease with increasing the disorder strength and vanish at some  $D$ . Also, from the comparison between these figures and Figs. 3.5 and 3.10, it is confirmed that this tendency observed in the systems with binary disorder is qualitatively similar to that in the systems with uniform disorder.

We estimate  $D_{\text{SF}}$  and  $D_{\text{AL}}$  from the results of  $\Phi^{\text{geom}}$  and  $\rho_\sigma^{\text{extend}}$ , and determine the ground state phase diagram of the attractively interacting systems with binary disorder at zero temperature in  $n \neq 2\gamma$  (Fig. 3.13). It is noted that the red dotted line on the  $U < 1$  region in Fig. 3.13 is drawn through the discussion in Sec. 3.2.2. We would like to comment on the phase diagram here. Although Fig. 3.13 is the phase diagram at  $n = 0.2$  and  $\gamma = 0.2$ , it is confirmed that the phase diagram at the different parameters (for examples,  $n = 0.5$  and  $\gamma = 0.5$ ) in this condition  $n \neq 2\gamma$  qualitatively

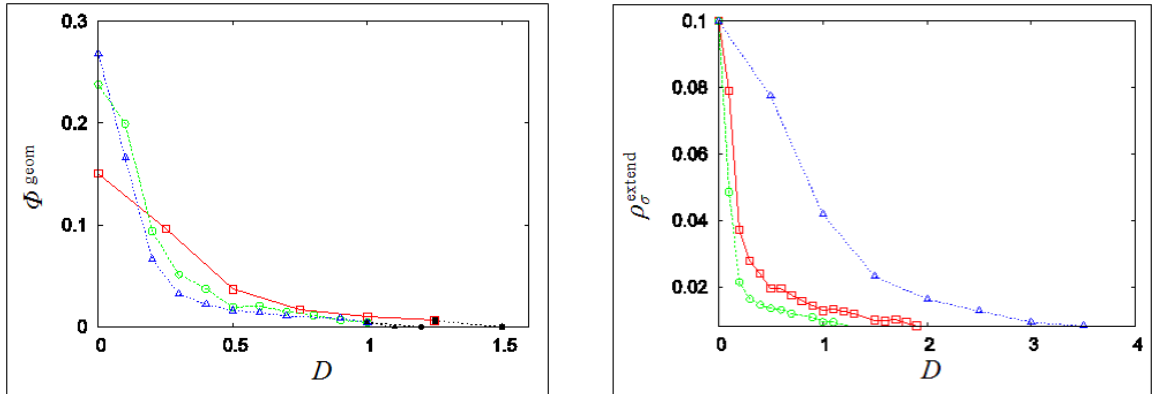


Fig. 3.12 (Left panel)  $\Phi^{\text{geom}}$  for three different values of the interaction strength  $U=1$  (solid red line with open squares),  $U=2$  (dotted green line with open circles), and  $U=3$  (dashed blue line with open triangles). Black symbols and dotted lines are not data points (see text). (Right panel)  $\rho_{\text{extend}}$  for three different attractive interaction strengths  $U=0$  (blue dotted line with open triangles),  $U=2$  (red solid line with open squares), and  $U=3$  (green dashed line with open circles).

conforms to the phase diagram shown in Fig. 3.13.

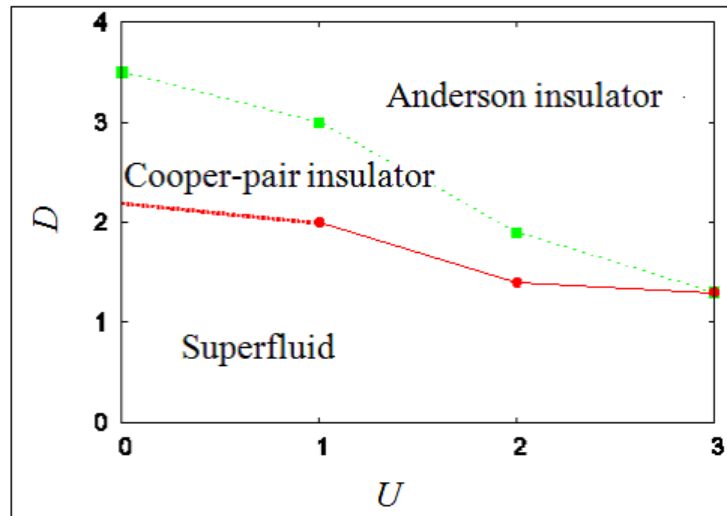


Fig. 3.13 Ground state phase diagram of two-component Fermi systems with binary disorder at zero temperature in  $n \neq 2\gamma$ . The line with red circles (with green squares) denotes  $D_{\text{SF}}$  ( $D_{\text{AL}}$ ). The red dotted line is drawn via the arguments given in the text.

It can be read from the phase diagram of binary-disordered systems that the superfluid state undergoes a transition to the Cooper-pair insulating state at some critical disorder strength, and the Cooper-pair insulating state crossovers to the Anderson insulating state as spatial nonuniformity further increases. The phases stabilized as

the ground state in the binary-disordered systems with an attractive interaction are similar to those in the uniformly disordered systems. Also, in both of the uniformly disordered systems and the binary-disordered systems, we can observe the tendency that both of  $D_{\text{SF}}$  and  $D_{\text{AL}}$  decrease with increase of an attractive interaction. From these results, we conclude that in  $n \neq 2\gamma$ , the band-splitting effects due to binary disorder do not strongly influence the properties and thus spatial nonuniformity plays a dominant role in dictating the properties of the whole systems.

### 3.3.2 $n=2\gamma$

Here, we select  $n=1$  and  $\gamma=0.5$  which satisfy  $n=2\gamma$ , and consider the Bethe lattice with  $K=3$ . In the condition  $n=2\gamma$ , the quantitative difference between the systems with uniform disorder and binary disorder is observed. We plot the geometrical average of the local superfluid order parameter and the sample-dependent profile of  $\Phi_i$  in Fig. 3.14. The left panel of Fig. 3.14 indicates that the global superfluid order

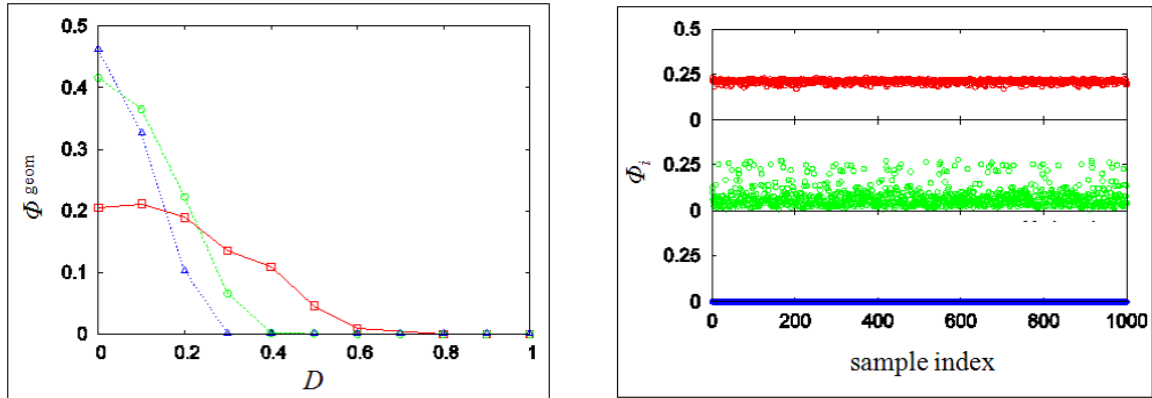


Fig. 3.14 (Left panel)  $\Phi^{\text{geom}}$  for three different values of interaction strength  $U=1$  (solid red line with open squares),  $U=2$  (dotted green line with open circles), and  $U=3$  (dashed blue line with open triangles). Black symbols and dotted lines are not data points (see text). (Right panel) Sample-dependent profile of  $\Phi_i$  for three different disorder strength  $D=0.1, 0.5,$  and  $1$  from top to bottom. We choose  $U=1$ .

is destroyed at some critical disorder  $D_{\text{SF}}$ . The destruction of the global superfluidity due to disorder is also observed in the systems with uniform disorder. However, the right panel of Fig. 3.14 demonstrates the marked difference between the systems with uniform disorder and binary disorder.  $\Phi_i$  widely ranges but takes a finite value at all sites in the weakly disordered regions  $D < D_{\text{SF}}$ . By contrast, in the strongly disordered regions,  $D > D_{\text{SF}}$ ,  $\Phi_i$  is equal to zero at all sites. This result demonstrates that the superfluid order does not exist even locally at  $D > D_{\text{SF}}$ , and thus binary disorder triggers the superfluid-band insulator transition.

The spectral gap caused by the band-splitting effects should characterize the band insulating phase. We plot the spectral gap width as a function of  $D$  in Fig. 3.15. We can see from Fig. 3.15 that the spectral gap width gradually lessens in the

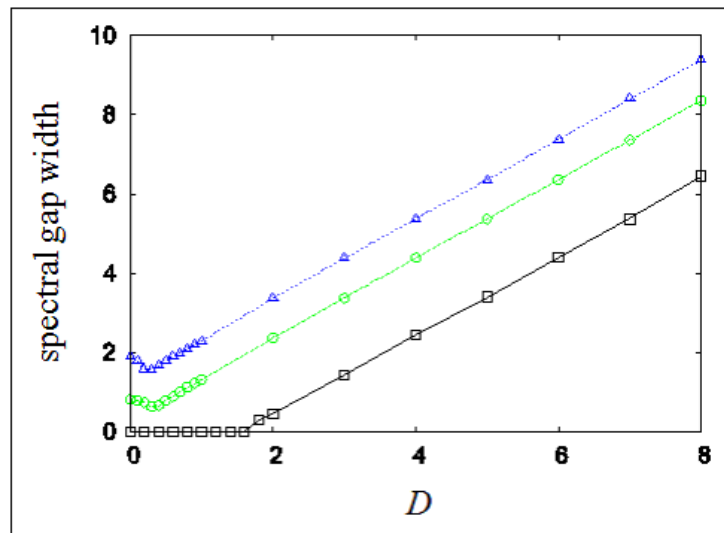


Fig. 3.15 Spectral gap width as a function of the disorder strength  $D$ . Black solid line with open squares shows the noninteracting case, green dotted line with open circles the  $U=2$  case, and blue dashed line with open triangles the  $U=3$  case.

superfluid phase as the disorder strength increases, but this tendency becomes opposite at transition points and thus the spectral gap width linearly increases with increasing the disorder strength. This linear increase is one of the characteristic properties of the band insulating state induced by binary disorder. Also, comparing the three lines shown in Fig. 3.15, we can find that the gap width increases as an attractive interaction increases, namely an attractive interaction enhances the band splitting effects. Therefore, the critical disorder strength lessens with increasing the attractive interaction strength.

At the end of this section, the ground state phase diagram is shown in Fig. 3.16. As shown in the phase diagram, the alloy subbands are formed in this condition  $n=2\gamma$ , and hence the superfluid-band insulator transition occurs at some critical disorder. An attractive interaction enhancing the band splitting effects, the critical disorder, where the superfluidity is completely destroyed, decreases. The superfluid-band insulator transition is characteristic of binary-disordered systems, and this transition does not appear in the phase diagram of the systems with uniform disorder.

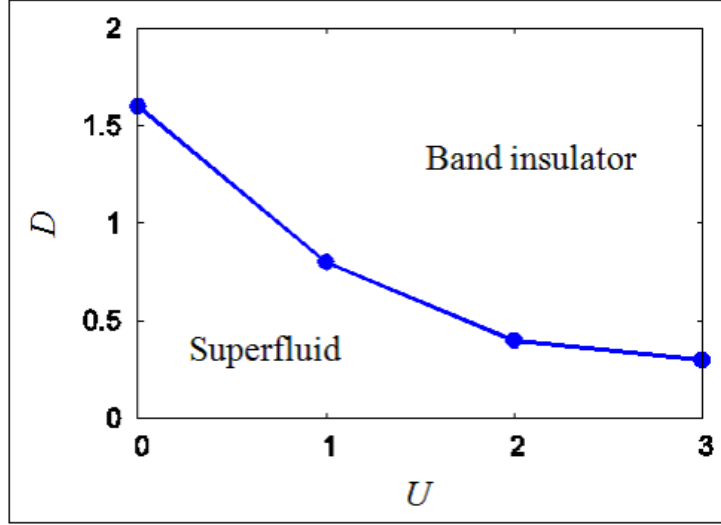


Fig. 3.16 Ground state phase diagram of two-component Fermi systems with binary disorder at zero temperature in  $n=2\gamma$ . The solid line with blue closed circles denotes the superfluid-band insulator transition points.

### 3.4 Summary

We summarize the results of our study of two component attractively interacting Fermi systems with spatial disorder. In this study, the Anderson-Hubbard model, which is well-described such systems, was investigated by employing the statistical DMFT combined with mIPT. Uniform disorder and binary disorder were used as the distribution of spatial disorder. We calculated the superfluid order parameter, the local one-particle spectrum and the superfluid stiffness, and determined the ground state phase diagrams at zero temperature. In the obtained phase diagrams for the uniform disorder, it was clarified that the superfluid-insulator transition points decrease with increasing the strength of the attractive interaction. Moreover, we elucidated that the Cooper-pair insulating region crossovers to the Anderson insulating region as the strength of spatial disorder increases. In the study of binary-disordered systems, we found that not band-splitting effects but spatial inhomogeneity due to binary disorder plays a main role in dictating the properties of whole systems on  $n \neq 2\gamma$ . Also, it was clarified that the superfluid-band-insulator transition, which is characteristic of the systems with binary disorder, occurs on  $n=2\gamma$ . Through these studies, we found that attractive interaction enhances the effects of spatial disorder.

## Chapter 4

# Multicomponent systems with spatial nonuniformity

Based on the knowledge which is obtained in the study of the two-component Fermi systems, we theoretically investigate the multicomponent Fermi systems with spatial inhomogeneity. As described in Chap. 1, these systems can be realized in cold atoms and thus well-described by the multicomponent Anderson-Hubbard model described in Eq. 2.78. Using the BdG equations, we analyze this Hamiltonian for  $N=3$  and  $N=4$ , where  $N$  is the number of components. Therefore, we clarify the quantum phase transitions which are characteristic of the multicomponent Fermi systems. The ground state phase diagrams of the three- and four-component systems are determined. We also argue what will be expected for  $N>4$  cases. In this chapter, we first explain the important problem of the multicomponent Fermi systems with spatial nonuniformity, and then show the obtained results.

### 4.1 Ground state of multicomponent systems with disorder

Here, we consider the multicomponent Anderson-Hubbard model with isotropic attractive interaction, namely the  $SU(N)$  attractive Anderson-Hubbard model. It is known that in the  $SU(2)$  model without disorder, the density-wave (DW) state and the  $s$ -wave superfluid (SF) state are degenerate at zero temperature and at half-filling (one atom per site in average) on a two-dimensional square lattice[48, 69]. The spatial nonuniformity lifts this degeneracy, and therefore stabilizes the SF state as the ground state. This is because on-site randomness strongly affects the density correlation whereas, as discussed in Sec. 1.2, the Cooper-pairs are rather robust against diagonal nonmagnetic disorder. On the other hand, in  $SU(N>2)$  systems without disorder, the DW state is stabilized as the ground state because the energy gained by the condensation of Cooper pairs is smaller than that gained by the DW order

(see also Sec. 2.2). We summarize the above discussion schematically in Fig. 4.1. Note here that in Fig. 4.1, we schematically express only the comparison of the free

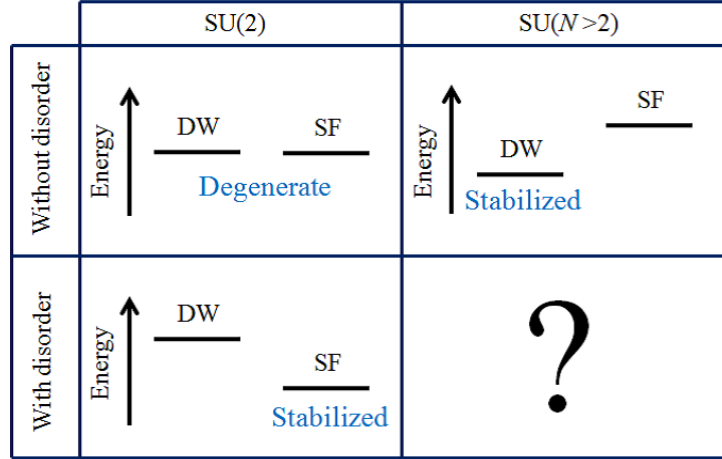


Fig. 4.1 Phases stabilized as the grand state of  $SU(N)$  Fermi systems with and without disorder. The comparison of the free energies between the DW state and the SF state in each system is schematically expressed in this figure.

energies between the DW state and the SF state in each system. Indeed, the spatial disorder should cause the decrease of the free energy of systems. As shown in Fig. 4.1, what kind of state is realized as the ground state in the  $SU(N>2)$  systems with disorder is an interesting open question. In particular, it should be clarified whether the SF state can dominate the DW state in the presence of disorder.

In order to answer this open question, we investigate the  $SU(N>2)$  attractively interacting Fermi systems with diagonal disorder in a two-dimensional square lattice at zero temperature and at half-filling. The  $N=3$  case and the  $N=4$  case are calculated within the BdG equations, and the uniform distribution function (Eq.(3.2)) is used as a disorder distribution.

We set the hopping amplitude  $t=1$  as a unit energy in the study of multicomponent Fermi systems. The superfluid state where  $(\Phi^{ba}, \Phi^{cb}, \Phi^{ac})=(\Phi^{ba}, 0, 0)$  and  $\Phi^{ba} \neq 0$  is chosen as an initial state. The validity of this choice is discussed in Sec. 2.2. The calculation is performed for the lattice sizes up to  $M=32 \times 32$  ( $M$  represents the number of sites) and a periodic boundary condition is imposed on the lattices. The calculation for the different lattice sizes is also performed. Hence, it is confirmed that results obtained in our study just quantitatively depend on lattice sizes. We average the results over 12—40 different realizations to eliminate the sample dependence.

## 4.2 SU(3) Fermi systems with spatial nonuniformity

Before presenting the results, we explain the classification of the phases which would be realized in the SU( $N$ ) Fermi systems with attractive interaction and spatial inhomogeneity. The system is in a

- DW phase if the periodic oscillation of the density-density correlation function is clearly observed and spectral has a gap at the Fermi level;
- SF phase if all local superfluid order parameters take a finite value and the spectral gap is closed (open) for odd  $N$  (for even  $N$ );
- Cooper-pair insulating phase if the site-average of local superfluid order parameters takes a finite value but the local superfluid order parameters at some sites equal to zero;
- Anderson localized (AL) phase if local superfluid order parameters at all sites equal to zero and the spectral does not have a gap at the Fermi level.

It should be commented that due to the difference in the theoretical methods used, this classification of the phases is slightly different from that described in Sec. 3.2. In the study of multicomponent Fermi systems, we classify the phases based on the above definition. Our calculations are performed for the two-dimensional lattices, and it has been shown in Cap. 3 that the attractive interaction enhances the localization of particles. Thus, we find it unlikely that the metallic state realizes in the two-dimensional attractively interacting systems with spatial inhomogeneity. For this reason, the metallic phase is not included in the above classification.

### 4.2.1 Density-density correlation

In the SU(3) systems with on-site attractive interaction and diagonal disorder, the density-wave state realizes as the ground state. To elucidate how spatial inhomogeneity influences the DW state, we calculate the density-density (d-d) correlation function  $D(r_i - r_j)$ , where  $r_i$  denotes the coordinate of site  $i$ .  $D(r_i - r_j)$  is given as,

$$D(r_i - r_j) = \left\langle \left( \sum_{\sigma} \hat{n}_{i\sigma} - n_{\text{half}} \right) \left( \sum_{\sigma'} \hat{n}_{j\sigma'} - n_{\text{half}} \right) \right\rangle, \quad (4.1)$$

where  $n_{\text{half}}$  ( $=3/2$ ) denotes at the half-filling. Within the mean-field treatment, the above formula is evaluated with Wick's theorem and thus is rewritten as,

$$D(r_i - r_j) = \left( n_i - n_{\text{half}} \right) \left( n_j - n_{\text{half}} \right). \quad (4.2)$$

$D(r_i - r_j)$  is plotted in Fig. 4.2. As shown in the upper two panels of Fig. 4.2, the

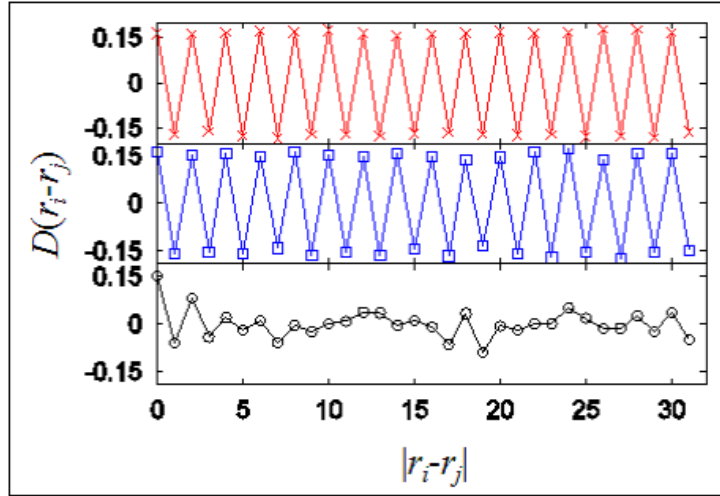


Fig. 4.2 Density-density correlation function for three different values of the disorder strength,  $D=0.2$  (red line with crosses),  $D=0.4$  (blue line with squares), and  $D=0.8$  (black line with circles) from top to bottom. The horizontal axis represents the distance between sites.  $U=0.8$  is fixed.

oscillatory character of the density correlation, which indicates the existence of the checker-board type density-wave order, is clearly observed in the weakly disordered regions. By contrast, this periodic oscillation disappears in the strongly disordered regions (see the bottom panel of Fig. 4.2). This result means that spatial nonuniformity breaks down the density-wave order. Note here that  $D(r_i - r_j)$  ( $r_i \neq r_j$ ) cannot exactly become equal to zero in disordered systems even if the density-wave order does not exist. This is because the local particle density  $n_i$  may deviate from the half-filling condition ( $n_i=3/2$ ) due to spatial disorder even when the whole system is at half-filling in average. However, the finite amplitude of  $D(r_i - r_j)$  caused by disorder is not periodic in distance between sites  $|r_i - r_j|$ , as plotted in the bottom panel of Fig. 4.2. Therefore, we can figure out whether the CDW order exists in disordered systems by observing the periodicity of  $D(r_i - r_j)$ .

For reference, we plot the density structure factor  $S_{\text{DW}}$  associated with the density-density correlation function in Fig. 4.3.  $S_{\text{DW}}$  provides a criterion for the robustness of the density-wave order and is given by,

$$S_{\text{DW}} = \frac{1}{M^2} \sum_{i,j} C(r_i - r_j) (-1)^{|r_i - r_j|}. \tag{4.3}$$

As found from Fig. 4.3,  $S_{\text{DW}}$  takes a finite value in weakly disordered regions and decreases with increasing the disorder strength. The dramatic fall-off of  $S_{\text{DW}}$  is observed at a finite disorder strength, and  $S_{\text{DW}}$  becomes nearly equal to zero when  $D$  is larger than the finite disorder. This result also implies as with the result of

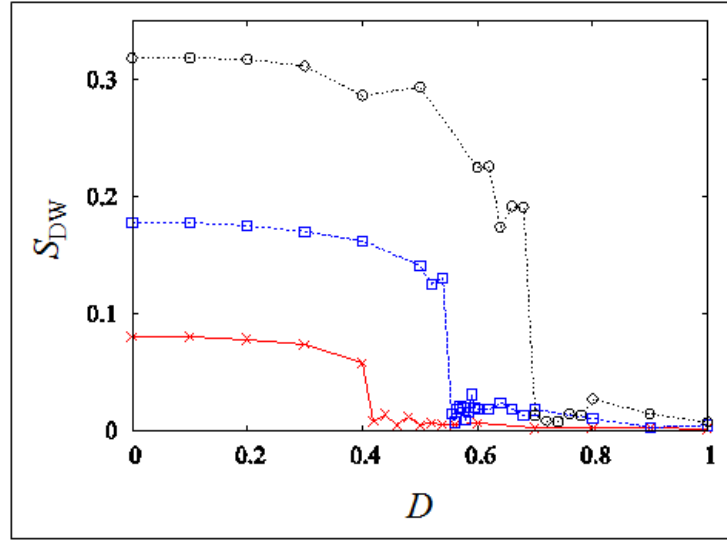


Fig. 4.3 Density structure factor as a function of the disorder strength. Red solid line with crosses represents  $S_{\text{DW}}$  for  $U=0.6$ , blue dotted line with squares for  $U=0.8$ , and black dashed line with circles for  $U=1$ .

$D(r_i - r_j)$  that spatial inhomogeneity breaks down the density-density correlation at finite critical disorder. Note that  $S_{\text{DW}}$  is not exactly zero even if density-density correlation does not exist for the reason described in the discussion of  $D(r_i - r_j)$ .

#### 4.2.2 Superfluid state in SU(3) systems

In order to answer the question what kind of phase is stabilized in the region without the density-density correlation, we calculate local superfluid order parameters  $\Phi_i^{\sigma\bar{\sigma}}$  and the site-average of them  $\Phi^{\sigma\bar{\sigma}}$  which is defined as,

$$\Phi^{\sigma\bar{\sigma}} = \frac{1}{M} \sum_i \Phi_i^{\sigma\bar{\sigma}}. \quad (4.4)$$

We plot  $\Phi^{ba}$  as a function of  $D$  in Fig. 4.4.  $\Phi^{ba}=0$  in the weakly disordered regions where the density-density correlation develops. In contrast, in the regions where strong disorder causes the destruction of the DW order,  $\Phi^{ba}$  takes a finite value. It is confirmed that the disorder strength, where the rapid fall of  $S_{\text{DW}}$  is observed, coincides with that where  $\Phi^{ba}$  starts taking a finite value. In addition to these results, we construct the histogram of local superfluid order parameters  $P(\Phi_i^{ba})$ , which is shown in Fig. 4.5. We can see from Fig. 4.5 that the mode value of  $P(\Phi_i^{ba})$  is almost equal to the arithmetic average of  $\Phi_i^{ba}$  although  $P(\Phi_i^{ba})$  has a finite variance, and hence the arithmetic average reflects the properties of the whole system.  $P(\Phi_i^{ba})$  includes the further valuable information that the local superfluid order parameters

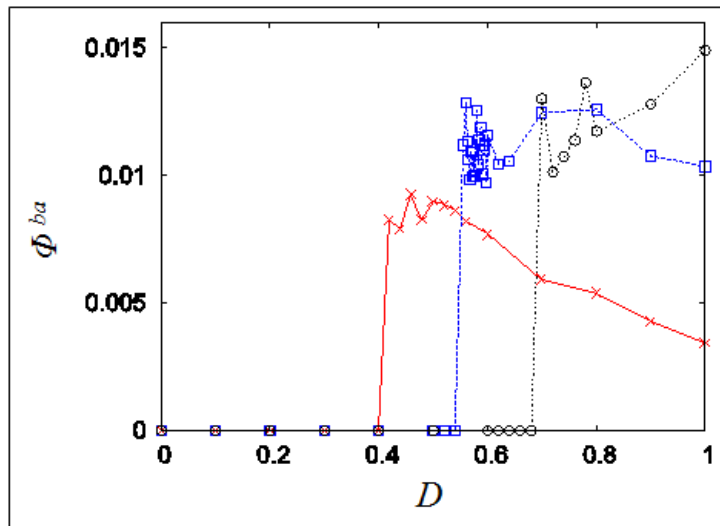


Fig. 4.4 Site-averaged superfluid order parameter  $\Phi^{ba}$  for  $U=0.6$  (red solid line with crosses),  $U=0.8$  (blue dotted line with squares), and  $U=1$  (black dashed line with circles).

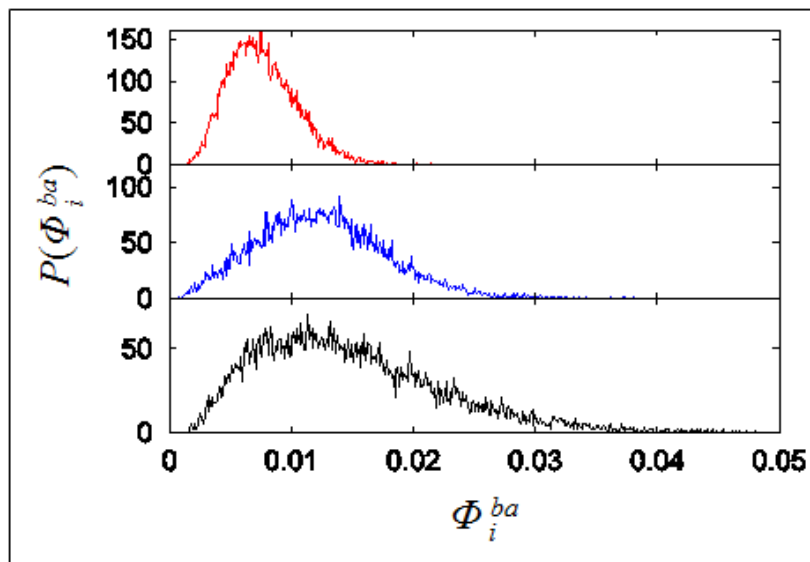


Fig. 4.5 Histogram of local superfluid order parameters for three different parameter regions,  $(U, D)=(0.6, 0.6)$ ,  $(0.8, 0.8)$ , and  $(1, 1)$  from top to bottom. In these regions, the oscillatory character of the density-density correlation does not appear.

are not zero at all sites. As discussed in Sec. 2.1, this results indicates that the superfluid order globally develops in the whole system. We conclude from these results that the SF state realizes in the regions where the density-wave order does not exist, namely spatial nonuniformity triggers the DW-SF transition. We would like to emphasize that the DW-SF transition predicted in our study is characteristic of the multicomponent Fermi systems, and this transition cannot be observed in SU(2) systems unless the systems are subject to the perturbations which stabilize the DW state, such as superlattice potential.

### 4.2.3 Disorder-induced DW-SF transition

We uncover the disorder-induced DW-SF transition. Our next concern is the nature of this transition. We can see from Figs. 4.3 and 4.4 that both of the density structure factor and the superfluid order parameter suddenly change at transition points. These results suggest that the disorder-induced DW-SF transition is of first order. To ensure this expectation, we calculate the free-energies corresponding to the DW state ( $F_{\text{DW}}$ ) and the SF state ( $F_{\text{SF}}$ ), and thereby confirm that both of  $F_{\text{DW}}$  and  $F_{\text{SF}}$  decrease as the disorder strength increases. It is also observed that  $F_{\text{DW}}=F_{\text{SF}}$  at a critical disorder strength, and  $F_{\text{DW}}>F_{\text{SF}}$  in the region where  $D$  is larger than a critical disorder strength. This inversion of the free energies of each phase is a feature of the first-order transition. This result should support that the disorder-triggered DW-SF transition is of first order.

In order to discuss the properties of the DW-SF transition, the site-averaged density of states  $\rho(\omega)$  in both phases is shown in Fig. 4.6.  $\rho(\omega)$  is defined as,

$$\rho(\omega) = \frac{1}{NM} \sum_{i,\sigma} \rho_{i\sigma}(\omega) \quad (4.5)$$

$$= \frac{1}{NM} \sum_{i,m} \left\{ |v_m(r_i)|^2 \delta(\omega + E_m) + |u_m(r_i)|^2 \delta(\omega - E_m) \right\}, \quad (4.6)$$

where  $\rho_{i\sigma}$  is the local density of states which depends on site  $i$  and spin  $\sigma$ . We can see from the top three panels of Fig. 4.6 that the spatial nonuniformity lessens the spectral gap width, which indicates the DW order is suppressed by the disorder. Comparing the bottom panel of Fig. 4.6 with the top three panels, we can observe the notable difference in the density of states between the DW phase and the SF phase. The spectral gap which is open at the Fermi level in the DW phase does not exist in the SF phase. This difference suggests that the spectral gap at the Fermi level closes at the DW-SF transition points. Namely, the spatial disorder destroys the spectral gap formed by the DW order, and triggers the DW-SF transition. For confirmation, we systematically estimate the spectral gap width. Thus, it is found that the spectral

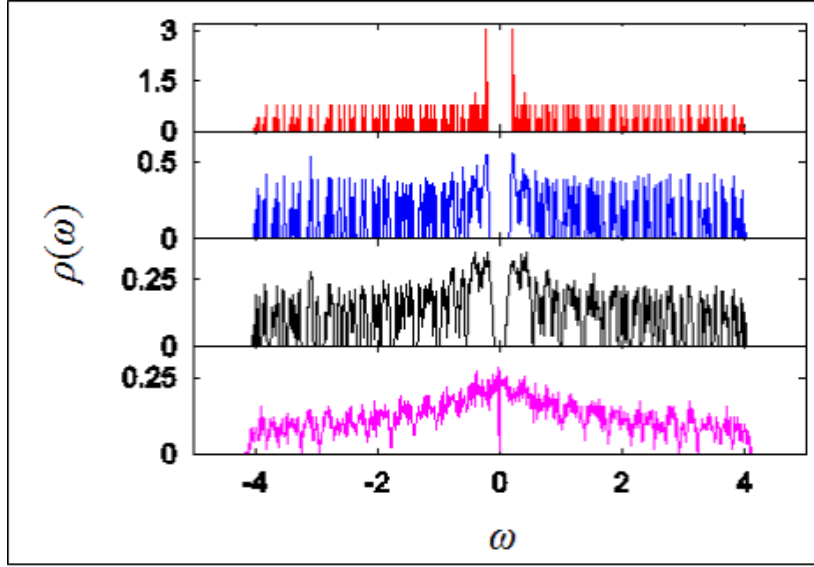


Fig. 4.6 Site-averaged density of states for four different disorder strengths,  $D=0, 0.2, 0.4$ , and  $0.8$  from top to bottom. The top three panels represent them in a DW phase and the bottom panel it in a SF phase.  $U=0.8$  is chosen.

gap width becomes zero at the critical disorder strength and the gap always closes at  $D$  which is larger than the critical disorder. We note here that although the spectral gap caused by the SF order still exists in the density of states for spin  $a$  and  $b$ , that for spin  $c$  does not exist. This is because, as mentioned above, the particles with spin  $c$  are not in the SF state, but in the unpaired Anderson localized state. Thereby, the density of states for the spin  $c$  leads to the finite density of states at the Fermi level in total.

More notable information is included in the probability distribution function of the local particle density  $P(n_i)$ . We show  $P(n_i)$  for the four different parameter regions in Fig. 4.7. From Fig. 4.7, it is seen that  $P(n_i)$  of the DW phase (top three panels) is bimodal, and there are few sites at which the local particle density  $n_i$  is nearly equal to 1.5. As the disorder strength increases, the two peaks observed in  $P(n_i)$  of the DW phase become broader. Finally, these peaks disappear, and then  $P(n_i)$  is reduced to a single-peak distribution which has a finite weight even at  $n_i = 1.5$ . The local particle density at each site is an observable quantity in cold atoms, and thus it should be easy to experimentally observe this change of the histogram of the local particle density associated with the DW-SF phase transition. We would like to comment that with further increasing the disorder strength, the distribution function  $P(n_i)$  shows a bimodal distribution even in the SF phase. This change of  $P(n_i)$  in the SF phase is consistent with the results given in the previous study[58].

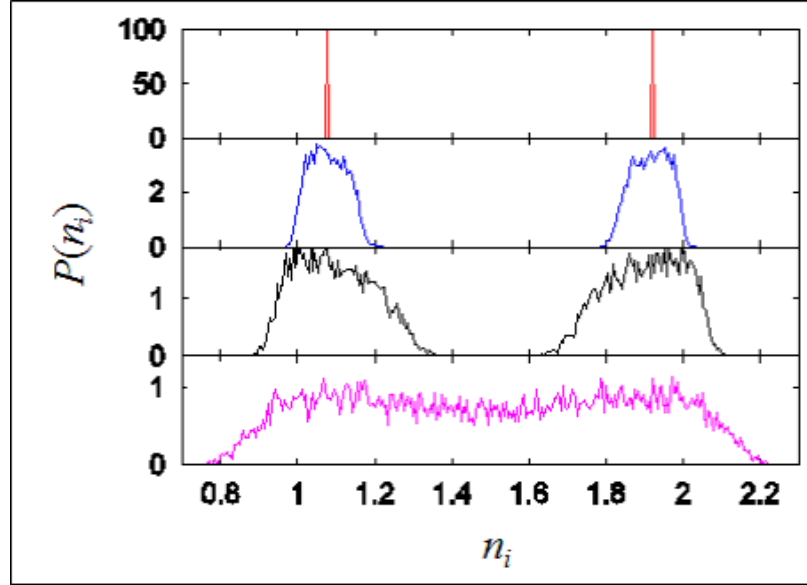


Fig. 4.7 Probability distribution function of the local particle density  $P(n_i)$ ,  $D=0, 0.2, 0.4$ , and  $0.8$  from top to bottom. The top three panels represent them in a DW phase and the bottom panel it in a SF phase.  $U=0.8$  is chosen.

#### 4.2.4 Effective disorder

It has been elucidated from the above discussion that spatial disorder makes the SF phase stable in SU(3) systems. Now, we define the following quantity  $\delta\tilde{\mu}_{i\sigma}$ ,

$$\delta\tilde{\mu}_{i\sigma} = \tilde{\mu}_{i\sigma} - \frac{1}{M} \sum_i \tilde{\mu}_{i\sigma}, \quad (4.7)$$

$$\tilde{\mu}_{i\sigma} = \mu - \epsilon_i + U \sum_{\sigma \neq \bar{\sigma}} n_{i\bar{\sigma}}. \quad (4.8)$$

This quantity  $\delta\tilde{\mu}_{i\sigma}$  denotes the effective lattice potential which particles are subject to in the interacting systems with spatial nonuniformity, and hence we call  $\delta\tilde{\mu}_{i\sigma}$  “effective disorder” hereafter. If  $U = 0$ ,  $\delta\mu_{i\sigma}$  is equal to  $-\epsilon_i$  and the distribution of  $\delta\mu_{i\sigma}$  is reduced to the uniform distribution of “pure disorder”  $\epsilon_i$ , whereas if  $\Delta = 0$ ,  $\delta\mu_{i\sigma}$  is equal to 0.

We systematically calculate  $\delta\tilde{\mu}_{i\sigma}$ , and plot the distributions of  $\delta\tilde{\mu}_{i\sigma}$  in the SF phase for  $N=2$  and  $N=3$  in the left panel of Fig. 4.8. It is found that the region characterizing the distribution of the effective disorder,  $P(\delta\mu_{ia})$ , is wider than that for the uniform distribution function,  $P_{\text{uni}}(\epsilon_i)$ , both for the  $N=2$  and  $3$  cases. It is also seen from this result that attractive interaction enhances the effects of spatial disorder. For example,  $\delta\mu_{ia}$  for  $N=3$  is approximately distributed in the wide region

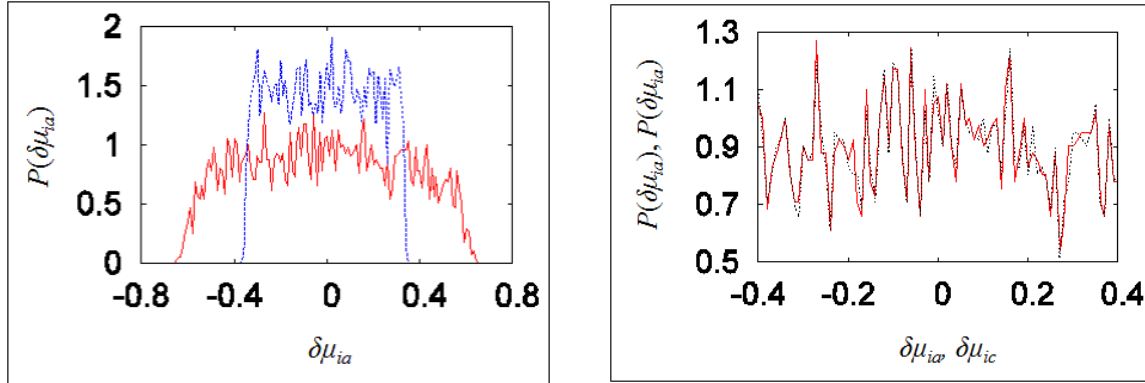


Fig. 4.8 (Left panel) Distribution of effective disorder  $P(\delta\mu_{ia})$  for the particles with spin  $a$ . The red solid line corresponds to the  $N=3$  case and blue dotted line the  $N=2$  case. (Right panel)  $P(\delta\mu_{ia})$  (for the particles which are paired in the SF state) and  $P(\delta\mu_{ic})$  (for the particles which should be localized) in the  $N=3$  case. The red solid line shows  $P(\delta\mu_{ia})$  and the black broken line  $P(\delta\mu_{ic})$ . We choose  $U=0.8$ ,  $D=0.6$ , and  $n=1.5$  in both panels.

of  $-0.6 < \delta\mu_{ia} < 0.6$  whereas  $\epsilon_i$  is in the region of  $-0.3 < \epsilon_i < 0.3$  for  $D=0.6$ . Moreover, we clarify from the systematic calculations that the enhancement of the effects of the spatial disorder by the attractive interaction is most largest when the whole system is at half-filling. Comparing  $P(\delta\mu_{ia})$  for  $N=2$  with that for  $N=3$ , we can find that the region for  $P(\delta\mu_{ia})$  in the  $SU(N=3)$  system is wider than that for  $N=2$ . Summarizing these results, we can say that the attractive interaction enhances the effects of disorder more strongly for larger  $N$ .

$P(\delta\mu_{i\sigma})$  gives us further information.  $P(\delta\mu_{ia})$  and  $P(\delta\mu_{ic})$  in the  $SU(3)$  systems are plotted in the right panel of Fig. 4.8. This figure indicates that  $P(\delta\mu_{ia})$  is slightly different from  $P(\delta\mu_{ic})$ , namely the effective lattice potential for particles with spin  $a$ , which are paired in the SF state, and that for particles with spin  $c$ , which are unpaired in the SF state and should be localized, are different. We note that the imbalance induced by the disorder would be characteristic of the superfluid state for the  $SU(N)$  systems with odd  $N$ , while such imbalance would not be observed for even  $N$  where all particles form Cooper-pairs in the SF state. The effective disorder corresponds to the local particle density. Thus, measuring the local particle density for each spin, we would be able to experimentally observe the imbalance predicted in our study.

#### 4.2.5 SF-AL transition in $SU(3)$ systems

To address the question what phenomena should be observed in strongly disordered regions, we calculate the site-average of the local superfluid order parameters for

such regions, and plot it in Fig. 4.9. As seen from Fig. 4.9,  $\Phi^{ba}$  suddenly becomes

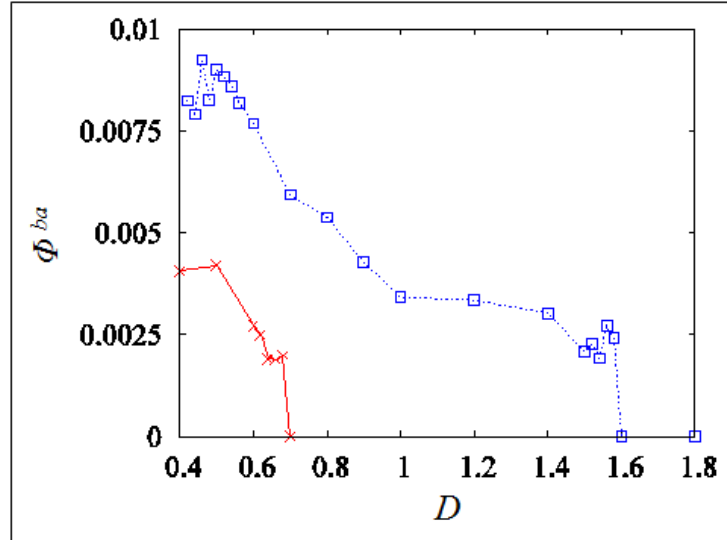


Fig. 4.9 Site-averaged superfluid order parameter  $\Phi^{ba}$  in the strongly disordered regions. We plot them for  $U=0.4$  (red solid line with crosses) and  $U=0.6$  (blue dotted line with squares).

equal to zero at critical disorder  $D_{AL}$ . It is confirmed that  $\Phi^{ba}$  is always zero at  $D > D_{AL}$  and the local superfluid order parameters at all sites are also zero. In addition to these properties, we confirm that the density of states for the particles with spin  $a$  or  $b$ , which are paired if the system is in a SF state, have no gap at the Fermi level as is the case with that for spin  $c$ , and the periodic oscillation of the density-density correlation function is not observed in the regions where  $\Phi^{ba}=0$ . From these features, it is concluded that the superfluid state undergoes a transition to the Anderson localized phase at critical disorder  $D_{AL}$ .

The SF-AL transition points increase with increase of an attractive interaction as is the case with the DW-SF transition points. The increase of  $D_{AL}$  is explained from the fact that the increase of an attractive interaction leads to the increase of the energy gained by the Cooper-pairs condensation. Fig. 4.9 gives us the further information that the site-average of the local superfluid order parameters jumps at  $D_{AL}$ . This result would indicate that the SF-AL transition is of first order. Here, it should be noted that the dependence of our results on disorder configurations can not be completely eliminated, and especially strongly influences the results near the transition points. Owing to this dependence, we can not sharply define the results near the SF-AL transition points. However, the jump in  $\Phi^{ba}$  is larger than the numerical errors caused by the sample dependence. Thus, we believe that the conclusion that the SF-AL transition is of first-order is reliable.

### 4.2.6 Ground state phase diagram of SU(3) Fermi systems

We systematically calculate the above quantities and determine the ground state phase diagram of SU(3) attractively interacting Fermi systems with spatial disorder at zero temperature and at half-filling. It is shown in Fig. 4.10. We can find from

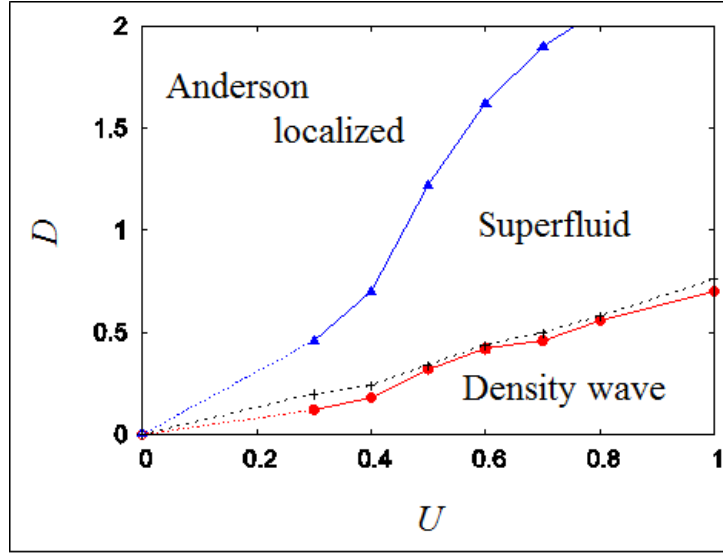


Fig. 4.10 Ground state phase diagram of SU(3) attractively interacting Fermi systems with spatial disorder at zero temperature and at half-filling. The red (blue) solid line with circles (triangles) denotes the DW-SF (SF-AL) transition point and the black dotted line with crosses shows the points where  $F_{\text{CDW}} = F_{\text{SF}}$ . The red and blue dashed line are deduced via the argument discussed in the text.

the phase diagram that  $D_{\text{SF}}$ , where the DW-SF transition is triggered, increases with increase of an attractive interaction. This result means that the attractive interaction makes the DW order more robust against spatial disorder because the attractive interaction leads to the increase of the difference between  $F_{\text{DW}}$  and  $F_{\text{SF}}$ . It is naturally expected from this result that  $D_{\text{SF}}$  goes to zero in  $U \rightarrow 0$  as shown in Fig. 4.10.

The DW-SF transition predicted in our study is of first order, and thus two kinds of transition points should appear in the ground state phase diagram. In Fig. 4.10, we plot only the transition points where this transition is triggered when we choose a SF state as an initial state, and do not show the other transition points when the initial state is a DW state. Owing to some technical reasons in the mean-field method, it is difficult to determine these transition points. For reference, we plot the points where  $F_{\text{CDW}} = F_{\text{SF}}$  in the phase diagram. We can naturally expect that there should be the transition points when the DW state is chosen as an initial state for

slightly larger  $D$  beyond the line where  $F_{\text{CDW}} = F_{\text{SF}}$ ,

Next, we would like to explain the SF-AL transition. This transition is characteristic of the SU(3) systems and qualitatively different from the SF-Cooper pair insulator transition which is observed in SU(2) systems and has been discussed in Chap. 3. The local superfluid order parameter at all sites becomes equal to zero in the Anderson localized phase while the superfluid order locally survives in the Cooper-pair insulating phase. Also, the SF-AL transition points increase as an attractive interaction increases whereas the attractive interaction leads to the decrease of the SF-Cooper pair insulator transition points. This difference arises from the fact that unpaired particles exist in the SF phase of the SU(3) system, and thus not only the strength of the coherence in the phases of the Cooper-pairs but also the energy gained by the SF order is relevant to the critical disorder where the SF-AL transition occurs, while the SF-Cooper pair insulator transition points are relevant to only the strength of the coherence in the phases of the Cooper-pairs. As shown in Fig. 4.10, it is deduced from this discussion that  $D_{\text{SF}}$  approaches zero if  $U \rightarrow 0$ .

### 4.3 SU(4) Fermi systems with spatial disorder

Similar calculations are performed for the SU(4) systems. First, we show the result of the density-density correlation function in Fig. 4.11. As is the case in the SU(3)

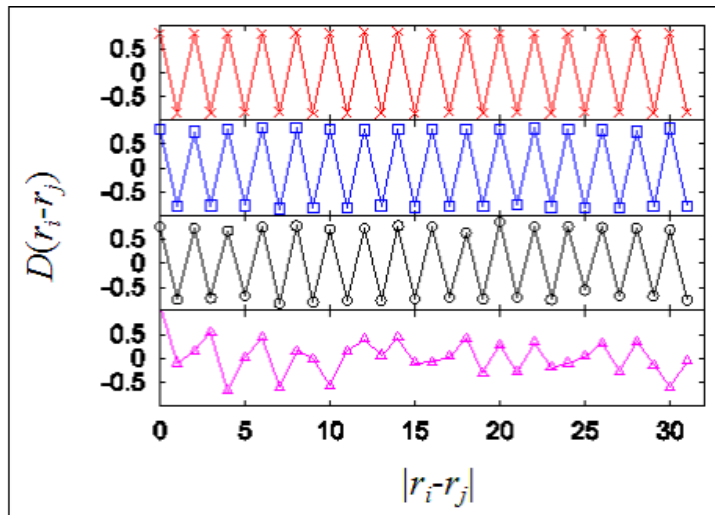


Fig. 4.11 Density-density correlation function in SU(4) systems for four different values of the disorder strength,  $D=0.2$  (red line with crosses),  $D=0.4$  (blue line with squares),  $D=0.8$  (black line with circles), and  $D=1.6$  (magenta line with triangles) from top to bottom.  $U=0.8$  is studied.

systems, it is found from this figure that although the periodic oscillation charac-

terizing the DW state is clearly observed in the weakly disordered regions, spatial disorder breaks down the DW order at a critical disorder strength. Comparing Fig. 4.11 with Fig. 4.2, we can see that the amplitude of  $D(r_i - r_j)$  for SU(4) systems is larger than that for SU(3) systems, and the DW order exists in the SU(4) systems even at  $D=0.8$  where the SF state realizes in SU(3) systems. This result implies that the DW order is more robust against spatial disorder with increase of the number of components, and is consistent with the fact that the energy gained by the CDW order increases in proportion to the number of possible pairs of the particles with different spins.

To confirm the DW-SF transition in the SU(4) systems, we systematically calculate the local superfluid order parameters. Surprisingly, however, we cannot find the regions where the local superfluid order parameters take a finite value, namely the SF state is stabilized as the ground state of the SU(4) systems. In the SU(4) systems, the DW phase directly undergoes a transition to the Anderson localized phase. We interpret this result as follows. As mentioned above, the DW order is rather robust against spatial disorder with increasing  $N$ . Thus, the energy gained by the Cooper-pair formation is not large enough to stabilize the superfluidity in between the DW state and the AL state.

There is the spectral gap at the Fermi level in the DW phase, while the gap is closed in the AL phase. This fact implies that the spectral gap is a good criterion for the DW-AL transition. Therefore, in order to determine the DW-AL transition points, the spectral gap width is systematically calculated, and shown in Fig. 4.12. We can obtain the result as expected that the DW-AL transition points increase as an attractive interaction increases because the attractive interaction makes the DW order robust against spatial disorder. Furthermore, it is seen from Fig. 4.12 that the DW-AL transition is of second order since the spectral gap width continuously decreases and becomes zero. Here, we should comment on the order of the DW-AL transition. The numerical method is used for this study, and thus it is not easy to perfectly conclude whether the transition is of first order or second order unless the clear jump, which is characteristic of the first order transition, is observed. In our calculations, it is concluded that the DW-AL transition is of second order, but there may be a probability that this transition is the first order transition which is characterized by a very small jump.

Some comments on the density-density correlation function and the density structure factor  $S_{\text{DW}}$  associated with it are in order. Each of them as with the spectral gap well characterizes the DW state, as discussed in Sec. 4.2.1. However, the response of these physical quantities to spatial disorder is different. As shown in Fig. 4.12, the decrease of the spectral gap width associated with the increase of the dis-

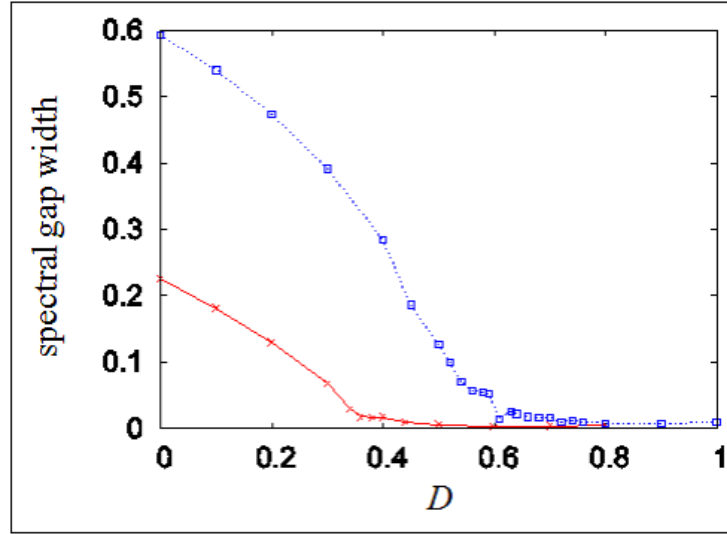


Fig. 4.12 Spectral gap width in SU(4) systems as a function of the disorder strength. Then for  $U=0.4$  (red solid line with crosses) and  $U=0.6$  (blue dotted line with squares) are plotted.

order strength is monotonic and well reflects the response of the systems to spatial disorder. By contrast, the amplitude of the density-density correlation function is smaller with increasing the strength of disorder but seems to be hardly affected by the effects of disorder away from the transition points. Also, the density structure factor (see Fig. 4.3) is almost unchanged in the DW state. We note that the amplitude of the density-density correlation function and the density structure factor correspond to the spectral gap, and hence the response of these physical quantities to spatial inhomogeneity is considered to be similar. However, this correspondence seems not to be established in our study. This would be because the density-density correlation function and the density structure factor are strongly affected by configurations of disorder in space, and hence the effects of disorder are misestimated when the disorder average of the density-density correlation function and the density structure factor is taken. Thereby, the DW-AL transition points cannot be definitely determined only from the results of these two physical quantities. These arguments suggest that the spectral gap width is more suitable for determining critical disorder at which the DW-AL transition is induced, as has been done in our studies.

The ground state phase diagram of the SU(4) systems with spatial disorder is determined from the systematic calculations of the spectral gap width, and shown in Fig. 4.13. The disorder breaks down the spectral gap formed by the DW order, and then triggers the DW-AL transition. The spectral gap becomes large with increasing the attractive interaction. Thereby, the increase of the attractive interaction leads

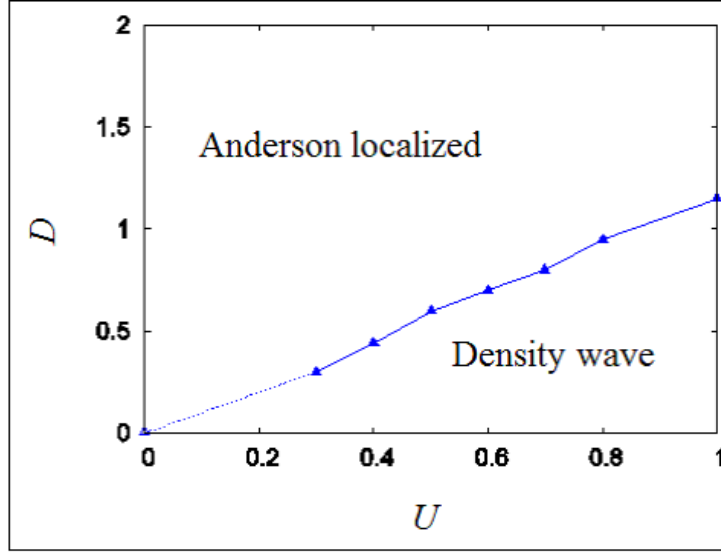


Fig. 4.13 Ground state phase diagram of SU(4) systems at zero temperature and at half-filling. The DW-AL transition points are denoted by the blue solid line with triangles. We deduce the blue dashed line via the argument discussed in the text.

to the increase of the DW-AL transition points. From this argument, we deduce the DW-AL transition points in the  $U < 0.3$  regions as shown in Fig. 4.13. As mentioned above, density-wave phase-Anderson localized phase transition points increase as an attractive interaction increases. Comparing this phase diagram of the SU(4) systems with that of the SU(3) systems, we can find that the regions, where the DW phase is stabilized as the ground state in SU(4) systems, are wider than those in SU(3) systems, and also the Anderson localized phase realizes in the rather wide regions. It is naturally expected from these results that the DW phase undergoes a direct transition to the Anderson localized phase when  $N > 3$ , and the critical disorder where the DW-AL transition occurs in SU( $N > 3$ ) systems increases with increase of  $N$ .

## 4.4 Summary

The results described in this chapter are summarized here. Using the BdG methods, we studied the SU( $N$ ) Fermi systems with on-site attractive interaction and spatial disorder, which are well-described by the SU( $N$ ) attractive Anderson-Hubbard model.

We found that in SU(3) systems the spatial disorder induces the DW-SF transition, and stabilizes the SF state as the ground state; the spatial disorder not only lifts the degeneracy between the DW phase and the SF phase as found in the previous study on the SU(2) case[48], but also can change the ground state according to the strength

of disorder. It was elucidated that the spectral gap on the Fermi energy closes and the histogram of the local particle density changes from the bimodal distribution to the single-peak distribution at the DW-SF transition point. It was clarified from the results of the effective disorder obtained that the attractive interaction more strongly enhances the effects of disorder as  $N$  becomes larger. It was also found that the SF-AL transition occurs as the strength of spatial disorder further increases. Furthermore, we showed that these two transitions are of first order. The ground state phase diagram of the SU(3) systems was determined, and it was clarified that the increase of the attractive interaction leads to the increase of the critical disorder strength where each transition is triggered.

We also addressed the SU(4) attractive Anderson-Hubbard model with spatial nonuniformity, and thus found that the DW state directly undergoes a transition to the AL state, and the DW-AL transition is of second-order. We concluded that this is because the DW order is rather robust against spatial disorder with increasing  $N$ , and therefore the energy gained by the SF order is not large enough to stabilize the superfluidity in the region where the DW order is broken down by spatial disorder. We expect from this result that the DW-AL direct-transition occurs in SU( $N > 3$ ) systems. The transitions discovered in our study are unique for the SU(3) or SU(4) systems, and cannot be observed in SU(2) systems.

## Chapter 5

# Conclusion

This thesis reported theoretical studies on the spatially disordered optical lattices. Here, we summarize this thesis.

In Chap. 1, we introduced the results given by recent experiments of cold atoms, and explained the important theoretical studies of spatially disordered systems. Also, the experiments of multicomponent Fermi systems were introduced and the notable previous studies of them were explained. These results suggest that multicomponent Fermi systems with spatial disorder should be realized in cold atomic systems. Motivated by these backgrounds, we investigated the  $N \geq 2$ -component attractively interacting Fermi systems with spatial disorder. The aim of our study was briefly described at the end of this chapter.

Chap. 2 gave a self-contained introduction of a statistical dynamical mean-field theory and a Bogoliubov-de Gennes method used in this study. We reviewed the microscopic derivation of a dynamical mean-field theory and explained the basic concept of it and a coherent potential approximation. How to treat the backscattering effects caused by strong disorder within the dynamical mean-field theory was described, and the statistical dynamical mean-field theory, which enables us to successfully treat the effects of spatial inhomogeneity and correlation between particles on equal footing, was introduced. We explained the self-consistent loop and the advantage of the statistical dynamical mean-field theory in detail, and also discussed the difference between it and other numerical methods. We chose the modified iterative perturbation theory as an impurity solver, and the explanation of this solver was described. In this study, the Bogoliubov-de Gennes method was extended to investigate multicomponent Fermi systems, and how to extend it was explained in detail. Moreover, we discussed the anomalous superfluid state which is characteristic of the multicomponent attractively-interacting Fermi systems.

We presented the obtained results of two-component Fermi systems in Chap. 3. Uniform disorder and binary disorder were considered as the distribution function which characterizes the spatial disorder. We confirmed that the superfluid long-

range order is suppressed by spatial disorder in uniformly disordered systems, and hence the superfluid state-Cooper-pair insulating state transition occurs at a certain disorder strength. Furthermore, it was found that as the disorder strength further increases, the Cooper-pair insulator gradually crossovers to the ordinary Anderson insulator. The properties of these transitions were discussed from the geometrical average of the local density of states and the local superfluid order parameters. The results given in this study demonstrated that the attractive interaction enhances the effects of spatial inhomogeneity. We performed similar calculations for the systems with binary disorder. Thus, we clarified the universal effects which are caused by spatial inhomogeneity and do not depend on the nature of the probability distribution functions, and the specific properties which depend on the probability distribution function.

In Chap. 4, we showed the results of the SU(3) and SU(4) attractively interacting Fermi systems with spatial disorder. It is known that the density-wave state is stabilized as the ground state in SU( $N>2$ ) Fermi systems if the systems are not spatially disordered. To investigate how spatial inhomogeneity influences the density-density correlation, we calculated the density-density correlation function and the structure factor associated with it. Therefore, we found that spatial disorder breaks down the density-wave order. Moreover, we clarified from the results of the local superfluid order parameters that disorder induces the transition between the density-wave state and the superfluid state. The characteristic properties of this transition were discussed in details from the site-averaged density of states and the histogram of a local particle density. It was also demonstrated that the superfluid long-range order is broken down by spatial nonuniformity in strongly disordered regions, and thus the superfluid phase-Anderson localized phase transition is triggered. The above two transitions are of first-order. Similar calculations were performed for the SU(4) systems. In these systems, we could also confirm as with the SU(3) systems that the periodic oscillation of the density-density correlation function characterized by the density-wave order disappears at a certain disorder strength. Surprisingly, however, we could not find the regions where the superfluid state is stabilized as the ground state of the SU(4) systems. In the SU(4) systems, the density-wave phase directly undergoes a transition to the Anderson localized phase. We concluded from this result that the direct transition between the density-wave state and the Anderson localized state should be observed in SU( $N>3$ ) systems.

# Bibliography

- [1] A. Ashkin, Phys. Rev. Lett. **24**, 156 (1970).
- [2] A. Ashkin, J. M. Dziedzic, J. E. Bjorkholm, and S. Chu, Opt. Lett. **11**, 288 (1986).
- [3] S. Chu, J. E. Bjorkholm, A. Ashkin, and A. Cable, Phys. Rev. Lett. **57**, 314 (1986).
- [4] S. Chu, L. Hollberg, J. E. Bjorkholm, A. Cable, and A. Ashkin, Phys. Rev. Lett. **55**, 48 (1985).
- [5] A. L. Migdall, J. V. Prodan, W. D. Phillips, T. H. Bergeman, and H. J. Metcalf, Phys. Rev. Lett. **54**, 2596 (1985).
- [6] N. Masuhara, J. M. Doyle, J. C. Sandberg, D. Kleppner, T. J. Greytak, H. F. Hess, and G. P. Kochanski, Phys. Rev. Lett. **61**, 935 (1988).
- [7] W. Petrich, M. H. Anderson, J. R. Ensher, and E. A. Cornell, Phys. Rev. Lett. **74**, 3352 (1995).
- [8] M. H. Anderson, J. R. Ensher, M. R. Matthews, C. E. Wieman, E. A. Cornell, Science **269**, 198 (1995).
- [9] K. B. Davis, M.-O. Mewes, M. R. Andrews, N. J. van Druten, D. S. Durfee, D. M. Kurn, and W. Ketterle, Phys. Rev. Lett. **75**, 3969 (1995).
- [10] P. S. Jessen and I. H. Deutsch, Adv. At., Mol., Opt. Phys. **37**, 95 (1996).
- [11] J. Billy, V. Josse, Z. Zuo, A. Bernard, B. Hambrecht, P. Lugan, D. Clément, L. Sanchez-Palencia, P. Bouyer, and A. Aspect, Nature **453**, 891(2008).
- [12] S. S. Kondov, W. R. McGehee, J. J. Zirbel, and B. DeMarco, Science **334**, 66 (2011).
- [13] M. Greiner, O. Mandel, T. Esslinger, T. W. Hänsch, and I. Bloch, Nature(London) **415**, 39 (2002).
- [14] C. Becker, P. Soltan-Panahi, J. Kronjäger, S. Dörscher, K. Bongs, and K. Sengstock, New J. Phys. **12**, 065025 (2010).
- [15] J. Struck, C. Ölschläger, R. Le Targat, P. Soltan-Panahi, A. Eckardt, M. Lewenstein, P. Windpassinger, K. Sengstock, Science **333**, 996 (2011).
- [16] M. Ölschläger, G. Wirth, and A. Hemmerich, Phys. Rev. Lett. **106**, 015302 (2011).
- [17] G. Wirth, M. Ölschläger, and A. Hemmerich, Nat. Phys. **7**, 147 (2011).

- 
- [18] P. Soltan-Panahi, J. Struck, P. Hauke, A. Bick, W. Plenkers, G. Meineke, C. Becker, P. Windpassinger, M. Lewenstein, and K. Sengstock, *Nat. Phys.* **7**, 434 (2011).
- [19] L. Tarruell, D. Greif, T. Uehlinger, G. Jotzu, and T. Esslinger, *Nature (London)* **483**, 302 (2012).
- [20] G.-B. Jo, J. Guzman, C. K. Thomas, P. Hosur, A. Vishwanath, and D. M. Stamper-Kurn, *Phys. Rev. Lett.* **108**, 045305 (2012).
- [21] S. Taie, H. Ozawa, T. Ichinose, T. Nishio, S. Nakajima, and Y. Takahashi, *Sci. Adv.* **1**, e15008545 (2015).
- [22] J. E. Lye, L. Fallani, M. Modugno, D. S. Wiersma, C. Fort, and M. Inguscio, *Phys. Rev. Lett.* **95**, 070401(2005).
- [23] D. Clément, A. F. Varón, M. Hugbart, J. A. Retter, P. Bouyer, L. Sanchez-Palencia, D. M. Gangardt, G. V. Shlyapnikov, and A. Aspect, *Phys. Rev. Lett.* **95**, 170409 (2005).
- [24] F. Sanchez-Palencia and M. Lewenstein, *Nat. Phys.* **6**, 87 (2010).
- [25] F. Jendrzejewski, A. Bernard, K. Müller, P. Cheinet, V. Josse, M. Piraud, L. Pezzé, L. Sanchez-Palencia, A. Aspect, and P. Bouyer, *Nat. Phys.* **8**, 398 (2012).
- [26] H. Feshbach, *Ann. Phys. (N.Y.)* **5**, 357 (1958).
- [27] K. Gunter, T. Stoferle, H. Moritz, M. Kohl, and T. Esslinger, *Phys. Rev. Lett.* **96**, 180402 (2006).
- [28] C. Ospelkaus, S. Ospelkaus, L. Humbert, P. Ernst, K. Sengstock, and K. Bongs, *Phys. Rev. Lett.* **97**, 120402 (2006).
- [29] T. Best, S. Will, U. Schneider, L. Hackermuller, D.-S. Luhmann, D. van Oosten, and I. Bloch, *Phys. Rev. Lett.* **102**, 030408 (2009).
- [30] H. Hara, Y. Takasu, Y. Yamaoka, J. M. Doyle, and Y. Takahashi, *Phys. Rev. Lett.* **106**, 205304 (2011).
- [31] S. Sugawa, K. Inaba, S. Taie, R. Yamazaki, M. Yamashita, and Y. Takahashi, *Nat. Phys.* **7**, 642 (2011).
- [32] I. Ferrier-Barbut, M. Delehaye, S. Laurent, A.T. Grier, M. Pierce, B.S. Rem, F. Chevy, and C. Salomon, *Science* **345**, 1035 (2014).
- [33] Y. Eto, M. Kunimi, H. Tokita, H. Saito, and T. Hirano, *Phys. Rev. A* **92**, 013611 (2015).
- [34] B. DeMarco and D. S. Jin, *Science* **285**, 1703 (1999).
- [35] A. G. Truscott, K. E. Strecker, W. I. McAlexander, G. B. Partridge, and R. G. Hulet, *Science* **291**, 2570 (2001).
- [36] T. Fukuhara, Y. Takasu, M. Kumakura, and Y. Takahashi, *Phys. Rev. Lett.* **98**, 030401 (2007).
- [37] B. J. DeSalvo, M. Yan, P. G. Mickelson, Y. N. Martinez de Escobar, and T. C.

- Killian, Phys. Rev. Lett. **105**, 030402 (2010).
- [38] M. Kitagawa, K. Enomoto, K. Kasa, Y. Takahashi, R. Ciuryło, P. Naidon, and P. S. Julienne, Phys. Rev. A **77**, 012719 (2008).
- [39] S. Taie, R. Yamazaki, S. Sugawa, and Y. Takahashi, Nat. Phys. **8**, 825 (2012).
- [40] P. W. Anderson, Phys. Rev. **109**, 1498 (1958).
- [41] E. Abrahams, P. W. Anderson, D. C. Licciardello, and T. V. Ramakrishnan, Phys. Rev. Lett. **42**, 673 (1979).
- [42] T. F. Rosenbaum, K. Andres, G. A. Thomas, and R. N. Bhatt, Phys. Rev. Lett. **45**, 1723 (1980).
- [43] N. F. Mott, Philos. Mag. **26**, 1015 (1972).
- [44] S. Hikami, A. I. Larkin, and Y. Nagaoka, Prog. Theor. Phys. **63**, 707 (1980).
- [45] Y. Kawaguchi and S. Kawaji, J. Phys. Soc. Jpn. **48**, 699 (1980).
- [46] K. Byczuk, W. Hofstetter, and D. Vollhardt, Phys. Rev. Lett. **94**, 056404 (2005).
- [47] K. Byczuk, W. Hofstetter, and D. Vollhardt, Phys. Rev. Lett. **102**, 146403 (2009).
- [48] C. Huscroft and R. T. Scalettar, Phys. Rev. B **55**, 1185 (1997).
- [49] P. W. Anderson, J. Phys. Chem. Solids **11**, 26 (1959).
- [50] T. I. Baturina, D. R. Islamov, J. Bentner, C. Strunk, M. R. Baklanov, and A. Satta, JETP Lett. **79**, 337 (2004).
- [51] B. Sacépé, C. Chapelier, T. I. Baturina, V. M. Vinokur, M. R. Baklanov, and M. Sanquer, Phys. Rev. Lett. **101**, 157006 (2008).
- [52] B. Sacépé, C. Chapelier, T. Baturina, V. Vinokur, M. Baklanov, and M. Sanquer, Nat. Commun. **1**, 140 (2010).
- [53] B. Sacépé, T. Dubouchet, C. Chapelier, M. Sanquer, M. Ovadis, D. Shahar, M. Feige'lman, and L. Ioffe, Nat. Phys. **7**, 239 (2011).
- [54] M. Mondal, A. Kamlapure, M. Chand, G. Saraswat, S. Kumar, J. Jesudasan, L. Benfatto, V. Tripathi, and P. Raychaudhuri, Phys. Rev. Lett. **106**, 047001 (2011).
- [55] M. Chand, G. Saraswat, A. Kamlapure, M. Mondal, S. Kumar, J. Jesudasan, V. Bagwe, L. Benfatto, V. Tripathi, and P. Raychaudhuri, Phys. Rev. B **85**, 014508 (2012).
- [56] Y. Noat, V. Cherkez, C. Brun, T. Cren, C. Carbillet, F. Debontridder, K. Ilin, M. Siegel, A. Semenov, H.-W. Hübers, and D. Roditchev, Phys. Rev. B **88**, 014503 (2013).
- [57] P. G. de-Gennes, Rev. Mod. Phys. **36**, 225 (1964).
- [58] A. Ghosal, M. Randeria, and N. Trivedi, Phys. Rev. B **65**, 014501 (2001).
- [59] Y. Dubi, Y. Meir, and Y. Avishai, Nature (London) **449**, 876 (2007).
- [60] P. Dey and S. Basu, J. Phys., Condens. Matter **20**, 485205 (2008).

- 
- [61] X. T. Wu and R. Ikeda, Phys. Rev. B **83**, 104517 (2011).
- [62] G. Seibold, L. Benfatto, C. Castellani, and J. Lorenzana, Phys. Rev. Lett. **108**, 207004 (2012).
- [63] S. Ghosh and S. S. Mandal, Phys. Rev. Lett. **111**, 207004 (2013).
- [64] A. Gerges, G. Kotliar, W. Krauth, and M. J. Rozenberg, Rev. Mod. Phys. **68**, 13 (1996).
- [65] A. Garg, H. R. Krishnamurthy, and M. Randeria, Phys. Rev. B **72**, 024517 (2005).
- [66] J. Bauer, A. C. Hewson, and N. Dupuis, Phys. Rev. B **79**, 214518 (2009).
- [67] I. Affleck and J. B. Marston, Phys. Rev. B **37**, 3774 (1988).
- [68] J. B. Marston and I. Affleck, Phys. Rev. B **39**, 11538 (1989).
- [69] C. Honerkamp and W. Hofstetter, Phys. Rev. Lett. **92**, 170403 (2004).
- [70] C. Honerkamp and W. Hofstetter, Phys. Rev. B **70**, 094521 (2004).
- [71] N. Kawashima and Y. Tanabe, Phys. Rev. Lett. **98**, 057202 (2007).
- [72] R. W. Cherng, G. Refael, and E. Demler, Phys. Rev. Lett. **99**, 130406 (2007).
- [73] Á. Rapp, G. Zaránd, C. Honerkamp, and W. Hofstetter, Phys. Rev. Lett. **98**, 160405 (2007).
- [74] Á. Rapp, W. Hofstetter, and G. Zaránd, Phys. Rev. B **77**, 144520 (2008).
- [75] M. A. Cazalilla, A. F. Ho, and M. Ueda, New J. Phys. **11**, 103033 (2009).
- [76] A. Kantian, M. Dalmonte, S. Diehl, W. Hofstetter, P. Zoller, and A. J. Daley, Phys. Rev. Lett. **103**, 240401 (2009).
- [77] A. V. Gorshkov, M. Hermele, V. Gurarie, C. Xu, P. S. Julienne, J. Ye, P. Zoller, E. Demler, M. D. Lukin, and A. M. Rey, Nat. Phys. **6**, 289 (2010).
- [78] G. Klingschat and C. Honerkamp, Phys. Rev. B **82**, 094521 (2010).
- [79] P. Corboz, A. M. Läuchli, K. Penc, M. Troyer, and F. Mila, Phys. Rev. Lett. **107**, 215301 (2011).
- [80] K. Inaba and S. Suga, Phys. Rev. Lett. **108**, 255301 (2012).
- [81] Y. Okanami, N. Takemori, and A. Koga, Phys. Rev. A **89**, 053622 (2014).
- [82] V. Dobrosaavjević and G. Kotliar, Phys. Rev. Lett. **78**, 3943 (1997).
- [83] V. Dobrosaavjević and G. Kotliar, Philos. Trans. R. Soc. London Ser. A **356**, 57 (1998).
- [84] K. Byczuk, W. Hofstetter, U. Yu, and D. Vollhardt, Eur. Phys. J. Special Topics **180**, 135 (2010).
- [85] P. Soven, Phys. Rev. **156**, 809 (1967).
- [86] F. Yonezawa and K. Morigaki, Prog. Theor. Phys. Suppl. No. **53**, 1 (1973).
- [87] H. Kajueter and G. Kotliar, Phys. Rev. Lett. **77**, 131 (1996).
- [88] M. Potthoff, T. Wegner, and W. Nolting, Phys. Rev. B **55**, 16132 (1997).
- [89] R. Vlaming and D. Vollhardt, Phys. Rev. B **45**, 4637 (1992).

- [90] K. Koepernik, B. Velický, R. Hayn, and H. Eschrig, *Phys. Rev. B* **55**, 5717 (1997).
- [91] J. Tobała, L. Jodin, P. Pecher, H. Scherrer, G. Venturini, B. Malaman, and S. Kaprzyk, *Phys. Rev. B* **64**, 155103 (2001).
- [92] V. Janiš and D. Vollhardt, *Phys. Rev. B* **46**, 15712 (1992).
- [93] V. Dobrosavljević and G. Kotliar, *Phys. Rev. B* **50**, 1430 (1994).
- [94] M. Ulmke, V. Janiš and D. Vollhardt, *Phys. Rev. B* **51**, 10411(1995).
- [95] M. S. Laad, L. Craco, and E. M. Hartmann, *Phys. Rev. B* **64**, 195114 (2001).
- [96] K. Byczuk, M. Ulmke, and D. Vollhardt, *Phys. Rev. Lett.* **90**, 196403 (2003).
- [97] K. Byczuk, W. Hofstetter, and D. Vollhardt, *Phys. Rev. B* **69**, 045112 (2004).
- [98] M. C. O. Aguiar, V. Dobrosavljević, E. Abrahams, and G. Kotliar, *Phys. Rev. B* **71**, 205115 (2005).
- [99] M. M. Radonjić, D. Tanasković, V. Dobrosavljević, and K. Haule, *Phys. Rev. B* **81**, 075118 (2010).
- [100] A. I. Poteryaev, S. L. Skornyakov, A. S. Belozarov, and V. I. Anisimov, *Phys. Rev. B* **91**, 195141 (2015).
- [101] D. Semmler, K. Byczuk, and W. Hofstetter, *Phys. Rev. B* **81**, 115111 (2010).
- [102] D. Semmler, J. Wernsdorfer, U. Bissbort, K. Byczuk, and W. Hofstetter, *Phys. Rev. B* **82**, 235115 (2010).
- [103] D. Semmler, K. Byczuk, and W. Hofstetter, *Phys. Rev. B* **84**, 115113 (2011).
- [104] V. Dobrosavljević, A. A. Pastor, and B. K. Nikolić, *Europhys. Lett.* **62**, 76 (2003).
- [105] M. C. O. Aguiar, V. Dobrosavljević, E. Abrahams, and G. Kotliar, *Phys. Rev. B* **73**, 115117 (2006).
- [106] M. C. O. Aguiar, V. Dobrosavljević, E. Abrahams, and G. Kotliar, *Phys. Rev. Lett.* **102**, 156402 (2009).
- [107] R. D. B. Carvalho, G. M. A. Almeida, and A. M. C. Souza, *Eur. Phys. J. B* **87**, 160 (2014).
- [108] J. Skolimowski, D. Vollhardt, and K. Byczuk, *Phys. Rev. B* **92**, 094202 (2015).
- [109] H. Braganca, M. C. O. Aguiar, J. Vučičević, D. Tanasković, and V. Dobrosavljević, *Phys. Rev. B* **92**, 125143 (2015).
- [110] E. M. Hartmann, *Z. Phys. B* **76**, 211 (1989).
- [111] M. Caffarel and W. Krauth, *Phys. Rev. Lett.* **72**, 1545 (1994).
- [112] M. Jarrell, *Phys. Rev. Lett.* **69**, 168 (1992).
- [113] K. G. Wilson, *Rev. Mod. Phys.* **47**, 773 (1975).
- [114] A. N. Rubtsov, V. V. Savkin, and A. I. Lichtenstein, *Phys. Rev. B* **72**, 035122 (2005).
- [115] A. Georges and G. Kotliar, *Phys. Rev. B* **45**, 6479 (1992).
- [116] M. J. Rozenberg, G. Kotliar, and X. Y. Zhang, *Phys. Rev. B* **49**, 10181 (1994).

- [117] D. J. Scalapino, S. R. White, and S. Zhang, *Phys. Rev. B* **47**, 7995 (1993).  
[118] S. Kirkpatrick, B. Velický, and H. Ehrenreich, *Phys. Rev. B* **1**, 3250 (1970).

# Acknowledgment

First of all, I would like to express my sincerest gratitude to Professor Norio Kawakami for his appropriate guidance and kindhearted encouragement during my five years graduate course. He always took time off for discussing insights of research projects with me. From the conversations with him, I have learned a lot not only about physics, but also many tips of the daily activities.

I wish to thank Kazuto Noda a lot. Through the collaboration with him, I have deeply learned the numerical methods from him. Also, thanks to his gracious leadings, the work has been successfully completed. His insights of our crude results have given a friendly picture, which always took me to next step.

I would like to thank the faculty in the condensed matter theory group at Kyoto, Ryusuke Ikeda, Satoshi Fujimoto, Hiroaki Ikeda, Masaki Tezuka, Kazushi Aoyama, and Robert Peters for their help in various academic matters. Also I benefited from discussions and interactions with many inspiring colleagues and friends in the condensed matter theory group. I especially express my acknowledgments to Yuto Takanaka, Yuichiro Dan, and Kyosuke Adachi, who have been responsible for the computer system in the group.

I would like to acknowledge financial support I received over the past two years from the Japan Society for the Promotion of Science (JSPS), without which the work reported in this dissertation would not have been possible.

At last, I express my sincere gratitude to my parents, Tsutomu Sakaida and Yoshiko Sakaida. I really benefited from their long-time support and understandings for my decision to study physics.